UNIVERSITE DE NICE-SOPHIA ANTIPOLIS - UFR Sciences
Ecole Doctorale en Sciences Fondamentales et Appliquées

T H E S E

pour obtenir le titre de
Docteur en Sciences
de l'Université de Nice-Sophia Antipolis

Discipline: Physique

Présentée et soutenue par

Biran WANG

Rheology and Magnetolysis of Tumor Cells

Thèse dirigée par : **Georges BOSSIS**

Soutenue le : *4-Décembre-2012*

Jury :

Dr. Alain Ponton	Directeur de recherche	(Rapporteur)
Dr. Olivier Sandre	Chargé de Recherche	(Rapporteur)
Dr. Georges Bossis	Directeur de recherche	
Dr. Christophe Di-Giorgio	Maître de conférences	
Dr. Pierre Vierling	Directeur de recherche	
Dr. Andrey Zubarev	Professeur	

ACKNOWLEDGMENTS

I would like to express my gratitude to my supervisor, Georges BOSSIS, for supporting me over the years, and for giving me so much freedom to explore and discover new areas of biophysics. I appreciate his vast knowledge and skill in many areas and his assistance in writing reports. My co-supervisor, Pierre VIERLING, has also been very supportive to me. To each of them I owe a great debt of gratitude for their patience, inspiration and friendship.

A sincere acknowledgment goes to the external reading committee, Alain Ponton, Olivier Sandre and Andrey Zubarev, thanks to their availability and effort in reading my work.

The research that has gone into this thesis was very enjoyable. The "sixth floor" has provided an excellent environment for my research. I spent many enjoyable hours with the team; I cannot find words to express my gratitude to them, Alain, Aladine, Alexandrza, Audrey, Cecilia, Jacques, Olga, Pascal, Pavel, Romain and all the visitors, what a hot ambience!! We've chatted about politics, broken news and of cause also the latest ideas about experiences over a cup of coffee. Without this rich environment, I doubt that many of my experiences would have come to fruition.

I am indebted to my many colleagues in "downtown" LPMC, who supported me, first of all, the two directors of laboratory, Gérard and Fabrice, who received me very kindly.

I wish to thank the members of Administrative department of LPMC, Denise, Christine C, Christine B and Nathalie, which helped me a lot about administrative stuffs, since I'm a Chinese, I have ten times more administrative papers than the other colleagues; without them, I couldn't finish my thesis in time, or ever could not start.

And of course, thanks go also to the member of technical services, mechanical workshop, chemical workshop, electrical workshop and computer department, without their help, lots of experiences would not be realized. A special memory goes to our respectable colleague, Dédé, who helped me a lot for the mechanical realization; he was really "a diamond of the first water".

I would also like to thank the other members of LPMC, who helped me to make the transition from process engineer to biophysicist, and I appreciate that.

I would like to thank my many friends and colleagues at LCMBA, with whom I have had the pleasure of working over the years. These include Céline, Nicolas, Christophe and all the members of the LCMBA.

Thanks also to my family in China, who have been extremely understanding and supportive of my studies. I feel very lucky to have a family that shares my enthusiasm for academic pursuits.

Finally, I would especially like to thank my beautiful wife Juan, who has encouraged me so much over the years, and my adorable son Zhidao, who has given me biggest smell of the world every day, and my little Amy, who came out in time for her dad's viva voce, it was them who given me the motivation to finish this thesis.

RÉSUMÉ COURT (FR. EN)

Les nanoparticules magnétiques peuvent être utilisées pour détruire des cellules cancéreuses. La connaissance des propriétés rhéologiques de ces cellules permet de modéliser le mouvement des particules sur la surface des membranes et de mieux comprendre les mécanismes en jeu. Une première approche fut d'utiliser des microsondes magnétiques pour déterminer les propriétés viscoélastiques du milieu cellulaire. Puis une technique plus directe à l'aide d'un AFM a été utilisée. Nous avons à cet effet développé une méthode générale d'analyse du mouvement de la pointe AFM pour les étapes d'indentation et de relaxation, ce qui permet une détermination plus précise des paramètres rhéologiques de cellules et en particulier de la lignée Hep-G2. La modélisation du comportement viscoélastique des cellules a ensuite permis de calculer l'indentation de ces cellules par des particules magnétiques soumise à un gradient de champ magnétique. Des nanoparticules de fer en forme de fuseau, recouvertes d'or, ainsi que des nanofibres de cobalt ont été synthétisées au laboratoire. Nous avons montré que l'application d'un champ magnétique de basse fréquence (quelques Hz) sur ces nanoparticules de fer pouvait "in vitro" détruire des cellules cancéreuses mais que, par contre, un champ constant n'avait pratiquement aucun effet. En s'appuyant sur la modélisation de l'indentation, on montre que seule la formation de clusters de particules peut expliquer ces résultats. A coté de la magnétolyse par voie mécanique, nous avons montré qu'il était aussi possible d'utiliser l'importante hystérésis magnétique des nanoparticules de cobalt pour le traitement par hyperthermie de cellules cancéreuses à des fréquences aussi basses que 10 kHz.

Magnetic nanoparticles can be used to destroy cancer cells. The knowledge of the rheological properties of the cancer cells allows to model the motion of the particles at the surface of the membrane and to get a better understanding of the mechanisms. A first approach was to use magnetic microprobes to determine the viscoelastic properties of a gel that represent the tumor cells. Then a more convenient AFM method has been employed. We have carried out a more general analysis of the AFM tip motion which contains both the indentation and relaxation steps, allowing a better determination of the rheological parameters, in particular of cancer cell called Hep-G2. The knowledge of the viscoelastic behavior of these cells allowed us to predict their indentation by magnetic particles submitted to an alternative field gradient. The synthesis of some of these particles such as: spindle-type iron and gold core-shell nanoparticles, and cobalt nanoneedles were carried out in our laboratory. We proved that the application of an alternative magnetic field of low frequency (a few Hertz) in the presence of magnetic microparticles was able "in vitro" to destroy cancer cells, and a constant magnetic field was far less efficient than an oscillating one. Based on the indentation model, we proposed that the magnetic field induces the formation of clusters of particles which are then large enough to damage the membranes of the cells. Besides magnetolysis by mechanical way we have also shown that cobalt nanoneedles presented an important hysteresis cycle which can be used for hyperthermia treatment of cancer cells at frequencies as low as 10 kHz.

ABSTRACT

Magnetic nanoparticles can be used to destroy cancer cells by applying an external magnetic field at high frequency, which produces a local heating due to the lag between the magnetization and the field. More recently, some works have concluded that it was also possible to destroy the membranes of the cell thanks to a mechanical damage caused by the oscillating motion of the magnetic nanoparticles. The knowledge of the rheological properties of the cancer cells allows to model the motion of the particles at the surface of the membrane and to get a better understanding of the mechanism, which come in play. A first approach was investigated based on the use of magnetic microprobes whose motion can be followed with a videocamera; although giving a good representation of the viscoelastic properties of a gel, it is difficult to apply on biological cells. A more convenient method lies on the use of atomic force microscopy (AFM) by looking at the relaxation of the force when a constant position of the AFM head is maintained or at the evolution of the indentation when a constant force is maintained. In both cases the analysis rests on the hypothesis that the motion of the probe inside the tissue before the relaxation step is realized in a time, which is much smaller than the characteristic relaxation time of the material. In this study we carry out a more general analysis of the probe motion, which contains both the indentation and relaxation steps, allowing a better determination of the rheological parameters. This analysis contains a correction of the Hertz model for large indentation and also a correction due to the finite thickness of the biological material; it can be applied to determine the parameters representing any kind of linear viscoelastic model. This approach is then used to model the rheological behavior of one kind of cancer cell called Hep-G2. For this kind of cell, a power law model does not well describe the low and high frequency modulus contrary to a generalized Maxwell model.

The knowledge of the viscoelastic behavior of the cells allowed us to predict the indentation of cells by magnetic microparticles submitted to an alternative field gradient. The synthesis of some of these particles such as: spindle-type iron and gold core-shell nanoparticles, and cobalt nanoneedles, were carried out in the LPMC. We proved that the application of an alternative magnetic field of low frequency (a few Hertz) in the presence of magnetic nanoparticles was able "in vitro" to destroy cancer cells. Also it was shown that a constant magnetic field was

far less efficient than an oscillating one. The mechanical model of indentation of the cell by the particles has demonstrated that the indentation by a single particle, in our experimental conditions, was in the range of the nanometer. Using an AFM tip as indenter, the lysis of the membrane needed amplitudes of indentation at least one order of magnitude larger. The explanation, which is proposed, based on observations under microscope before and after the application of the field, is that the magnetic field induces the formation of clusters of particles, which are then large enough to damage the membranes of the cells.

Besides magnetolysis by mechanical way we have also shown that cobalt nanoneedles presented an important hysteresis cycle, which can be used for hyperthermia treatment of cancer cells at frequencies as low as 10 kHz, compared to a few hundred kHz in usual conditions.

TABLE OF CONTENTS

LIST OF ILLUSTRATIONS

LIST OF TABLE

1. INTRODUCTION (FR. EN)

知己知彼 百战不殆

«Qui connaît son ennemi comme il se connaît, en cent combats ne sera point défait»

- 孙子兵法- Sun Tzu, L'Art de la guerre

Le cancer est l'ennemi public N° 1 de la société, de nombreuses stratégies ont été développées pour lutter contre lui, l'une d'entre elles est basée sur l'utilisation de nanoparticules magnétiques. Des nanoparticules magnétiques peuvent se lier à la membrane cellulaire, si leur surface a été recouverte de ligands appropriés. En utilisant un champ magnétique alternatif, il est possible de faire tourner les particules et /ou leur aimantation interne, ce qui entraîne une dissipation d'énergie et un échauffement local qui peut être utilisé pour détruire les tumeurs. Néanmoins, l'hyperthermie est difficile à réguler parce que les cellules tumorales ne sont que légèrement plus sensibles à l'élévation de température que les cellules saines. L'utilisation de nanoparticules allongées à la place de nanoparticules sphériques pourrait permettre de combiner l'effet thermique et l'endommagement mécanique.

Comme l'indique le titre de cette thèse, Rhéologie et magnétolyse des cellules tumorales, ce travail a deux objectifs principaux. La première porte sur l'étude des propriétés rhéologiques des cellules tumorales, et le second sur l'utilisation de nano/micro particules magnétiques pour détruire ces cellules.

Il y a un célèbre proverbe chinois de Sun Tzu, ancien général chinois, stratége et philosophe auteur de L'Art de la Guerre, qui dit: «Qui connaît son ennemi comme il se connaît, en cent combats ne sera point défait. »

Dans le but de combattre cet ennemi qu'est la cellule tumorale par des moyens de microécanique, la première partie de ce travail porte sur la manière d'obtenir des informations sur les propriétés mécaniques de ces cellules. Nous avons commencé avec l'idée de suivre le

mouvement de microsondes pour obtenir leurs propriétés rhéologiques. Dans une première approche en utilisant un fluide newtonien, nous avons suivi le mouvement d'une aiguille en présence d'un champ alternatif et comparé ce mouvement angulaire avec un modèle micromécanique qui prédit l'intensité du champ magnétique et la fréquence nécessaires pour obtenir un mouvement oscillatoire des aiguilles. Nous avons également utilisé le mouvement de translation sous un gradient de champ magnétique pour mesurer la viscosité. Ensuite, nous avons étudié le mouvement de petites sondes magnétiques (sphère, fibre et plaque) dans un milieu viscoélastique montrant qu'il était possible d'obtenir les propriétés viscoélastiques d'un gel par cette méthode décrite dans le chapitre 3.

Bien qu'elles soient réalisables en principe, ces expériences sont difficiles à conduire à l'échelle de cellules avec des particules de l'ordre du micron; il est plus facile d'utiliser des particules microniques attachées au cantilever d'un AFM afin de mesurer les propriétés viscoélastiques de cellules tumorales. Cette méthode et les résultats obtenus sont présentés au chapitre 4.

La deuxième partie de ce travail est consacrée à l'utilisation de micro ou nanoparticules magnétiques dans le but de détruire les cellules soit mécaniquement, soit par un effet thermique. Le chapitre 5 décrit la synthèse et la caractérisation de ces particules. Dans le chapitre 6, nous étudions l'effet sur la mortalité des cellules cancéreuses, d'un gradient de champ alternatif appliqué sur les microparticules qui ont sédimenté sur la surface des cellules. Dans le dernier chapitre, nous avons examiné la possibilité d'élever la température des cellules avec des nanoparticules d'environ 100 nm, plus grandes que celles d'un ferrofluide (environ 10 nm) qui sont généralement considérées pour des applications d'hyperthermie, mais encore assez petites pour diffuser à l'intérieur du tissu tumoral.

«If you know the enemy and know yourself, you need not fear the result of a hundred battles. »

Sa Tzu, The Art of War

Cancer is the N°1 public enemy for the society and numerous strategies have been developed to fight against it. One of them is based on the use of magnetic nanoparticles. Magnetic nanoparticles can bind to the cell membrane if their surface has been coated with appropriated ligands. Using an alternating magnetic field, it is possible to rotate the particles and/or their internal magnetization, resulting in energy dissipation and local temperature rise that can be used to destroy tumors. Nevertheless, hyperthermia is difficult to regulate because the tumor cells are only slightly more sensitive to temperature rise than healthy cells. The use of elongated nanoparticles instead of spherical one could provide both thermal and mechanical damage.

As indicated by the title of this thesis, *Rheology and magnetolysis of tumor cell*, there are two main objectives of this work, the first one about the study of the rheological properties of tumor cells, and the second one on the use of magnetic micro or nanoparticles to destroy these cells.

There is one celebrated saying about enemy by ***Sun Tzu***, an ancient Chinese military general, strategist and philosopher, author of ***The Art of Wa***r, «If you know the enemy and know yourself, you need not fear the result of a hundred battles. »

Since we want to kill this enemy mechanically, the first part of this work is about the way to obtain information on the mechanical properties of the tumor cells. We have started with the idea to follow the motion of microprobes to get the rheological behavior. In a first approach on a Newtonian fluid, we have followed the motion of a needle in the presence of an alternative field and compared this angular motion with the prediction of a micromechanical model, which gives the magnetic field intensity and the frequency necessary to obtain a swinging motion of the needles; also the translational motion under a magnetic field gradient was used to measure the viscosity. In a second step we have studied the motion of small magnetic probes (sphere, needle or plate) in a viscoelastic medium showing that it was possible to access the viscoelastic properties of a gel by these means; this is described in

chapter 3. Although feasible in principle these experiments are difficult to make at the scale of cells with probes of size around one micron, so finally we performed experiments with a micronic particle attached to an AFM cantilever in order to measure the viscoelastic properties of tumor cells; the method and the results are presented in chapter 4.

The second part of this work is devoted to the use of magnetic micro or nanoparticles which will be used for the purpose of destroying the cells either mechanically or by a heating effect. Chapter 5 describes the synthesis and characterization of these particles. In chapter 6, we study the effect, on the viability of cancer cells, of an alternative field gradient applied on the microparticles, which were sediment on the surface of the cells. In the last chapter, we examine the possibility to heat the cells with nanoparticles whose sizes (about 100 nm) are larger than the ones of a ferrofluid (about 10 nm), which are usually considered for hyperthermia applications, but still small enough to diffuse inside the tumor tissue.

2. STATE OF THE ART

2.1. Cancer

2.1.1. Tumor, cancer, metastasis

The term tumor is, in medicine, an increasing volume of tissue, clearly delineated without specifying cause. It is a formation of new body tissue (neoplasm) that occurs as a result of a deregulation of cell growth, like benign or malignant.

Neoplasm is an abnormal mass of tissue as a result of neoplasia. Neoplasia ("new growth" in Greek) is the abnormal proliferation of cells. The growth of neoplastic cells exceeds and is not coordinated with that of the normal tissues around it. The growth persists in the same excessive manner even after cessation of the stimuli. It usually causes a lump or tumor. Neoplasms may be benign, pre-malignant (carcinoma in situ) or malignant (cancer).

Benign tumors are usually not harmful and grow slowly. They are also localized and has not spread (metastasize) to other parts of the body or invaded and destroyed nearby tissue. Benign tumors affecting the skin are still often seen as unsightly and can lead to ablation. However, a benign tumor can cause serious complications (compression, ignition ...) by its mechanical action.

Potentially malignant neoplasms include carcinoma in situ. They do not invade and destroy but, given enough time, will transform into a cancer.

Malignant neoplasms are commonly called cancer, they are ambitious. Unlike benign tumors that generally stay in place, malignant tumors have two goals in life: to survive and to conquer new territory. They invade and destroy the surrounding tissue, may form metastases and eventually kill the host.

Metastasis is the spread of a disease from one organ or part to another non-adjacent organ or part. A cancer can affect any type of tissue. Depending on the location of the tumor and function of the affected tissue, it can lead to organ dysfunction and affect the whole body and even cause his death.

Determining what causes cancer is complex. Many things are known to increase the risk of cancer, including tobacco use, certain infections, radiation, lack of physical activity, poor diet and obesity, and environmental pollutants(1). The tumors occur in all living beings, including plants.

2.1.2. Number and cost about cancer

A study by the International Agency for Research on Cancer (IARC, an offshoot of the World Health Organization), cancer killed 7.6 million people, mostly in developing countries in 2008 , 12.7 million new cases of cancer were diagnosed, while in 2000 the number was 10 million and in 1975 it was 5.9 million(2).

As to France, there are 146,500 cancer deaths estimated in 2010, 84,500 men and 62,000 women. For the period 2003-2007, cancer is the leading cause of death in men and second in women(3).

The most commonly diagnosed cancers in the world are those of the lung (12.7%), breast (10.9%) and colorectal cancer (9.7%). The most common deaths are caused by lung cancer (18.2%), stomach cancer (9.7%) and liver cancer (9.2%)(2).

In France, in men, lung cancer is the leading cause of death, followed by colorectal cancer and prostate cancer. In women, it is breast cancer followed by colorectal cancer and lung cancer(3).

Chemotherapy and major surgery and the long-term treatment of cancer are one of the most financially costly diseases to society. The social cost of cancer is difficult to assess, but is important and continues to grow(4).

In France in the 2000s, about 280,000 new cases were detected per year, with a steady rise in the number of cases (358,000 new cases expected in 2010 according to the modeling of the INVS (made necessary by the fact that in France, only about 20% of the population is concerned by a cancer registry) annual cost estimated to be 30 billion Euros in 2004. 730 million Euros were granted in the 2nd Plan of cancer (2009-2013) of which 95 million for research and 400 million for care. The research also focuses on ways to reduce the socio-economic costs of the disease and the health care(3).

2.1.3. Classic treatments of cancer

Surgery In theory, non-hematological cancers can be cured if entirely removed by surgery, but this is not always possible. When the cancer has metastasized to other sites in the body prior to surgery, complete surgical excision is usually impossible.

Chemotherapy is the treatment of cancer with drugs ("anticancer drugs") that can destroy cancer cells. In current usage, the term "chemotherapy" usually refers to cytotoxic drugs which affect rapidly dividing cells in general, in contrast with targeted therapy. Because some drugs work better together than alone, two or more drugs are often given at the same time. This is called "combination chemotherapy"; most chemotherapy regimens are given in a combination.

This technique has a range of side effects that depend on the type of medications used. The common side effects include: depression of the immune system, physically exhausting for the patient, the tendency to bleed easily, the gastrointestinal distress, like nausea and vomiting, and hair loss, and so on.

Hormonal therapy is used for several types of cancers derived from hormonally responsive tissues, including the breast, prostate, endometrium, and adrenal cortex. Because steroid hormones are powerful drivers of gene expression in certain cancer cells, changing the levels or activity of certain hormones can cause certain cancers to cease growing, or even undergo cell death.

Radiation therapy is the use of ionizing radiation to kill cancer cells and shrink tumors. The effects of radiation therapy are localized and confined to the region being treated. Radiation therapy injures or destroys cells in the area being treated (the "target tissue") by damaging their genetic material, making it impossible for these cells to continue to grow and divide. Although radiation damages both cancer cells and normal cells, most normal cells can recover from the effects of radiation and function properly. The goal of radiation therapy is to damage as many cancer cells as possible, while limiting harm to nearby healthy tissue. Hence, it is given in many fractions, allowing healthy tissue to recover between fractions. Thus, as with every form of treatment, radiation therapy is not without its side effects.

Immunotherapy is the use of the immune system to reject cancer. The main premise is stimulating the patient's immune system to attack the malignant tumor cells that are responsible for the disease. This can be either through immunization of the patient, in which case the patient's own immune system is trained to recognize tumor cells as targets to be destroyed, or through the administration of therapeutic antibodies as drugs, in which case the patient's immune system is recruited to destroy tumor cells by the therapeutic antibodies. Cell based immunotherapy is another major entity of cancer immunotherapy. This involves immune cells such as the Natural killer Cells (NK cells), Lymphokine Activated killer cell(LAK), Cytotoxic T Lymphocytes(CTLs), Dendritic Cells (DC), etc., which are either activated in vivo by administering certain cytokines such as Interleukins or they are isolated, enriched and transfused to the patient to fight against cancer.

Besides these “classical” treatments, new approaches are emerging based on the use of magnetic nanoparticles which can be focused on the tumor cells and activated from outside by the application of a magnetic field.

2.1.4. Hyperthermia therapy

- ***Principle and Mechanism***

Hyperthermia therapy is a type of medical treatment in which body tissue is exposed to slightly higher temperatures to damage and kill cancer cells or to make cancer cells more sensitive to the effects of radiation and certain anti-cancer drugs(4).

Tumor cells, with a disorganized and compact vascular structure, have difficulty dissipating heat. Hyperthermia may therefore cause cancerous cells to undergo apoptosis in direct response to applied heat, while healthy tissues can more easily maintain a normal temperature. Even if the cancerous cells do not die outright, they may become more susceptible to ionizing radiation therapy or to certain chemotherapy drugs, which may allow such therapy to be given in smaller doses.

Intense heating will cause denaturation and coagulation of cellular proteins, rapidly killing cells within a tumor. More prolonged moderate heating to temperatures just a few degrees above normal can cause more subtle changes. A mild heat treatment combined with other stresses can cause cell death by apoptosis. There are many biochemical consequences to the

heat shock response within cell, including slowed cell division and increased sensitivity to ionizing radiation therapy.

Hyperthermia can increase blood flow to the warmed area, perhaps doubling perfusion in tumors, while increasing perfusion in normal tissue by ten times or even more(5). This enhances the delivery of medications. Hyperthermia also increases oxygen delivery to the area, which may make radiation more likely to damage and kill cells, as well as preventing cells from repairing the damage induced during the radiation session.(6)

Cancerous cells are not inherently more susceptible to the effects of heat (5). When compared in vitro studies, normal cells and cancer cells show the same responses to heat. However, the vascular disorganization of a solid tumor results in an unfavorable microenvironment inside tumors. Consequently, the tumor cells are already stressed by low oxygen, higher than normal acid concentrations, and insufficient nutrients, and are thus significantly less able to tolerate the added stress of heat than a healthy cell in normal tissue(5). Then in practice most local and regional cancer treatments are made in the temperature range of 40 to 42 °C. Very high temperatures, above 50 °C (122 °F), are used for ablation (direct destruction) of some tumors.(6) This generally involves inserting a metal tube directly into the tumor, and heating the tip until the tissue next to the tube has been killed.

Many sources of energy for localized hyperthermia treatment were developed in the last two decades.

The minimally invasive devices must be inserted inside the tumor in order to apply, microwave, radio frequency (RF) or laser beams.

Non-invasive devices, for which the energy source is placed outside the body, use focused ultrasound.

Magnetic Hyperthermia requires the injection of magnetic nanoparticles in the tumor and the application of an external alternating magnetic field.

- ***Controlling temperatures***

One of the challenges in thermal therapy is to deliver the appropriate amount of heat to the correct part of the patient's body. For this technique to be effective, the temperatures must be high enough, and the temperatures must be sustained long enough, to damage or kill the

cancer cells. However, if the temperature is too high, or if it is kept elevated for too long, then serious side effects, including death can result. The smaller the place that is heated the shorter the treatment time, the lower the side effects(7).

To minimize damage to healthy tissue and other adverse effects, physicians carefully monitor the temperature of the affected area. The goal is to keep local temperatures under 44 °C to avoid damage to surrounding tissues, and the whole body temperature smaller than 42 °C, which is the upper limit compatible with life. These temperatures compare to the normal human body temperature, taken internally, of about 37.6 °C.

2.1.5. Magnetic hyperthermia

- ***Definition***

Magnetic hyperthermia is based on the fact that magnetic nanoparticles, when subjected to an alternating magnetic field, produce heat(8). As a consequence, if magnetic nanoparticles are put inside a tumor and the whole patient is placed in an alternating magnetic field of well-chosen amplitude and frequency, the tumor temperature would raise. This could kill the tumor cells by necrosis if the temperature is above 45 °C, or could improve the efficiency of chemotherapy if the temperature is raised around 42 °C(9).

A general feature of many magnetic materials is to display a magnetic hysteresis when it is submitted to an alternative magnetic field. The area of this hysteresis loop is dissipated in the environment under the form of thermal energy. This is the energy used in magnetic hyperthermia.

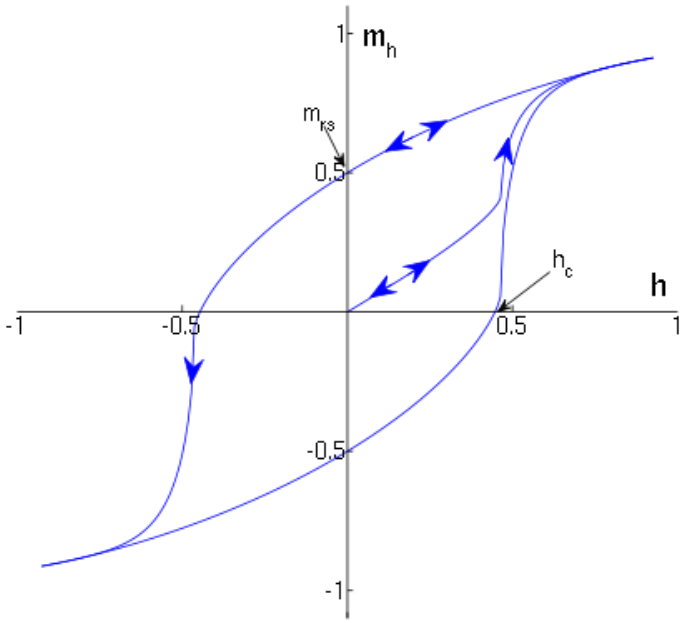

Fig. 2-1: A plot of magnetization m against magnetic field h calculated using a theoretical model.

Starting at the origin, the upward curve is the initial magnetization curve. The downward curve after saturation, along with the lower return curve, forms the main loop. The intercepts h_c is the coercive field and m_{rs}, the remanent magnetization.

The power dissipated by a magnetic material subjected to an alternative magnetic field is often called "**Specific Absorption Rate**" (SAR) in the community of magnetic hyperthermia.

The SAR of a given material is simply given by:

$$SAR = Af \qquad (2.1)$$

Where A is the area of the hysteresis loop vs. f the frequency of the magnetic field.

A is expressed in J/g and is also called "**specific losses**" of the material. It should be noted that this expression is always true; whatever can be the complexity of determining A. Indeed, as will be shown in more details below, *A*, depends on a very complex manner on all the properties of the magnetic material. In the case of magnetic nanoparticles, it depends on their magnetocrystalline anisotropy *K*, their volume *V*, the temperature *T*, and the frequency of the magnetic field *f*, its amplitude H_{max} and on the volume concentration of the nanoparticles which influences the magnetic interactions between them(10).

2.1.6. Composition of tumor cell

Like normal cell, the tumor cell contain 70% of water(11); By mass, human cells consist of 65–90% water (H_2O), and the estimated gross molecular content of a typical 20 micrometer human cell is as follows (12):

Molecule	% of Mass	Mol. Weight (Daltons)	Number of Molecules	% of Molecules
Water	65	18	1.74E+14	98.73
Protein	20	50000	1.90E+10	0.011
Lipids	12	700	8.40E+11	0.475
Other Inorganic	1.5	55	1.31E+12	0.74
RNA	1	1.00E+06	5.00E+07	3.00E-05
Other Organics	0.4	250	7.70E+10	0.044
DNA	0.1	1.00E+11	46	3.00E-11

Tab. 2-1: Estimated gross molecular content of a typical 20 micrometer human cell

2.2. Rheology

Rheology is the study of the deformation and flow of matter under the effect of an applied stress. The term was inspired by the aphorism of Simplicius, panta rei, "everything flows".(13) It applies to substances which have a complex molecular structure, such as muds, sludges, suspensions, polymers, as well as many foods and additives, body fluids (e.g. blood) and other biological materials, like tumors. If one wants to destroy the tumors mechanically, we must know better the tumor's rheological properties, that's why in the following topic, we are going to look to some rheological problem.

2.2.1. Stress, strain and strain rate

Stress is a measure of the internal forces acting within a deformable body. Quantitatively, it is a measure of the average force per unit area of a surface within the body on which internal forces act. These internal forces are a reaction to external forces applied on the body.

The dimension of stress is the one of pressure, and therefore the SI unit for stress is the Pascal (symbol Pa), it's equivalent to N/m2.

More often we consider two kinds of stress, normal stress and shear stress:

For the simple case of an axially loaded body, for instance a bar subjected to tension or compression by a force passing through its center, Fig. 2-2 ,the stress is obtained by dividing the total normal force F by the bar's cross-sectional area A:

$$\sigma = \frac{F}{A} \tag{2.2}$$

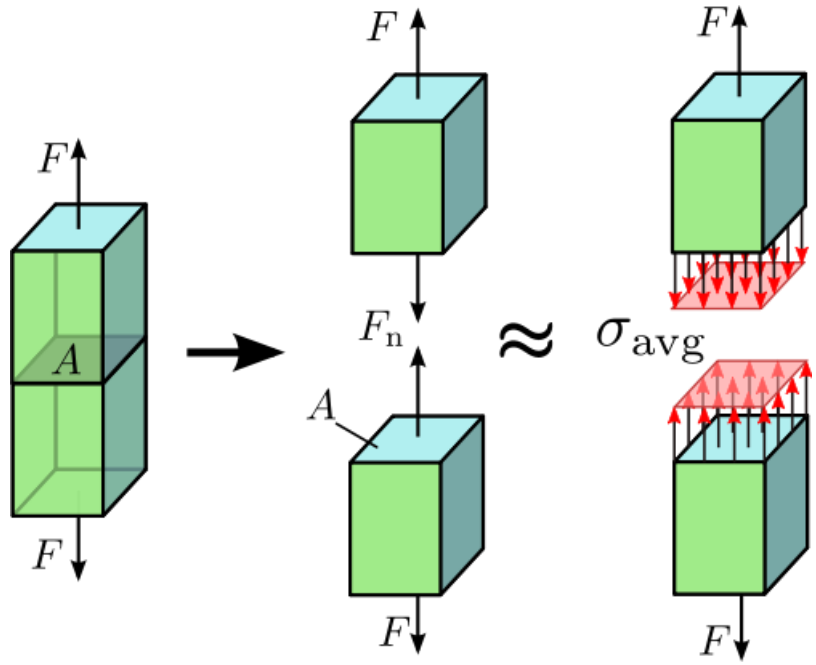

Fig. 2-2: Axial stress in a prismatic bar axially loaded

Shear stress is a different type of stress, the force F occurs in shear, as shown in Fig. 2-3. The force here is called the shear force. Dividing the shear force F by the cross-sectional area A, we obtain the shear stress τ.

$$\tau = \frac{F}{A} \tag{2.3}$$

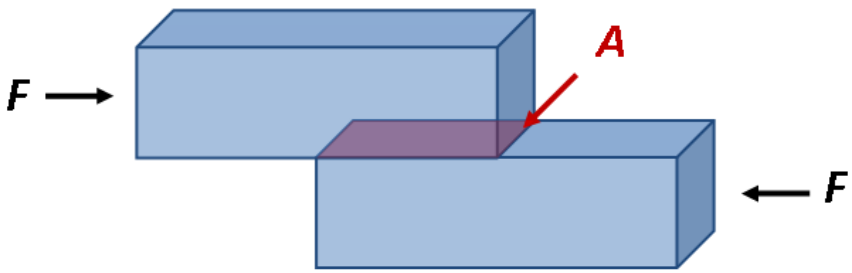

Fig. 2-3: Shear stress in a prismatic bar. The stress is not necessarily uniform.

The strain is a normalized measure of deformation representing the displacement from a reference configuration to a current configuration. As with stresses, strains may also be classified as 'normal strain' and 'shear strain' (acting perpendicular to or along the face of an element respectively). As shown in Fig. 2-4, normal strain are $\varepsilon_X = \frac{\triangle X}{X}$ and $\varepsilon_Y = \frac{\triangle Y}{Y}$, and shear strain are $\varepsilon_{XY} = \frac{\triangle X}{Y}$ and $\varepsilon_{YX} = \frac{\triangle Y}{X}$.

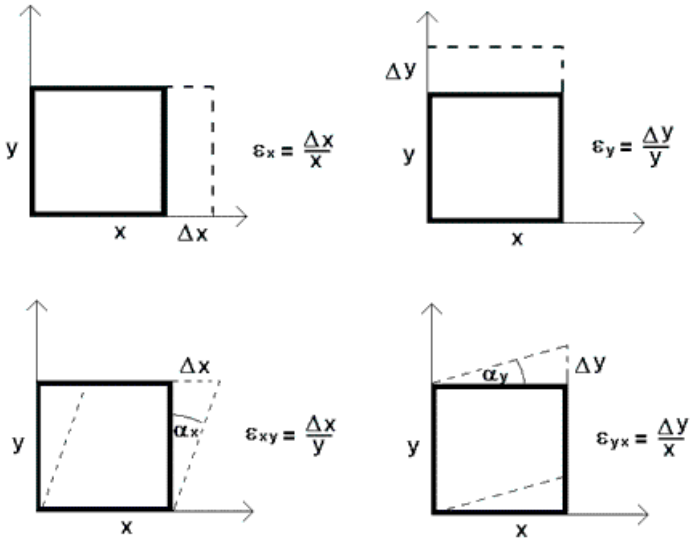

Fig. 2-4: Two-dimensional geometric deformation of an infinitesimal material element

In a solid, shear stress is a function of strain, but in a fluid, shear stress is a function of strain rate.

Strain rate is the rate of change in strain with respect to time and is denoted as:

$$\dot{\varepsilon} = \frac{d\varepsilon}{dt} \tag{2.4}$$

So it is also the speed at which deformation of an object from its original shape occurs.

2.2.2. Newtonian fluid, Hookean solid and yield stress

A Newtonian fluid is a fluid whose stress versus strain rate is linear and passes through the origin. The constant of proportionality is known as the viscosity. A simple equation to describe a Newtonian fluid behavior is

$$\tau = \eta\dot{\varepsilon} = \eta\frac{du}{dy} \qquad (2.5)$$

Where τ is the shear stress exerted by the fluid [Pa]

η is the fluid viscosity [Pa·s]

$\frac{du}{dy}$ is the velocity gradient perpendicular to the direction of velocity, or equivalently the shear rate [s^{-1}]

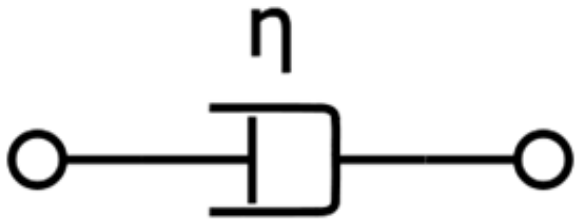

Fig. 2-5 : Model of a Newtonian fluid, a dashpot

Mathematically, Hooke's law states that

$$F = -k.\Delta x = -E\frac{S}{l}\Delta x \quad or \quad \sigma = E.\varepsilon \qquad (2.6)$$

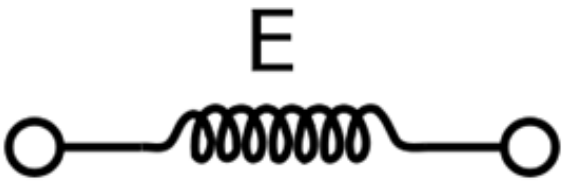

Fig. 2-6 : Model of an elastic solid, a spring

Where E is the Young modulus S the section of the sample and l its length

The yield strength or yield point of a material is defined in engineering and materials science as the stress at which a material begins to deform plastically. Prior to the yield point the material will deform elastically and will return to its original shape when the applied stress is removed. Once the yield point is passed, some fraction of the deformation will be permanent and non-reversible.

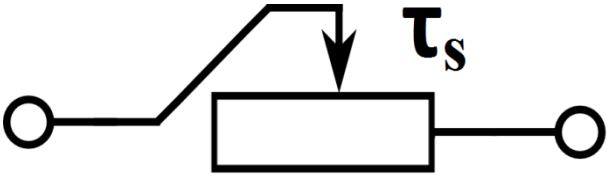

Fig. 2-7 : Model of a yield stress, a switch

2.2.3. Maxwell model and Kelvin-Voigt Model

Maxwell model describes the dashpot as a Newtonian fluid and models the spring with Hooke's law. It's a viscoelastic liquid, as show in Fig. 2-8. In this configuration, under an applied axial stress, the total stress and the total strain can be defined as follows, D for dashpot and S for spring:

$$\sigma_{Total} = \sigma_D = \sigma_S \tag{2.7}$$

$$\varepsilon_{Total} = \varepsilon_D + \varepsilon_S \tag{2.8}$$

Taking the derivative of strain with respect to time, we obtain:

$$\frac{d\varepsilon_{Total}}{dt} = \frac{d\varepsilon_D}{dt} + \frac{d\varepsilon_S}{dt} = \frac{\sigma}{\eta} + \frac{1}{E}\frac{d\sigma}{dt} \tag{2.9}$$

$$\dot{\varepsilon} = \frac{\sigma}{\eta} + \frac{\dot{\sigma}}{E} \tag{2.10}$$

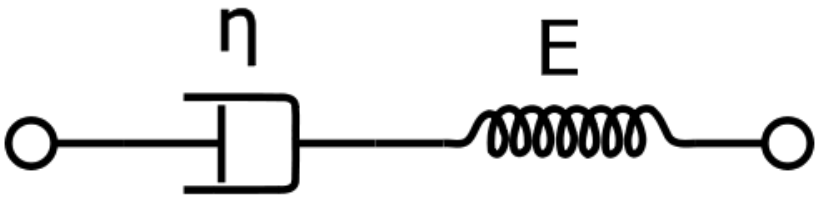

Fig. 2-8 : Maxwell model, a dashpot and a spring in series

If a Maxwell material is suddenly subjected to a stress σ_0, then the elastic element would suddenly deform and the viscous element would deform with a constant rate:

$$\varepsilon(t) = \frac{\sigma_0}{E} + \frac{\sigma_0}{\eta}t \tag{2.11}$$

Kelvin Voigt model is represented by a purely viscous dashpot and purely elastic spring connected in parallel as shown in Fig. 2-9 the picture. It's a model for viscoelastic solid.

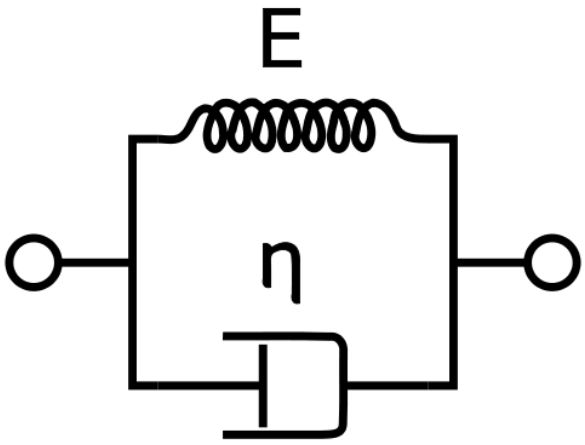

Fig. 2-9 : Model of Kelvin-Voigt, a dashpot and a spring in parallel

Since the two components of the model are arranged in parallel, the strains in each component are identical:

$$\varepsilon_{Total} = \varepsilon_D = \varepsilon_S \tag{2.12}$$

Similarly, the total stress will be the sum of the stress in each component:

$$\sigma_{Total} = \sigma_D + \sigma_S \tag{2.13}$$

From these equations we get that in a Kelvin–Voigt material, the stress σ, the strain ε and their rates of change with respect to time t are governed by equation:

$$\sigma(t) = E\varepsilon(t) + \eta\frac{d\varepsilon(t)}{dt} \tag{2.14}$$

. The equation can be applied either to the shear stress, in this case the shear modulus G replaces the Yong modulus or to the normal stress of a material.

If we suddenly apply some constant stress σ_0 to a Kelvin–Voigt material, then the deformation would approach the deformation for the pure elastic material σ_0/E with the difference decaying exponentially:

$$\varepsilon(t) = \frac{\sigma_0}{E}\left(1 - e^{-\lambda t}\right) \tag{2.15}$$

Where t is time and λ the rate of relaxation

$$\lambda = \frac{E}{\eta} \tag{2.16}$$

2.2.4. More complex model

There are some more complex models, such as Bingham model, Zener model, and Generalized Maxwell Model.

The Bingham model

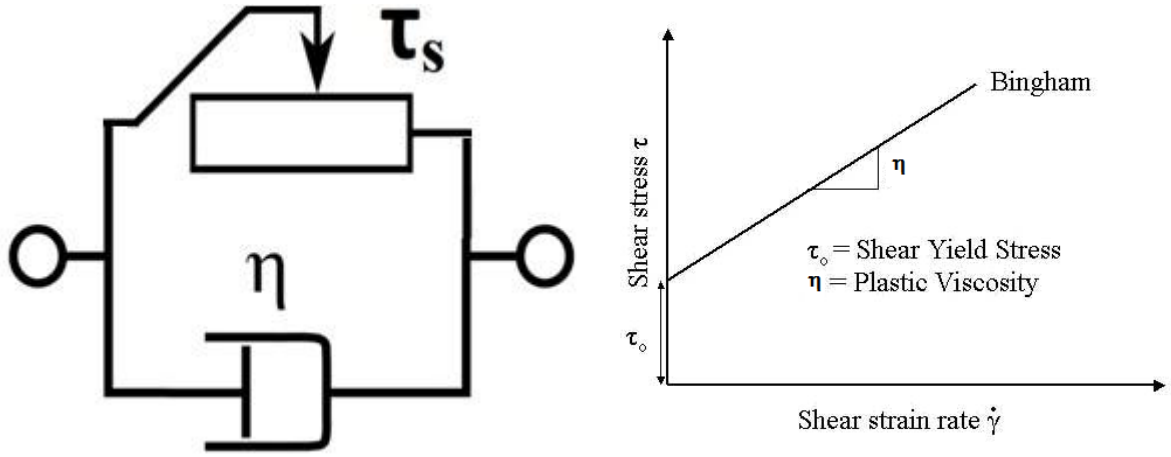

Fig. 2-10 : Model of Bingham, a dashpot and a switch in parallel

The Zener Model effectively combines the Maxwell Model and a Hookean spring in parallel. A viscous material is modeled as a spring and a dashpot in series with each other, both of which are in parallel with a spring. For this model, the governing constitutive relation is:

$$\frac{d\varepsilon}{dt} = \frac{\frac{E_2}{\eta}\left(\frac{\eta}{E_2}\frac{d\sigma}{dt} + \sigma - E_1\varepsilon\right)}{E_1 + E_2} \tag{2.17}$$

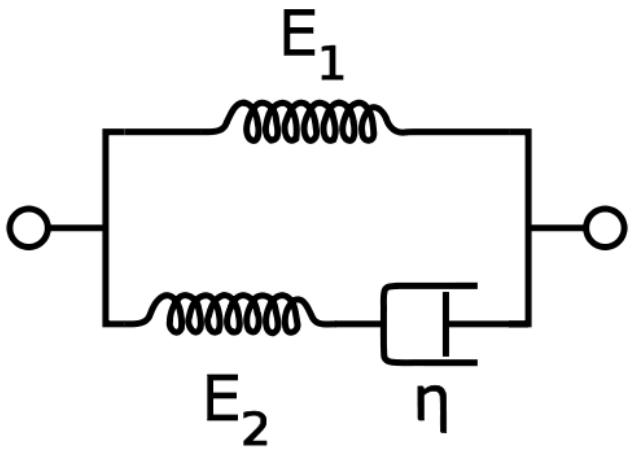

Fig. 2-11 : Schematic representation of the Zener model

The Generalized Maxwell model also known as the Maxwell–Wiechert model, is the most general form of the linear model for viscoelasticity. It takes into account that the relaxation does not occur at a single time, but as a distribution of times. Due to molecular segments of different lengths with shorter ones contributing less than longer ones, there is a varying time distribution. The Wiechert model takes into account this behavior by having as many spring–dashpot Maxwell elements as necessary to accurately represent the distribution. The figure on the right shows the generalized Wiechert model.

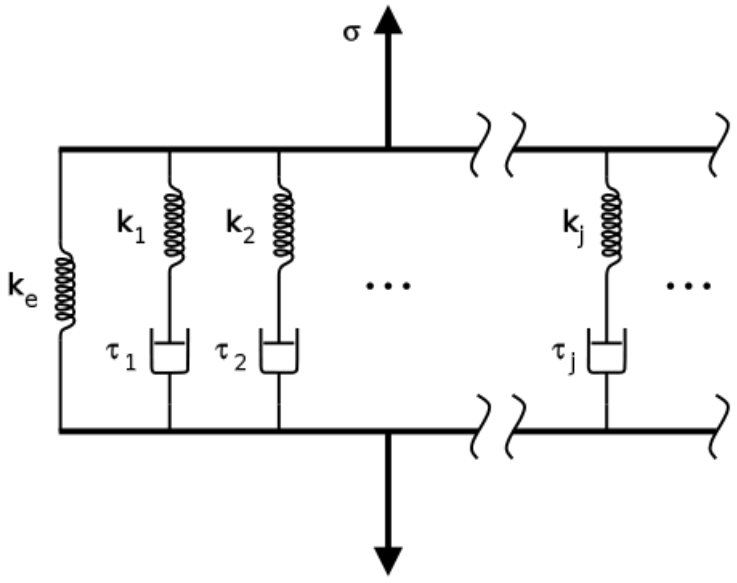

Fig. 2-12 : Schematic of Maxwell-Wiechert Model

2.3. Magnetic nanoparticles

Magnetic nanoparticles are a class of nanoparticles which can be manipulated using magnetic field. Such particles commonly consist of magnetic elements such as iron, nickel and cobalt and their chemical compounds. While nanoparticles are smaller than 1 micrometer in diameter (typically 5–500 nanometers), the larger microbeads are 0.5–500 micrometer in diameter. The magnetic nanoparticles have been the focus of much research recently because they possess attractive properties, which could see potential use in catalysis(14), biomedicine(15), magnetic resonance imaging, magnetic particle imaging(16), etc.

As described in section 2.1.5 magnetic nanoparticles are used in an experimental cancer treatment called magnetic hyperthermia using the fact that nanoparticles heat when they are placed in an alternative magnetic field is used.

Another potential treatment of cancer includes attaching magnetic nanoparticles to free-floating cancer cells, allowing them to be captured and carried out of the body. The treatment has been tested in the laboratory on mice and will be looked at in survival studies (17).

Magnetic nanoparticles can be used for the detection of cancer. Blood can be inserted onto a microfluidic chip with magnetic nanoparticles in it. These magnetic nanoparticles are trapped inside due to an externally applied magnetic field as the blood is free to flow through. The magnetic nanoparticles are coated with antibodies targeting cancer cells or proteins. The magnetic nanoparticles can be recovered and the attached cancer-associated molecules can be assayed to test for their existence.

Magnetic nanoparticles can be conjugated with carbohydrates and used for detection of bacteria. Iron oxide particles have been used for the detection of Gram negative bacteria like Escherichia coli and for detection of Gram positive bacteria like Streptococcus suis(18).

2.4. Atomic force microscopy (AFM)

Atomic force microscopy (AFM) is a very high-resolution type of scanning probe microscopy, with demonstrated resolution on the order of fractions of a nanometer, more than 1000 times better than the optical diffraction limit. AFM was invented by Gerd Binnig(19) in 1986.

The AFM is one of the foremost tools for imaging, measuring, and manipulating matter at the nanoscale. The information is gathered by "feeling" the surface with a mechanical probe. Piezoelectric elements that facilitate tiny but accurate and precise movements on (electronic) command enable a very precise scanning.

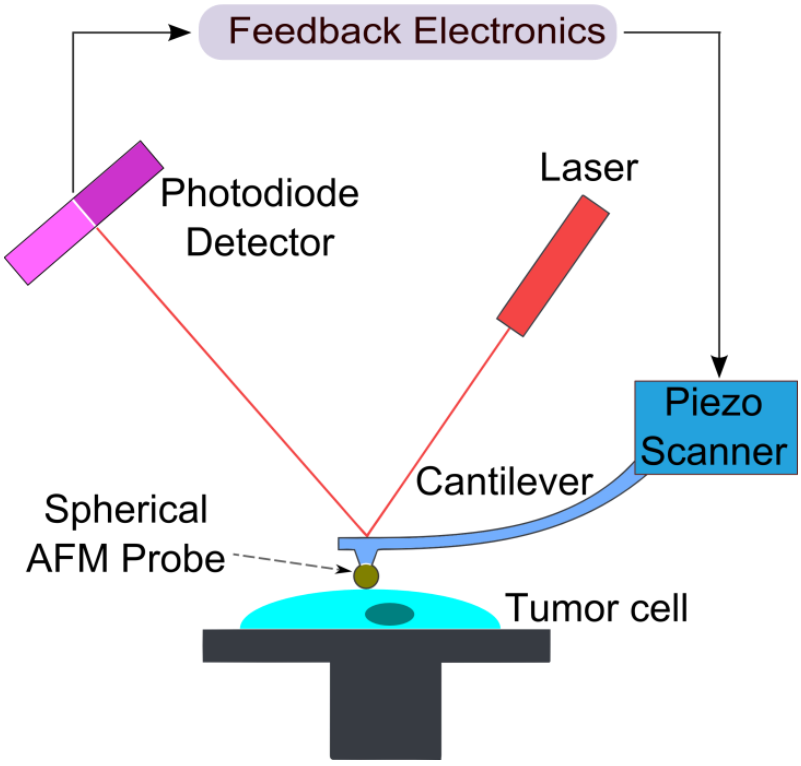

Fig. 2-13: Block diagram of atomic force microscope

2.4.1. Basic principles

The AFM consists of a cantilever with a sharp tip (probe) at its end that is used to scan the specimen surface. The cantilever is typically made of silicon or silicon nitride with a tip radius of curvature of the order of nanometers. When the tip is brought into proximity of a sample surface, forces between the tip and the sample lead to a deflection of the cantilever according to Hooke's law. Depending on the situation, forces that are measured in AFM include mechanical contact force, van der Waals forces, capillary forces, chemical bonding, electrostatic forces, magnetic forces, Casimir forces, solvation forces, etc.

Along with the force, additional quantities may simultaneously be measured through the use of specialized types of probe (see scanning thermal microscopy, scanning joule expansion

microscopy, photothermal microspectroscopy, etc.). Typically, the deflection is measured using a laser spot reflected from the top surface of the cantilever into an array of photodiodes. Other methods that are used include optical interferometry, capacitive sensing or piezoresistive AFM cantilevers. These cantilevers are fabricated with piezoresistive elements that act as a strain gauge. Using a Wheatstone bridge, strain in the AFM cantilever due to deflection can be measured, but this method is not as sensitive as laser deflection or interferometry.

If the tip is scanning the sample at a constant height, a risk would exist that the tip collides with the surface, causing damage. Hence, in most cases a feedback mechanism is employed to adjust the tip-to-sample distance to maintain a constant force between the tip and the sample. Traditionally, the sample is mounted on a piezoelectric tube that can move the sample in the z direction for maintaining a constant force, and in the x and y directions for scanning the sample. Alternatively a 'tripod' configuration of three piezo crystals may be employed, with each responsible for scanning in the x, y and z directions. This eliminates some of the distortion effects seen with a tube scanner. In newer designs, the tip is mounted on a vertical piezo scanner while the sample is being scanned in X and Y using another piezo block. The resulting map of the area z = f(x, y) represents the topography of the sample.

The AFM can be operated in a number of modes, depending on the application. In general, possible imaging modes are contact modes where the tip remains in contact with the sample with a constant deflection of the cantilever and non-contact modes where the cantilever is submitted to a vibration and it is the amplitude of the deflection which is kept constant.

2.4.2. Force spectroscopy

Besides imaging, another major application of AFM is force spectroscopy, the direct measurement of tip-sample interaction forces as a function of the gap between the tip and sample (the result of this measurement is called a force-distance curve).

For this method, the AFM tip is extended towards and retracted from the surface and the deflection of the cantilever is monitored as a function of piezoelectric displacement. These measurements have been used to measure nanoscale contacts, atomic bonding, Van der Waals forces, and Casimir forces, dissolution forces in liquids and single molecule stretching and rupture forces (20). Furthermore, AFM was used to measure, in an aqueous environment, the

dispersion force due to polymer adsorbed on the substrate (21). Forces of the order of a few piconewtons can now be routinely measured with a vertical distance resolution of better than 0.1 nanometers. Force spectroscopy can be performed with either static or dynamic modes. In dynamic modes, information about the cantilever vibration is monitored in addition to the static deflection (22).

Problems with the technique include no direct measurement of the tip-sample separation and the common need for low stiffness cantilevers which tend to 'snap' to the surface. The snap-in can be reduced by measuring in liquids or by using stiffer cantilevers, but in the latter case a more sensitive deflection sensor is needed. By applying a small dither to the tip, the stiffness (force gradient) of the bond can be measured as well(23).

3. USE OF MAGNETIC PARTICLES TO PROBE THE RHEOLOGY

A way to access the rheological properties of cancer cells is to use magnetic microparticles as probes and to look at their motion in the presence of a magnetic field. In order to check the validity of this approach, we have begun to study the motion of bigger particles, which are easier to follow by optical microscopy and which are well defined relatively to their shape and magnetic properties. We have used known suspending medium, firstly a Newtonian fluid in which we have studied the rotation and translation of a magnetic, this is described in section 3.1. Then we have analyzed the translational motion of probes of different shapes (sphere, needle, plate) inside a gel whose rheological properties were also measured by conventional rheometry; this is described in section 3.2 .

3.1. Motion of a fiber in a Newtonian fluid

3.1.1. Experimental setup

The experimental setup consists essentially of a homemade inverted microscope and a high speed camera (900fps) connected to a special system of ten parallel disks to record the images of the motion of the probe with enough optical resolution. Two coils in Helmholtz configuration are used for applying a constant magnetic field, cf. Fig. 3-1.

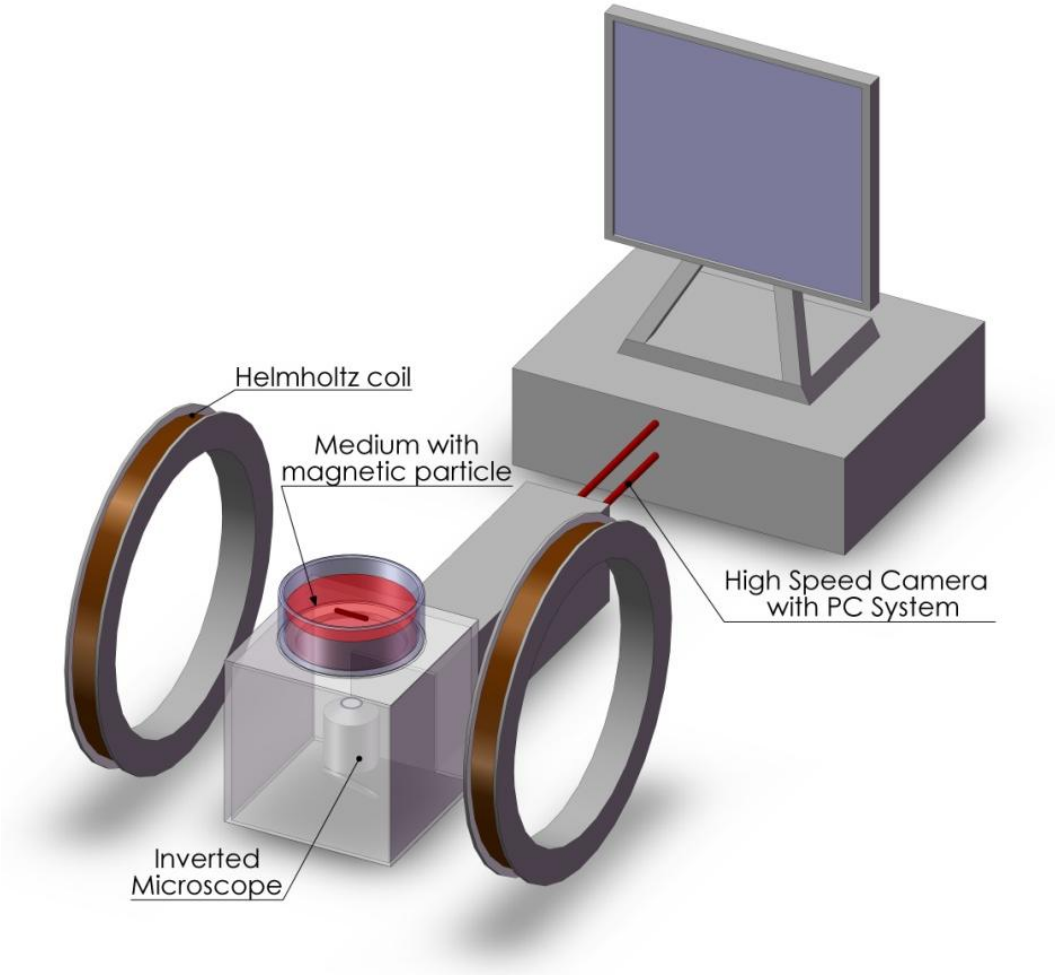

Fig. 3-1 : Experimental setup

3.1.2. Rotation

First of all, it's interesting to discuss the rotation of a magnetic fiber, because compared to a spherical magnetic particle, the magnetic fiber experiences a magnetic torque, due to the shape anisotropy. One issue is to know under which condition the fiber can follow the oscillation of an alternative magnetic field.

- ***Theoretical study***

The equation of motion of can be written as(24):

$$I\frac{d^2\theta}{dt^2}+\Gamma_m+\Gamma_h=0 \qquad (3.1)$$

Where Γ_m and Γ_h are respectively the magnetic and hydrodynamic torque, θ is the angle between the magnetic force and the rod.

The moment of inertia *I* of a rod of length *L* and mass *m*, similar to our fiber is given by(25):

$$I = \frac{mL^2}{12} \tag{3.2}$$

In a Stokes fluid, the hydrodynamic torque Γ_h is always present, and is proportional to the angular velocity as:

$$\Gamma_h = \alpha \frac{d\theta}{dt} \tag{3.3}$$

where the hydrodynamic coefficient α is proportional to the viscosity:

$$\alpha = C \frac{\pi \eta L^3}{3} \tag{3.4}$$

The factor *C*, depends on the different models, but is always related to the aspect ratio ***a*** between the length *L* and the diameter of the fiber *D*: $a = \frac{L}{D}$. Fig. 3-2 shows the hydrodynamic torque as a function of this aspect ratio *a* for different models. There are no exact analytical solutions and the model rests on different approximations. For Batchelor model(26), in the case of cylinder, we have:

$$C(\varepsilon) = \frac{2 + 1.28\varepsilon}{2 - \varepsilon}\varepsilon + 1.109\varepsilon^3 \tag{3.5}$$

with: $\varepsilon(a) = \frac{1}{\ln(2a)}$,

and for a slender body,

$$C(\varepsilon) = \frac{8}{\varepsilon} \tag{3.6}$$

with: $\varepsilon(a) = \frac{1}{\ln(2a) - 0.5}$,

For the ellipsoidal Van de Ven model(27):

$$C(a) = \frac{2}{a^3 \delta(a)} \tag{3.7}$$

$$\delta(a) = \int_0^\infty \frac{1}{\left(a^2 + x\right)\sqrt{(1+x)^2\left(a^2 + x\right)}}\, dx$$

For the Wilhelm model(28):

$$C(a) = \frac{1.5}{\ln\left(\frac{a}{2}\right) + \frac{2.4}{a}} \tag{3.8}$$

For the Keshoju model(29):

$$C = 0.15 \quad (L \gg r) \tag{3.9}$$

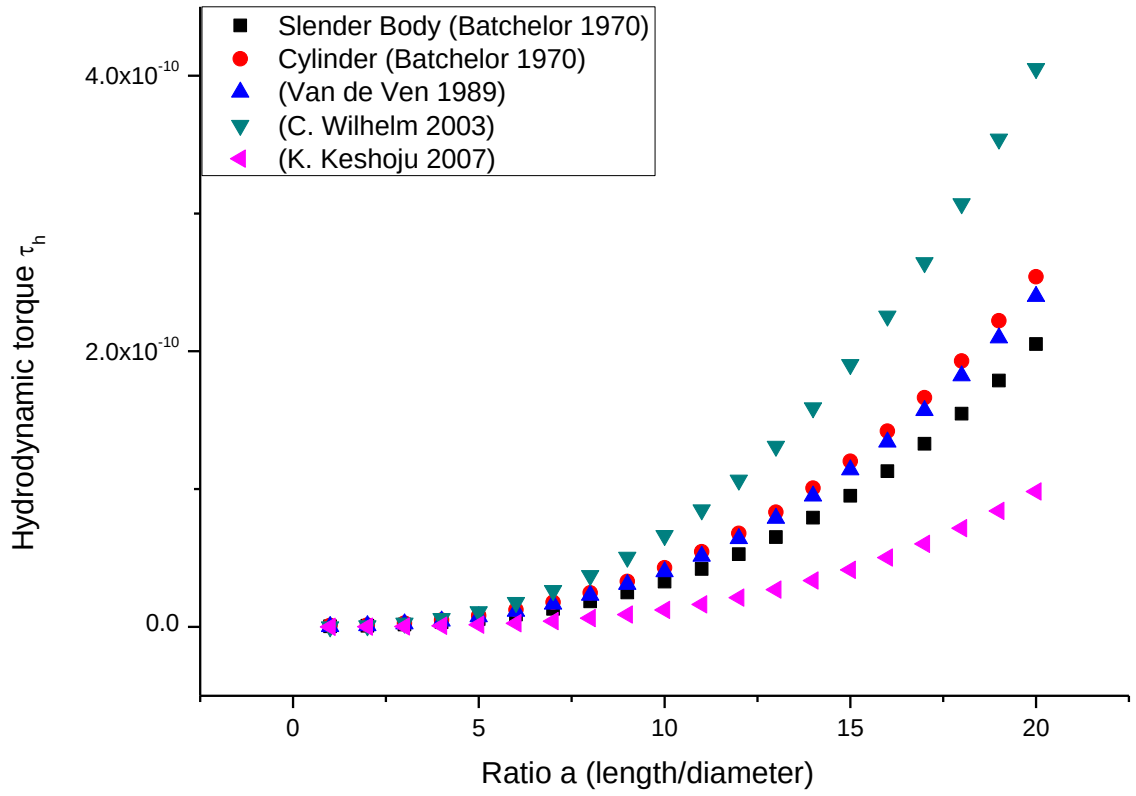

Fig. 3-2. Comparison of the different models used for the hydrodynamic torque

In conclusion, the model of a cylinder represented by Eq.(3.5), which is close to the well known slender body model and also to the model of ellipsoid of Van de Ven, will be the one used for the rest of the study.

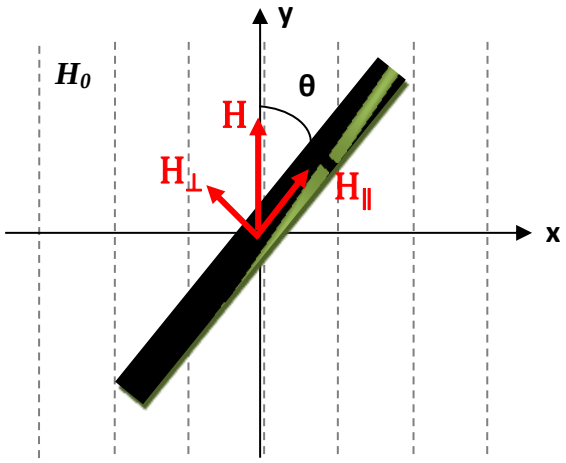

Fig. 3-3 : A rod-like fiber in a Newtonian fluid under an alternative magnetic field

The magnetic torque exerted by a magnetic field $\vec{H}$ on a magnetic moment $\vec{m}$ is expressed by:

$$\vec{\Gamma}_m = \vec{m} \times \vec{H} \tag{3.10}$$

The magnetic moment $\vec{m}$ is the magnetization $\vec{M}$ time the volume V of the particle:

$$\vec{m} = \mu_0 V \vec{M} \tag{3.11}$$

For the magnetization $\vec{M}$, we have two simple situations depending on the applied magnetic field.

1. *Case of induced magnetization*

If there is no remanent magnetization, the magnetization is a function of the magnetic field as:

$$\vec{M} = \chi_{(H)} \vec{H} \tag{3.12}$$

The components of the magnetization on the two directions, parallel and perpendicular to the fiber will be:

$$\begin{cases} M_{\parallel} = \chi_{(H)} H_{\parallel} = \chi_{(H)} H_0 \cos\theta \\ M_{\perp} = \chi_{(H)} \left(H_{\perp} - H_d \right) = \chi_{(H)} \left(H_0 \sin\theta - \frac{1}{2} M_{\perp} \right) \end{cases} \tag{3.13}$$

H_d is the demagnetizing field, given by (for a cylinder):

$$H_d = \frac{1}{2} M_\perp \tag{3.14}$$

Hence we shall have:

$$M_\perp = \frac{\chi_{(H)}}{1+\frac{\chi_{(H)}}{2}} H_0 \sin\theta \tag{3.15}$$

So the magnetic torque becomes,

$$\overrightarrow{\Gamma_m} = V\vec{M} \wedge \left(\mu_0 \vec{H}\right) = \mu_0 V \left(\overrightarrow{M_\parallel} \wedge \overrightarrow{H_\perp} + \overrightarrow{M_\perp} \wedge \overrightarrow{H_\parallel}\right) \tag{3.16}$$

$$\Gamma_m = \mu_0 V \chi_{(H)} \left[1 - \frac{1}{1+\frac{\chi_{(H)}}{2}}\right] {H_0}^2 \frac{\sin 2\theta}{2} \tag{3.17}$$

We can write it simply, in the presence of an alternative magnetic field $\mathrm{H} = \mathrm{H}_0 \cos(\omega t)$:

$$\Gamma_m = \beta_i \cos(\omega t)^2 \frac{\sin 2\theta}{2} \tag{3.18}$$

With

$$\beta_i = \mu_0 V \chi_{(H)} \left[\frac{\chi_{(H)}}{2+\chi_{(H)}}\right] {H_0}^2 \tag{3.19}$$

2. Case of remanent magnetization

In this case, the magnetic dipole moment is:

$$\overrightarrow{m_r} = \mu_0 V \overrightarrow{M_r} \tag{3.20}$$

$$\Gamma_r = \mu_0 V M_r H \sin\theta \tag{3.21}$$

Where $\overrightarrow{M_r}$ is the remanent magnetization along the axis of the fiber.

In presence of an alternative magnetic field $H = H_0 \cos(\omega t)$, the magnetic torque can be written as:

$$\Gamma_m = \beta_r \cos(\omega t) \sin\theta \qquad (3.22)$$

With

$$\beta_r = \mu_0 V M_r H_0 \qquad (3.23)$$

- ***Experimental study***

We have studied the motion of a nickel microfiber of diameter 10 µm and length 100 µm. To avoid the sinking of the fiber we placed it at the interface between two immiscible Newtonian fluids presenting the same viscosity. We have used for that, silicone oil on one hand and a mixture of ethylene glycol (60% w/w) with water (40% w/w) on the other hand. This proportion was chosen for obtaining the same viscosity as the one of silicone oil as shown in Fig. 3-4.

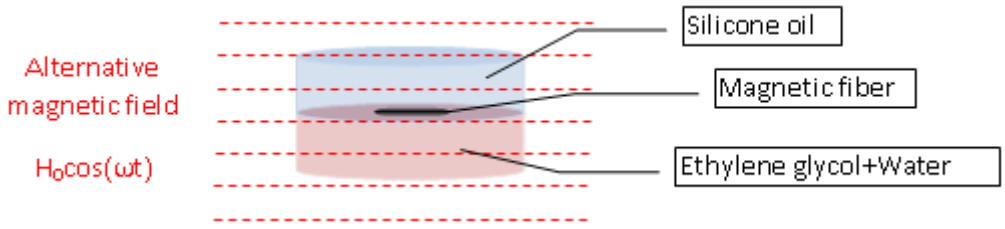

Fig. 3-4: Schematic view of the fiber at the interface of two fluids

The rotation of the fiber at this interface has been observed with the device represented in Fig. 3-1 and the evolution of the angle of the fiber relatively to the direction of the field was obtained by analyzing each image with the software ImageJ.

The **Erreur ! Source du renvoi introuvable.** below represents the rotation of the microfiber of pure nickel, for two applied magnetic field 1.4*G* and 27.8*G*, at a frequency *f*=2*Hz*. We can see that for the higher magnetic field the fiber stays a longer time aligned with the magnetic field with an abrupt change of orientation when the field changes of sign.

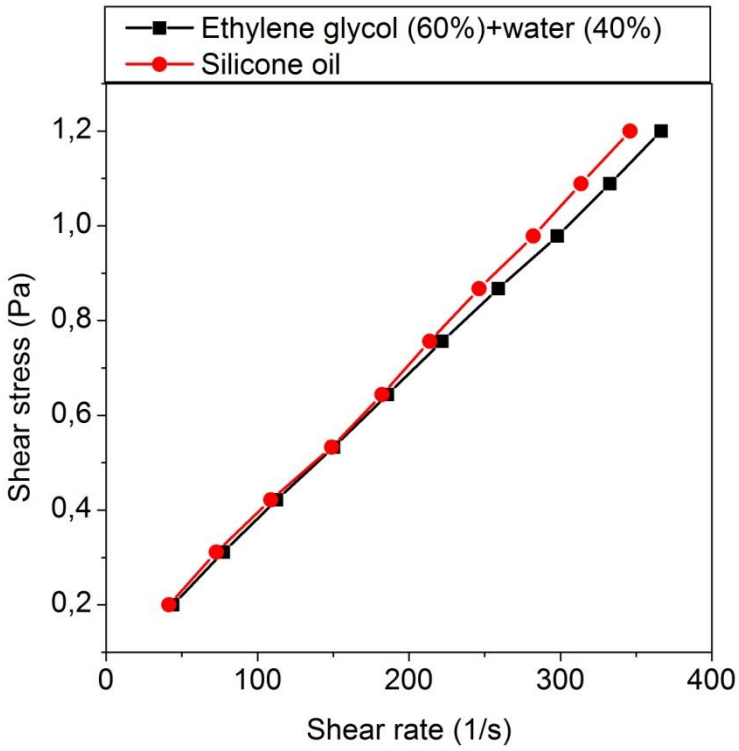

Fig. 3-5 : Rheological property of silicone oil and of the mixture of ethylene glycol (60%) with water

- ***Comparison theory-experiment***

We consider here only the remanent magnetization for the magnetic torque, because, as seen in Fig. 3-6, after the application of a large magnetic field (250kA/m), the fiber keeps a practically constant remanent magnetization, M_r= 145kA/m at small field amplitude, so from Eqs(3.1), (3.4) and (3.22):

$$\frac{d^2\theta}{dt^2} = -\frac{\alpha}{I}\frac{d\theta}{dt} - \frac{\beta_r}{I}\cos(\omega t)\sin\theta \qquad (3.24)$$

$$\omega = 2\pi f$$

The hydrodynamic torque entering in α is given by the equation of Bachelor for a cylinder (26).

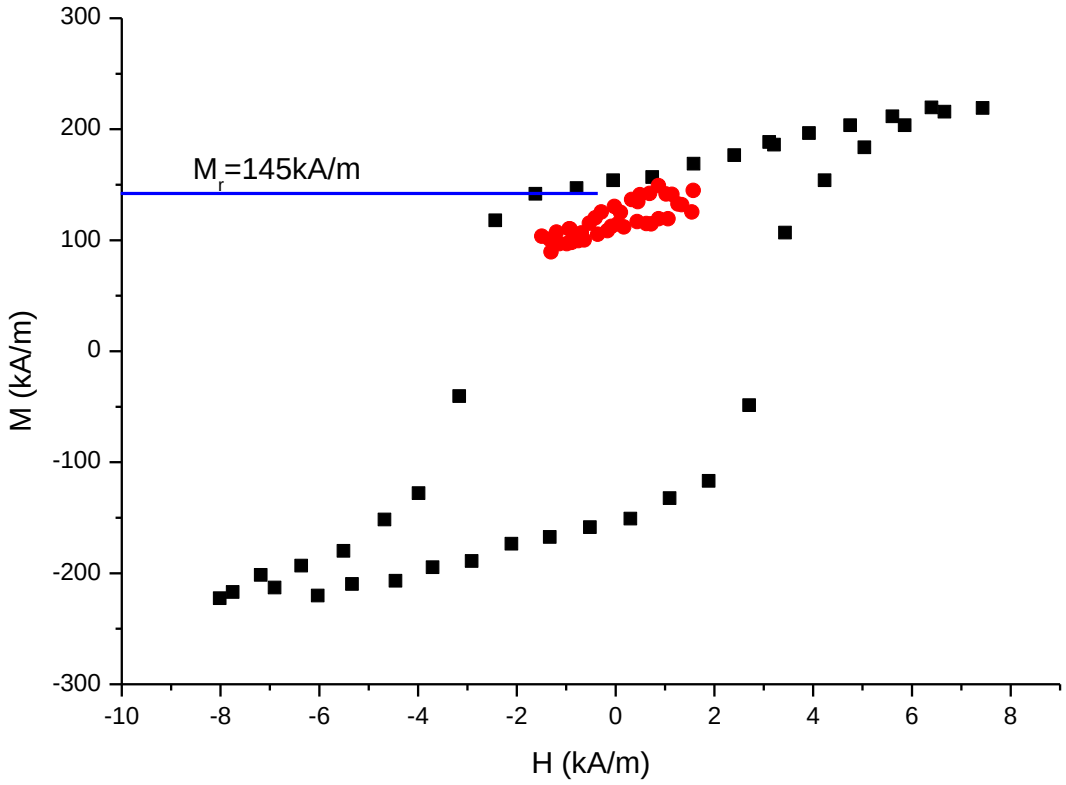

Fig. 3-6. Magnetization curve M= f (H), for a pure nickel fiber, the red dots represent the magnetization cycle at low field amplitude after the magnetization at high field

The equation of motion is solved numerically and the resulting angular motion of the needle is compared with the experimental result in Fig. 3-7. We can see that we have a good agreement-there is no fitting parameter- and in particular that the model well recovers the fact that the fiber remains aligned on the direction of the field the major part of the period. Still it is worth recalling that the applied field is sinusoidal and not squared shape.

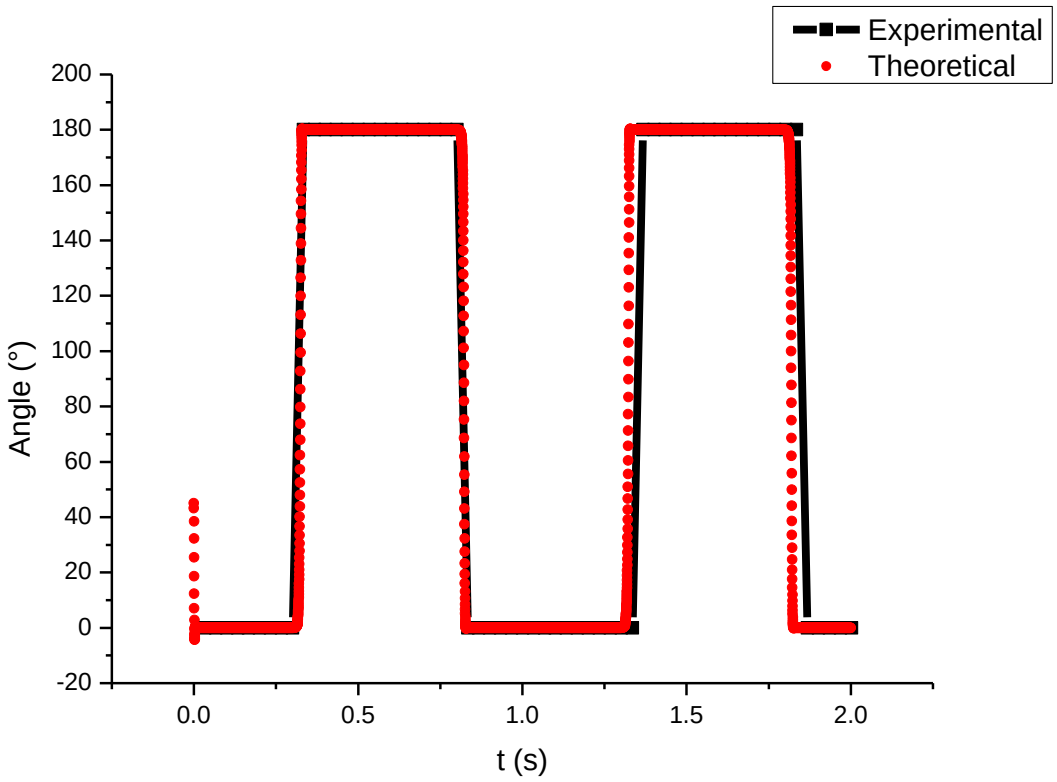

Fig. 3-7. Comparison of experimental and theoretical angular rotation, for f=1Hz, H=31G

- ***Domain of rotation***

We wish to determine the domain of frequencies and field amplitudes for which we obtain a steady angular motion. For this aim we normalize the equation of motion in order to reduce the number of parameters.

First of all, we define a relaxation time of the angular velocity related to the inertia:

$$\tau_I = \frac{I}{\alpha} \tag{3.25}$$

And a rotational time related to the viscosity and the magnetic torque:

$$\tau_R = \frac{\alpha}{\beta} = \frac{4C}{3\mu_0}\frac{\eta a^2}{M_r H} \tag{3.26}$$

We can notice that τ_R does not depend on the volume of the particle but on the square of the aspect ratio. Then, we normalize the time by τ_R and the frequency of the magnetic field by the resonance frequency of the system:

$$t^* = \frac{t}{\tau_R} \tag{3.27}$$

$$f^* = f\sqrt{\tau_R \tau_I} = f\sqrt{\frac{I}{\beta}} \tag{3.28}$$

Using these dimensionless quantities the Eq.(3.24) becomes:

$$\frac{d^2\theta}{dt^{*2}} = -\frac{\tau_R}{\tau_I}\left[\frac{d\theta}{dt^*} - \cos\left(2\pi f^* \sqrt{\frac{\tau_R}{\tau_I}} t^*\right)\sin\theta\right] \tag{3.29}$$

And finally, putting:

$$\gamma = \frac{\tau_R}{\tau_I} = \frac{\alpha^2}{\beta I} \tag{3.30}$$

We obtain:

$$\frac{d^2\theta}{dt^{*2}} = -\gamma\left[\frac{d\theta}{dt^*} - \cos\left(2\pi f^* \sqrt{\gamma} t^*\right)\sin\theta\right] \tag{3.31}$$

We are left with two parameters γ and f^*,

We can then solve numerically this equation for different couples of γ and f^*, and find the domain where the fiber oscillates. If we reassemble all the value of γ and f^* which correspond to an oscillation of the fiber, we can draw the boundary between the two domains. Since this zone is established after the normalization of Eq.(3.24), it can be applied in a general way, no matter the size and the material of fiber, the magnetic field and the applied frequency, or even the viscosity of the fluid. We can verify experimentally if the fiber reaches a state of steady oscillation or stops to move and compare with the theoretical prediction. The experiment has been done with the nickel fiber of diameter 10 μm and 100 microns in length immersed at the interface described in Fig. 3-4 . As Fig. 3-8 shows, the experimental points (blue squares

where there is no oscillation and red dot when it oscillates) coincide with the theoretical prediction of the boundary (black line).

From Eqs. (3.30) and (3.23), we can see that γ is inversely proportional to the magnetic field, on the other hand, from (3.28) and (3.30) it can be expressed as: $\gamma = \frac{\alpha^2 f^{*2}}{I^2 f^2}$, which gives ,for a given frequency *f*, a straight line with a slope of 2 in the log-log presentation of Fig. 3-8,

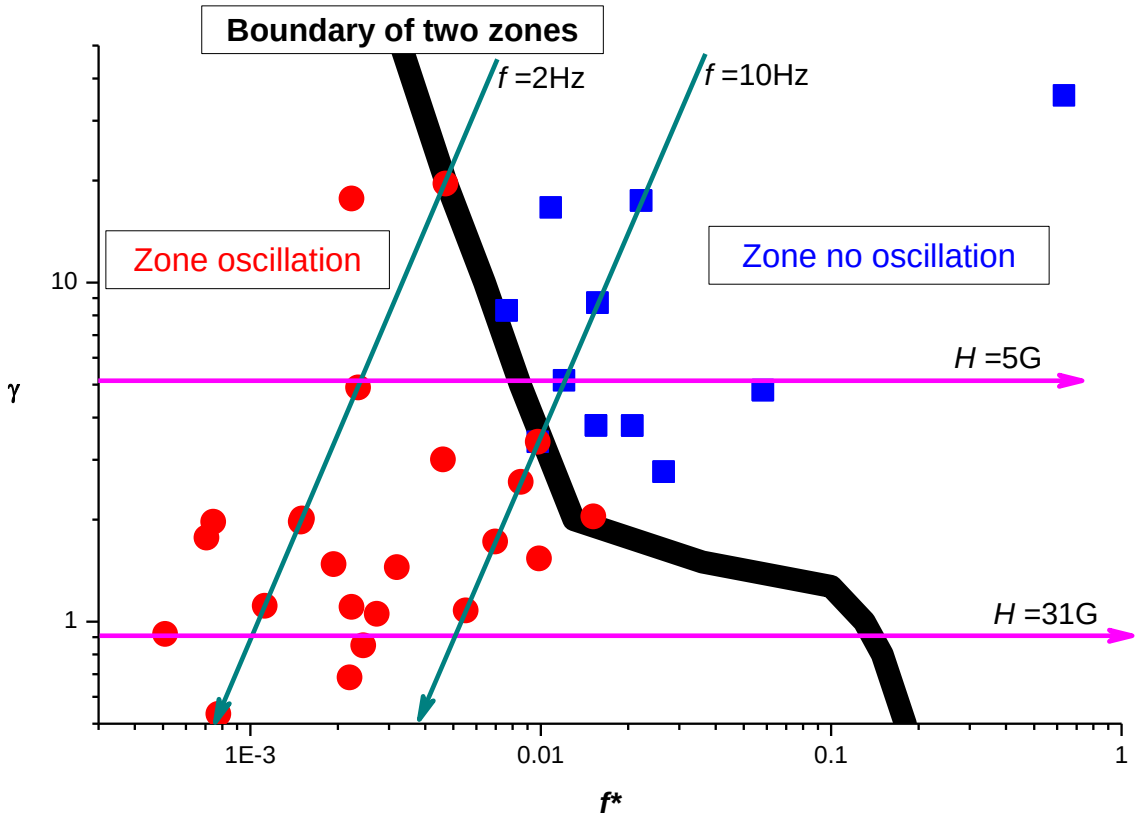

Fig. 3-8. Oscillation zone in the plane, γ, normalized frequency f*

We can see on this graph that, the rotation of the needle in the alternative field happens in zones of high field and low frequencies. Actually the parameter γ in our case is close to unity, which means that the inertia time is similar to the viscous time. This is true because our fiber has a quasi macroscopic length (0.1 mm) but for micro or nanoparticles the inertial time will be much lower than the viscous time so (3.29) becomes:

$$\frac{d\theta}{dt^*} = \cos(\omega^* t^*)\sin(\theta) \qquad (3.32)$$

Recognizing that:

$$\int \frac{d\theta}{\sin(\theta)} = Log(tg(\theta/2))$$

The solution of (3.32) is then given by:

$$\theta(t) = 2\, arctg\left[tg(\frac{\theta_0}{2})\, e^{-\frac{1}{\omega.\tau_R}\sin(\omega.t)} \right] \qquad (3.33)$$

If $\omega\tau_R >> 1$ the oscillation will be small around the initial orientation θ_0, on the contrary if $\omega\tau_R << 1$ then the exponential is either very large or very small depending on the sign of the field and the angle will flip suddenly from 0 to π as shown in Fig. 3-7 . The angular motion is responsible for viscous dissipation and we shall come back to this point in chapter 7. A last remark is that the boundary between the two regimes given by $\omega\tau_R=1$ can be written $\gamma \propto 1/f^{*2}$,

using $\omega\tau_R = 2\pi \frac{f^*}{\sqrt{\tau_R.\tau_I}} \tau_R = 2\pi f^* \sqrt{\gamma}$

It corresponds to the straight line separating the two zones at high values of γ in Fig. 3-8.

3.1.3. Translation of a probe in magnetic field gradient

We have also studied the translation of a magnetic fiber in a viscous liquid, using the same experimental setup than for rotation's experiment (cf. Fig. 3-4); the dish containing two immiscible Newtonian fluids presenting the same viscosity and the magnetic particle floating between the two fluids. But the difference is that we need a field gradient to observe a translational motion; so in this case the sample is placed outside the coils instead of being at the middle of the two coils (cf. Fig. 3-9) to get a magnetic field gradient. On the other hand, in a steady state of motion, we can neglect the inertia so the magnetic force equilibrates the viscous force (drag force):

$$F_m = F_v \qquad (3.34)$$

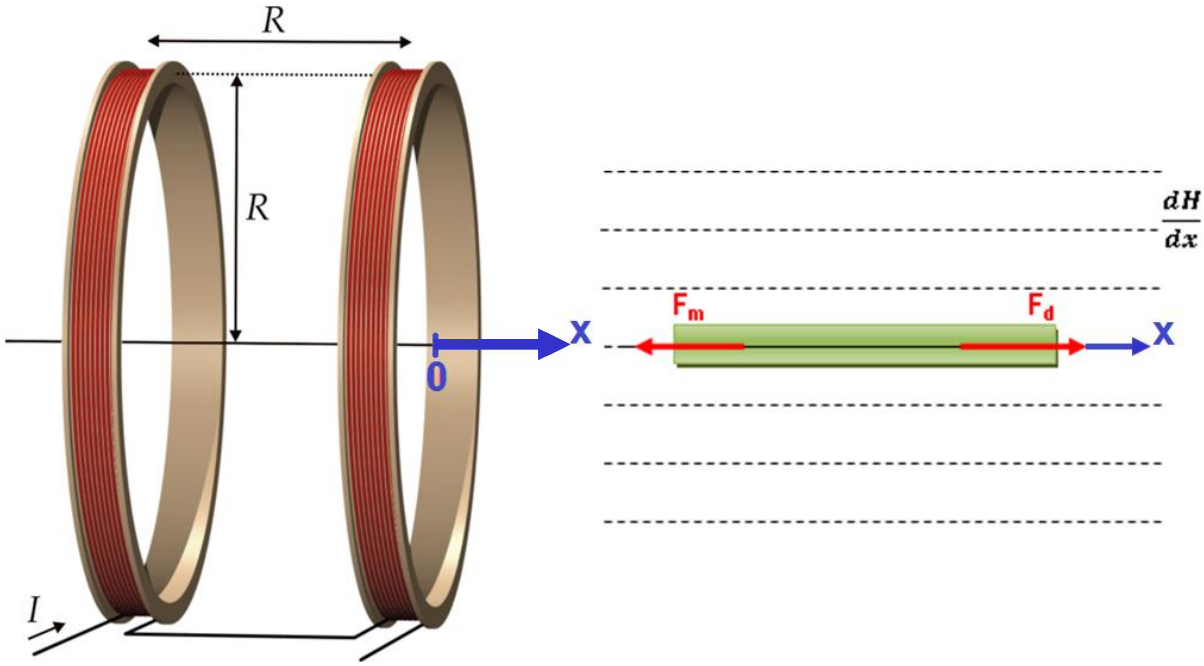

Fig. 3-9. Simplified experiment setup for translation (left), one fiber in a viscous fluid under a magnetic field gradient (right)

The drag force can be written as:

$$F_d = C\frac{dx}{dt} \tag{3.35}$$

Where, C is the coefficient of the drag force, which can be calculated by two methods, one given by Batchelor(26) in the frame of slender body theory:

$$C_1(\varepsilon) = 8\pi\eta l\varepsilon \tag{3.36}$$

With $\varepsilon = \dfrac{1}{\ln\left(\dfrac{2l}{R}\right)}$

And the other by Van de Ven(27) for an elongated ellipsoid:

$$C_2(\varepsilon) = 2\pi\eta\Delta L\varepsilon \tag{3.37}$$

With $\Delta L = \int_{-l}^{l} \frac{1-\varepsilon \log\left(1-\frac{x^2}{l^2}\right)}{1-0.5\varepsilon} dx$;

For our probe the two values are very close but for a cylindrical shape the Batchelor "s result is likely more appropriated.

The magnetic force is given by(30):

$$F_m = \mathrm{m}\frac{dH}{dx} \tag{3.38}$$

Where **m** is the magnetic moment of the needle given by Eq.(3.11) , As we have seen in the preceding section the magnetization is the remanent magnetization, M_r, so:

$$F_m = \mu_0 V M_r \frac{dH}{dx} \tag{3.39}$$

Equating the magnetic force and the drag force gives:

$$F_m = F_d \Rightarrow \mu_0 M_r V \frac{dH}{dx} = 8\pi\eta l\varepsilon \frac{dx}{dt} \tag{3.40}$$

The velocity of fiber in the liquid is then given by:

$$\upsilon_{th} = \frac{dx}{dt} = \frac{\mu_0 M_r V}{8\pi\eta l\varepsilon}\frac{dH}{dx} \tag{3.41}$$

The field gradient *dH/dx* was obtained from the measurement of the magnetic field in several known distances, as shown in Fig. 3-9. All the quantities entering into the Eq. (3.41) are listed in the table below. On the other hand the displacement of the magnetic fiber versus time was obtained from the recorded video and is reported in Fig. 3-11 together with the straight line deduced from the theoretical value of the velocity. The agreement is really good. This was expected as soon as the field gradient and magnetic moment are correctly measured, but it proves that this method is quite reliable to measure the viscosity on a small scale

μ_0	η	M_r	l	V	ε	dH/dx
Wb/(A.m)	Pa.s	A/m	m	m^3	-	$A/m^{\wedge 2}$
1.26E-06	5.00E-03	1.50E+05	7.00E-04	1.37E-12	0.3	10561

Tab. 3-1: the value of the parameters used to calculate the velocity

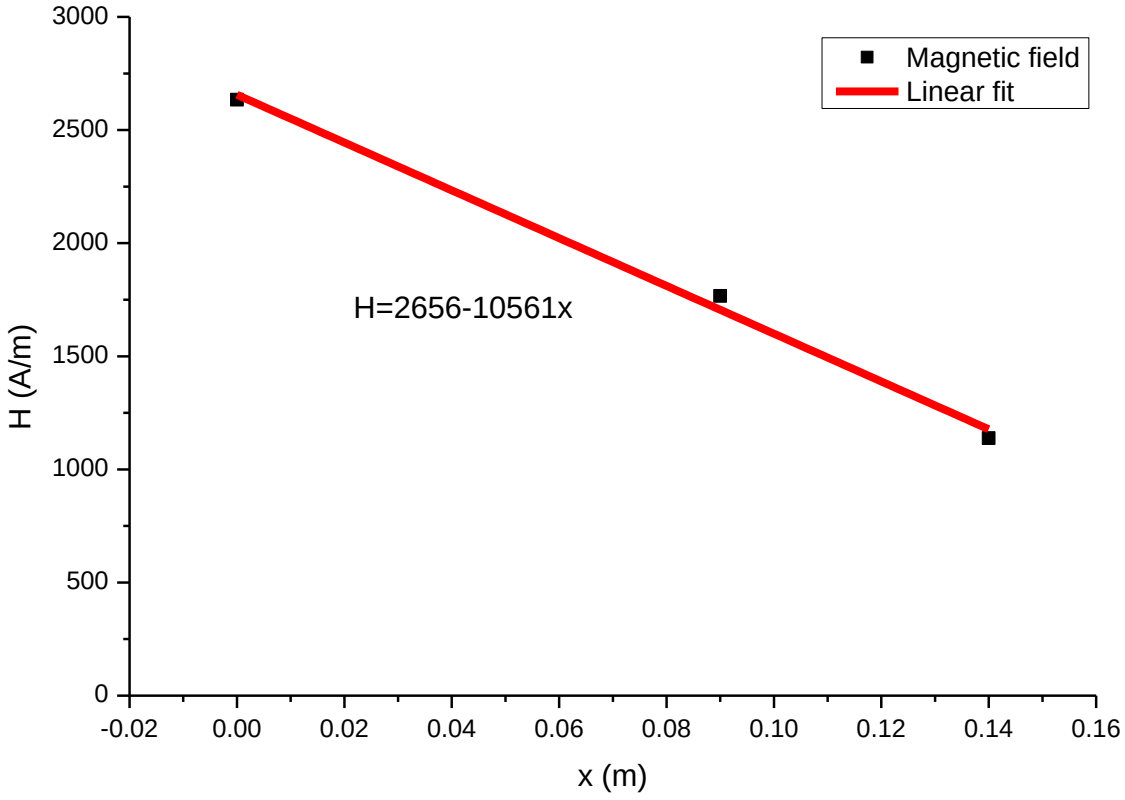

Fig. 3-10 : Measurement of magnetic field gradient

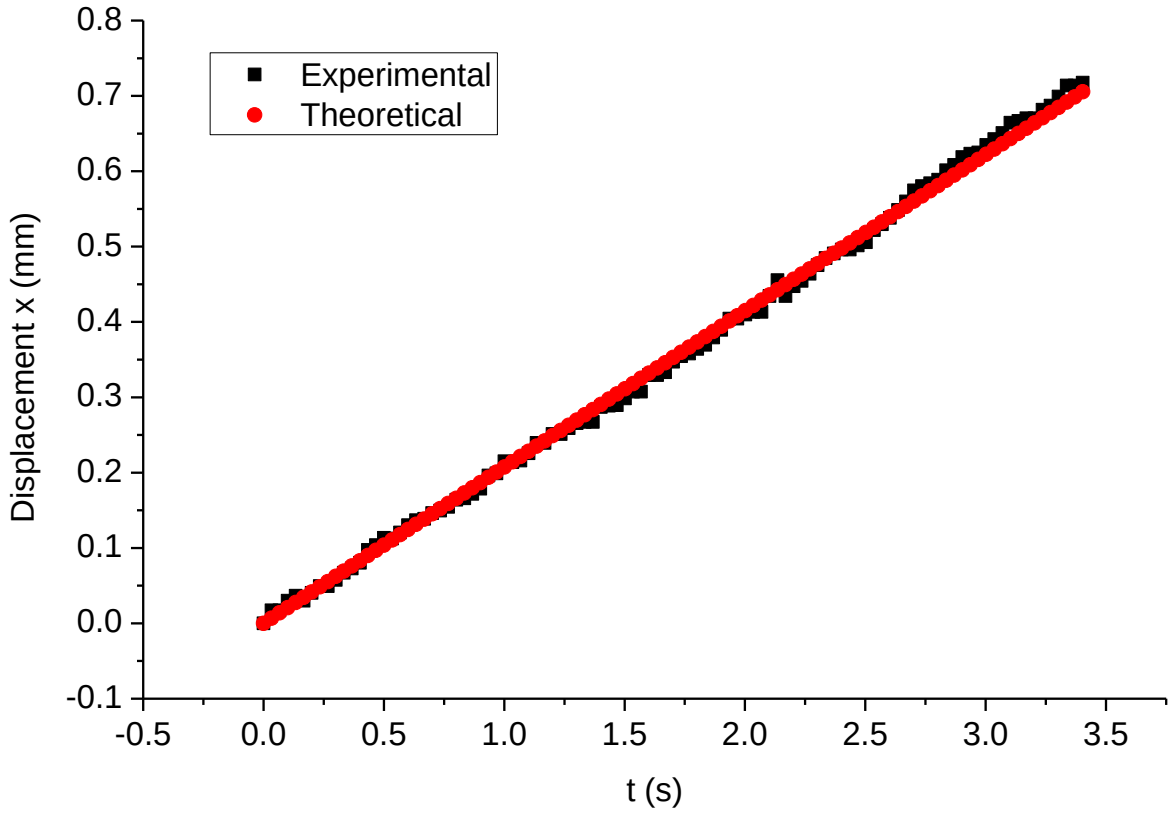

Fig. 3-11 : The translational motion of a magnetic fiber versus time

3.2. Viscoelastic model

Behind the Newtonian fluid, a more realistic model to represent a complex medium like the interior of a cell has to introduce viscoelasticity.

The rheological properties of complex fluids such as suspensions of colloidal particles are not always invariant properties with sample size. Indeed the ratio between the thickness of the layer of fluid studied and the ratio of this thickness to the maximum size of the particles (or aggregates of particles) is a parameter that can intervene critically in the rheology. This is true for electro or magnetorheological fluids where the particles are aligned as strings whose length relative to the size of the cell will determine the appearance of a threshold stress. This also applies to many concentrated suspensions where the lock-release phenomena will depend on the formation of aggregates under shear percolating between the stationary and mobile walls of the rheometers. Also in these environments the classical rheometers is dependent on

many artifacts related to the presence of cell walls (inhomogeneity of concentration on the walls, the effect of wall roughness of slip etc ...). In other situations (lipid bilayers, cell tissues, adsorbed polymer layer on a solid surface etc ...) the local rheological properties are not accessible by conventional rheological methods(31). For these reasons, many studies are related to the use of microprobes that will help measure the rheology at scales much smaller than those of conventional rheometers.

Our work fits into this framework with the aim of determining the viscoelastic properties of the cells using magnetic microprobes, which are set in motion by applying a field or a magnetic field gradient. Besides measuring the viscoelastic properties of the cell, these microprobes can, under certain conditions of application of the field, help to create a pore in the membrane and to allow exchanges between extracellular and intracellular medium, or even to destroy the cell. The characteristic size of a cell is of the order of tens of microns and it is difficult with conventional rheometers to obtain reliable measurements on a monolayer of this thickness. Besides the difficulty of adhering cells on the fixed part and the moving part of the plates, low modulus of elasticity (tens to hundreds of Pascal) requires the use of large areas incompatible with a constancy of the gap that must be greater than one micron. Also the atmosphere must be controlled to 5% CO2 and sterile, which further complicates the experimental conditions. For these reasons the use of probes in the form of rods, plates or spheres resting on the surface of the cell(32) or even inside the cell is clearly preferable to obtain reliable viscoelastic properties.

In order to check the validity of this technique, we have used a viscoelastic gel, named Carbopol, whose rheological characteristics can be measured by conventional rheometers in order to compare these results with those obtained using the particle motion sensors.

The apparatus is the one shown in Fig. 3-1; it consists essentially of a homemade videomicroscope inverted to record the movement of the probes and a coil system for applying a constant magnetic field gradient or an alternating one.

A simple rheological model can then be used to find the fundamental properties such as yield stress Young's modulus and viscosity.

3.2.1. Materials and experimental setup

- ***Viscoelastic medium - Carbopol 980***

Carbopol®980 polymers is a cross-linked polyacrylate polymer, it is proven to be an exceptional thickener, suspending agent and stabilizer, utilized in a wide variety of personal care products. Used at concentrations lower than 1%, it can offer the flexibility to develop products with a wide range of flow and rheological properties.

We mixed 0.2 g of Carbopol powder with 100ml of pure water, and then we added a few drops of triethanolamine, to adjust the pH of the solution. When the pH was equal to about 5, the solution gelled.

- ***Microprobes***

We used several types of probes: an iron ball of 2 mm in diameter, a nickel wire of diameter 250µm, 2.5mm in length, and a cobalt plate of 125µm in thickness, 1 mm in width and 3mm in length.

The iron ball was immersed in the Carbopol. The nickel fiber was placed in the center of a glass tube of internal diameter of 1mm, containing Carbopol.

For a higher contact area with Carbopol, we glued the plate of cobalt on a square glass slide. The slide is on the surface of the gel Carbopol, whose thickness was 1mm.

- ***Experimental setup***

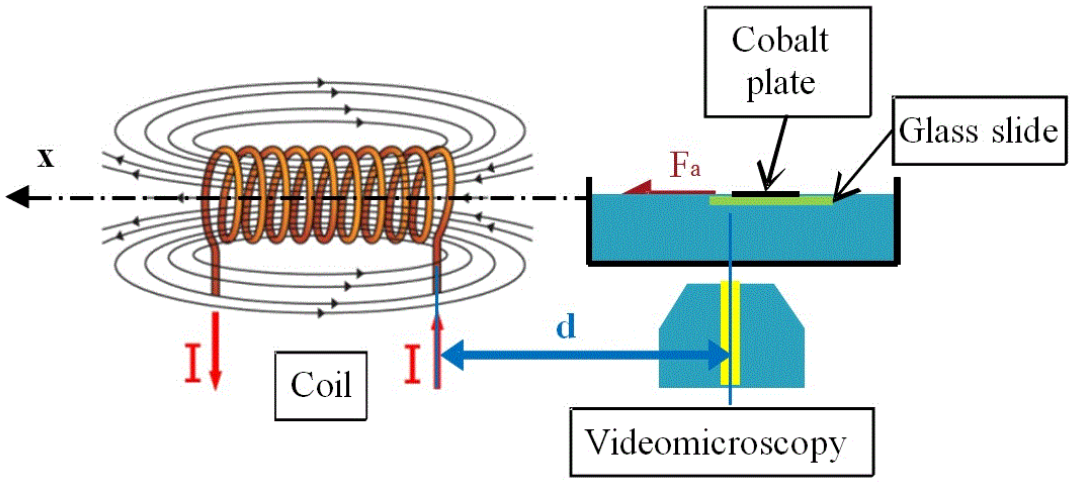

Fig. 3-12: Simplified experimental setup, experience with the cobalt plate bonded to glass slide, on carbopol

The experimental setup consists of an inverted microscope connected to a high speed camera (900ftp). The distance between the center of the objective and the iron core of the coil is about 2 cm. The coil generates the magnetic field, DC or AC.

We studied the motion of each microprobe the recorded images were processed using the free software ImageJ.

3.2.2. Results obtained by conventional rheometry

We first measured the rheological properties of carbopol with a conventional rheometer (Anton Paar Physica MCR 301). Viscosity and yield stress were obtained from a classical strain versus shear rate curve shown in Fig. 3-13, The extrapolation at low shear rates with a Bibgham law gives a yield stress τ_B=70 Pa, and a fit at low shear rate with the Bingham model (see section 2.2.4) gives τ_B=70 Pa and η=16.7 Pa.s . On the other hand the whole curve can be fitted with a model of Herschel-Buckley(33) which generalizes the Bingham model by taking a power exponent n instead of unity:

$$\tau = \tau_0 + K\dot{\gamma}^n \qquad (3.42)$$

The parameters of the fit are the following: K=20.3 and n=0.4.

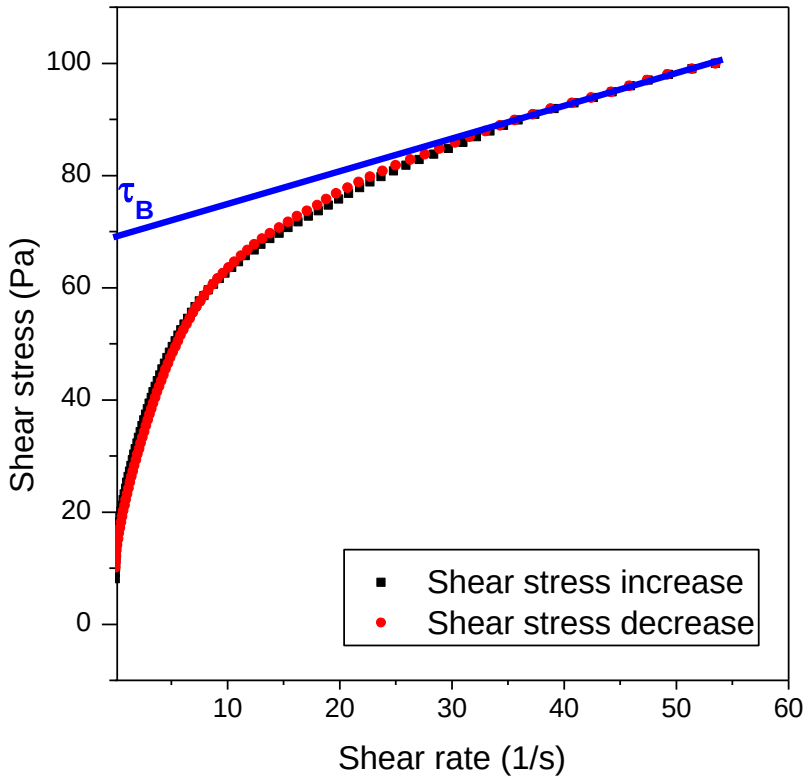

Fig. 3-13: Shear stress/shear rate of carbopol, measured by rotational rheometry; the blue line is a Bingham fit of the decreasing stress with τ_B=70Pa and η=16.7 Pa

On the other hand, we measured the shear modulus at a strain of 0.06% and for frequencies between 3 to 100 rad/s. the storage modulus *G'* increases slightly in this domain from 230 *Pa* to 260 *Pa*, as shown in Fig. 3-14. The loss modulus (right axis of Fig. 3-14) is much lower than the storage modulus, as expected for a viscoelastic solid.

In the following section we are going to use microprobes instead of conventional rheometer, to measure the storage modulus, the viscosity and the yield stress. The final comparison will be presented in section 3.2.4

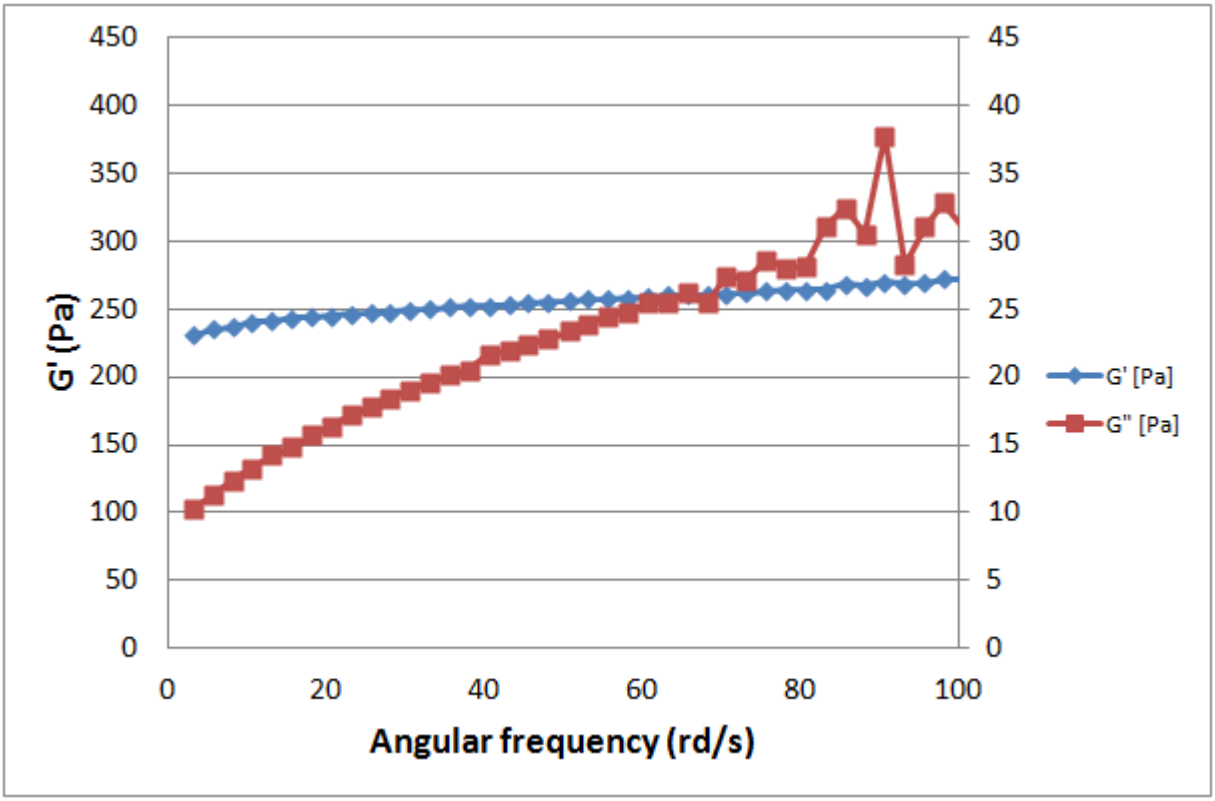

Fig. 3-14: Storage modulus G' and loss modulus G" of carbopol

3.2.3. Use of a microprobe to obtain the rheological properties

Compared to a Newtonian fluid, we have to add the elastic response of the fluid, so the equation of motion should be rewritten as:

$$m\frac{d^2x}{dt^2} = F_m - F_v - F_e \tag{3.43}$$

In this equation, we do not consider the yield of the material, meaning that the applied stress is smaller than the yield stress. For a Kelvin-Voight model (See section 2.2.3) we shall have:

$$m\frac{d^2x}{dt^2} = F_m - C\left(\eta\frac{dx}{dt} - Gx\right) \tag{3.44}$$

Where C is the coefficient of viscous and elastic forces, which depends on the shape of the probe. F_m is the magnetic force, η is the viscosity, G is the shear modulus of material. We

should find the same rheological properties no matter is the kind of probe we use. That is what we are going to test in the following sections.

- ***Microprobe1: Iron ball in an alternating field gradient***

An iron ball with radius of 1 mm was immersed in Carbopol, and we applied an alternating field with a known distance between the ball and the extremity of the iron core inserted in the coil. An alternating current was applied in the coil with a frequency between 2 and 10Hz.

The magnetic force F_m generated on the ball is given by Eq.(3.38), the viscous force, calculated by Eq.(3.35) , the coefficient of the drag force for a sphere is the one of the Stokes law:

$$C = 6\pi R \tag{3.45}$$

And finally, we shall have the following equation Eq. (3.46):

$$m\frac{d^2x}{dt^2} = \mu_0 VM\frac{dH}{dx} - 6\pi\eta R\frac{dx}{dt} - 6\pi GRx \tag{3.46}$$

Where V is the volume of the ball and μ_0 is the vacuum permeability. As seen in section 3.1.3(page 34), the magnetic field in function of the distance was measured in order to obtain the field gradient. Here M is the magnetization of the ball; we have:

$$M = \chi H_i = \chi\left(H_e - H_d\right) \tag{3.47}$$

H_e is the external magnetic field and H_d is the demagnetizing field, for a sphere, it is given by:

$$H_d = \frac{1}{3}M \tag{3.48}$$

So from Eq.(3.47) and Eq.(3.48), we have:

$$M = \chi\left(H_0 - \frac{1}{3}M\right) \tag{3.49}$$

Or

$$M = \frac{3\chi}{3+\chi} H_{ext} \tag{3.50}$$

Since we applied an alternative field,

$$H_{ext} = H_0 \cos(\omega t) \tag{3.51}$$

$$\frac{dH}{dx} = \frac{dH_{ext}}{dx} = \frac{dH_0}{dx} \cos(\omega t) \tag{3.52}$$

Then the magnetic force becomes:

$$F_m = \mu_0 V \frac{\chi}{1+\chi/3} \frac{dH_0}{dx} H_0 \cos^2(\omega t) = \mu_0 V \frac{\chi}{1+\chi/3} \frac{dH_0}{dx} H_0 \frac{1+\cos(2\omega t)}{2} \tag{3.53}$$

In practice $\frac{\chi}{1+\chi/3} \simeq 3$, when $\chi \gg 1$ which i s the case for our probe.

So Eq.(3.46) should be written as:

$$m\frac{d^2x}{dt^2} + 6\pi\eta R\frac{dx}{dt} + 6\pi GRx = \frac{3}{2}\mu_0 V \frac{dH_0}{dx} H_0 \left[1+\cos(2\omega t)\right] \tag{3.54}$$

Or, simplified as:

$$m\frac{d^2x}{dt^2} + C\left(\eta\frac{dx}{dt} + Gx\right) = F_0\left[1+\cos(2\omega t)\right] \tag{3.55}$$

With $F_0 = \frac{3}{2}\mu_0 V \frac{dH_0}{dx} H_0$

This is a classic inhomogeneous second-order linear ordinary differential equation; the resolution of this equation is composed of two parts $x_{ts}(t)$ the transient solution and $x_{ss}(t)$ the steady-state solution:

$$x(t) = x_{ts}(t) + x_{ss}(t) \tag{3.56}$$

$$x_{ts}(t) = \frac{F_0}{CG} + \mathrm{e}^{-\frac{(C\eta+\sqrt{C^2\eta^2-4CGm})}{2m}t}(C_{[1]} + \mathrm{e}^{\frac{\sqrt{C^2\eta^2-4CGm}}{m}t} C_{[2]}) \tag{3.57}$$

$$x_{ss}(t)=\frac{F_0\left[(CG-4m\omega^2)\cos(2\omega t)+2C\eta\omega\sin(2\omega t)\right]}{C^2G^2+4C(C\eta^2-2Gm)\omega^2+16m^2\omega^4} \tag{3.58}$$

Looking at the experimental results (cf Fig. 3-15) we notice that the experimental result is not just a regular combination of cosine and sine function of period 2/ν but that we have also a component at the frequency of the applied field. The explanation is that the magnetic force has a second part, due to the remanent magnetization of iron ball. So Eq.(3.38) should be rewritten as:

$$F_m=\mu_0 V(M+M_r)\frac{dH}{dx}=\frac{3}{2}\mu_0 V\frac{dH_0}{dx}H_0\left[1+\cos(2\omega t)\right]+\mu_0 V\frac{dH_0}{dx}M_r\cos(\omega t) \tag{3.59}$$

Or as:

$$F_m=F_0\left[1+\cos(2\omega t)\right]+F_1\cos(\omega t) \tag{3.60}$$

With $F_0=\frac{3}{2}\mu_0 V\frac{dH_0}{dx}H_0$ and $F_1=\mu_0 V\frac{dH_0}{dx}M_r$

In this case, theequation of motion:

$$m\frac{d^2x}{dt^2}+C\left(\eta\frac{dx}{dt}+Gx\right)=F_0\left[1+\cos(2\omega t)\right]+F_1\cos(\omega t) \tag{3.61}$$

The steady-state solution of this equation is:

$$x(t)=x_0(t)+x_1(t) \tag{3.62}$$

With:

$$x_0(t)=F_0\frac{\left(CG-4m\omega^2\right)\cos(2\omega t-\phi)+2C\eta\omega\sin(2\omega t-\phi)}{C^2G^2+4\left(C^2\eta^2-2CGm\right)\omega^2+16m^2\omega^4} \tag{3.63}$$

$$x_1(t)=F_1\frac{\left(CG-4m\omega^2\right)\cos(\omega t-\phi)+C\eta\omega\sin(\omega t-\phi)}{C^2G^2+\left(C^2\eta^2-2CGm\right)\omega^2+m^2\omega^4} \tag{3.64}$$

And the phase ϕ depends on the initial condition.

With fitting resolution, we can get the two unknowns η and G. The magnetic field and the magnetic field gradient have been measured and we are left with three parameters: The remanent magnetization, the viscosity η and the shear modulus G. The first curve at f=3Hz and H=42kA/m was fitted with these three parameters and we obtained M_r=5kA/m. The two other curves were fitted with two parameters, keeping M_r =5kA/m.

In Fig. 3-15 we have presented the experimental motion of the ball and the result of the fit by Eq.(3.62) for different conditions: f=3Hz or 10Hz, H=23kA/m or 42kA/m, In these three cases we obtained $G = 270\text{Pa}$ and $\eta = 270 * 0.1 = 27 Pa.s$.

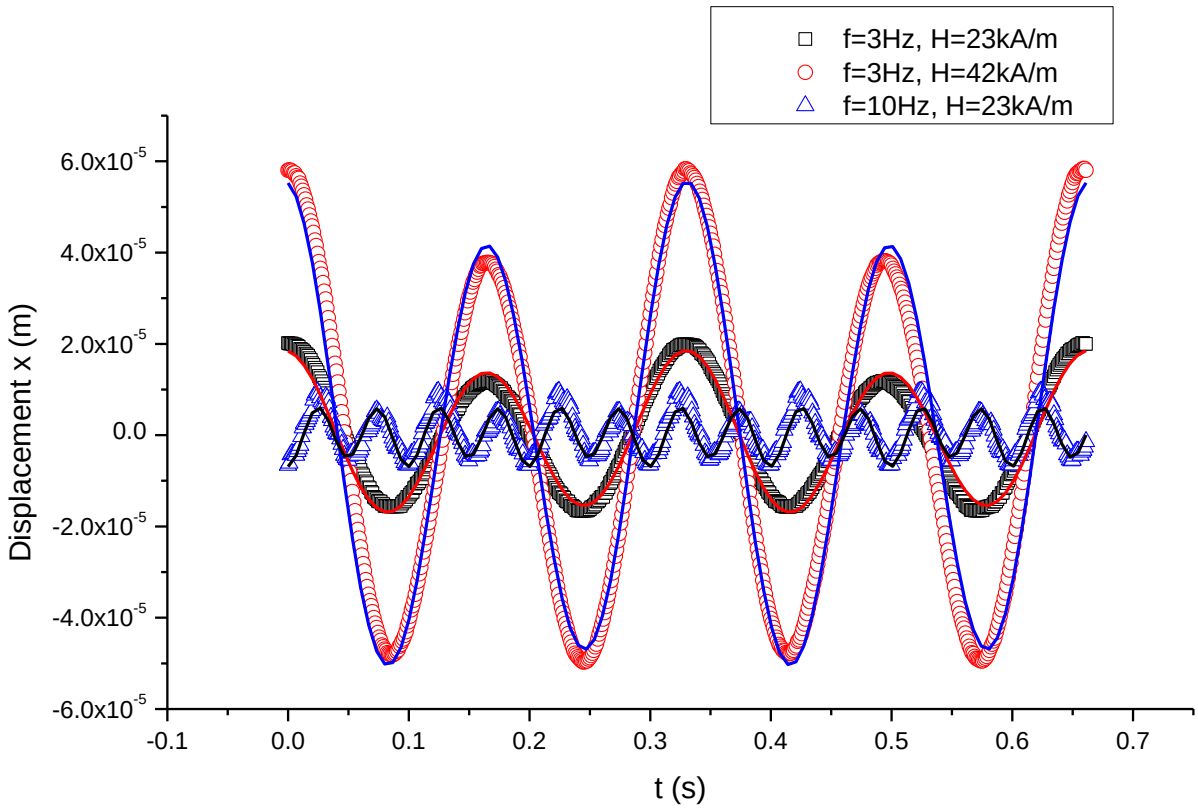

Fig. 3-15: Displacement of the iron ball vs. time, and fitting curve, for different frequencies and field

- ***Microprobe 2: Cobalt plate-plate system***

This time, we used as microprobe a rectangular cobalt plate of dimension, 1mm*3mm and thickness 0.125mm, the deepness of carbopol was h=1 mm. In order to increase the surface of contact with carbopol and also to prevent its sinking, the cobalt plate was glued on a round

glass slide of diameter 13mm and contact surface S=133 mm^2. The objective of the microscope is always focused on the edge of the slide and the displacement of the probe is not more than a few hundred microns. We impose a constant magnetic field at $t=0$ and turn it off after a few seconds, then we simultaneously record the displacement of the cobalt plate versus time. In this kind of creep experiment the inertia force is negligible so we can write:

$$F_m = \left(\eta \frac{\dot{x}}{h} + G\frac{x}{h}\right) S \qquad (3.65)$$

In this case the factor C of Eq. (3.44) is now $C = \frac{S}{h}$, which is equal to 0.133m.

The magnetic force on the plate is more difficult to calculate than on a sphere because it requires a good knowledge of the dependence of the magnetic permeability of the plate as a function of the field (unlike the case of the sphere where the dipole moment does not depend on the permeability when it is large due to the demagnetization field).

We therefore used a direct method for measuring the magnetic force by using a "balance" (Precisa 40SM-200A) which has an accuracy of 0.1 mg. The cobalt plate bonded with the slide was attached at the bottom of the balance as shown in the left part of Fig. 3-16, and the same coil as in the previous experiments was used to apply the magnetic force.

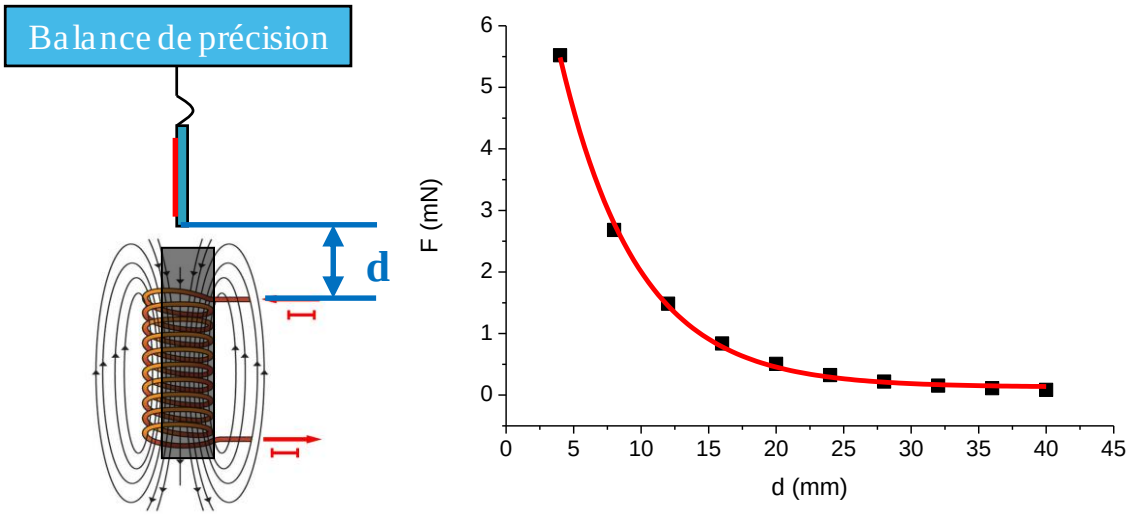

Fig. 3-16: Measurement setup of the magnetic force, here for a thin slice of cobalt; right figure is the magnetic force as a function of the distance(fitted by an Exponentially Decreasing Function)

With this setup, we have determined the magnetic force in function of the distance, as shown in the right part of Fig. 3-16. Since the order of magnitude of the displacement of the microprobe is of several microns to some tens of microns, we can consider that the applied magnetic force is practically constant.

As the rising time (~0.001s) of the applied magnetic force $F_m(t)$ is much smaller than the Maxwell time of carpobol (~0.1s), we can consider that F_m is constant and the displacement after turning on suddenly the field is given by:

$$x(t) = \frac{F_m}{CG}\left(1 - e^{-\frac{Gt}{\eta}}\right) \tag{3.66}$$

We fitted the experimental curves by this equation; the results are shown in Fig. 3-17. With 3 different applied forces, we obtained the shear modulus $G = 163.0Pa$, and the viscosity $\eta = 30.3Pa.s$.

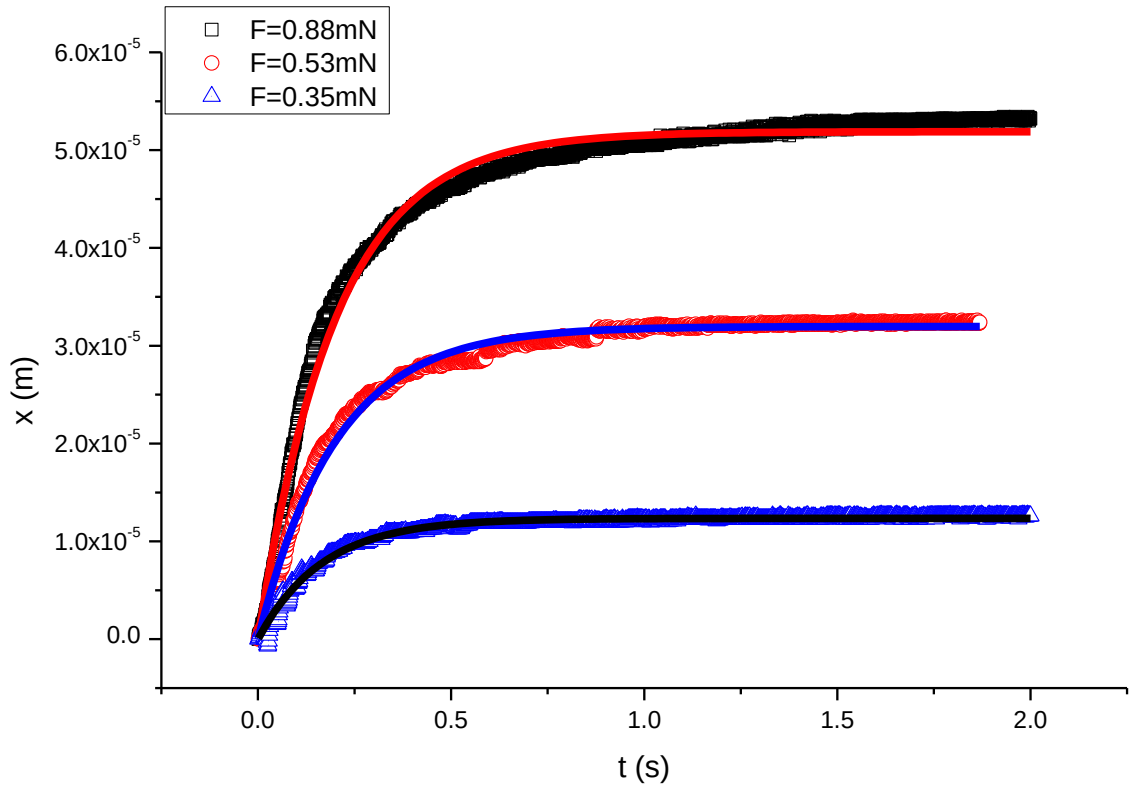

Fig. 3-17: Motion of the cobalt plate vs. time, for three applied step forces: 0.88mN, 0.53mN, 0.35mN

- ***Microprobe 3: Nickel microfiber, coaxial system***

We put a nickel fiber of radius R=125µm and length l=2.5µm in the middle of a glass tube of radius R_i=500 µm containing Carbopol, which is a coaxial structure, shown in Fig. 3-19. Here, too, the inertial force is negligible in our experimental condition. The equation of motion of the fiber is still given by:

$$F_m = \mu_0 M(H) V \frac{dH}{dx} = C\eta \frac{dx}{dt} + CGx \tag{3.67}$$

$$C(\varepsilon) = 4\pi l \left(\frac{2 + 0.307\varepsilon}{2 - \varepsilon} \varepsilon + 0.426\varepsilon^3 \right) \tag{3.68}$$

with for a cylinder(26): $\varepsilon(a) = \frac{1}{\ln(2a)}$ and $a = \frac{2l}{R}$

With $C = 0.0224$ in our case.

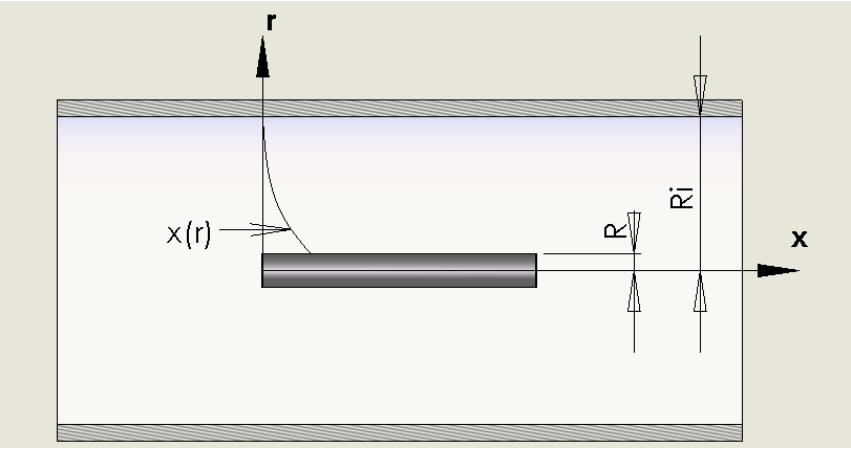

Fig. 3-18: the nickel fiber touring by Carbopol in a glass tube

We are looking to the displacement of the fiber under the sudden application of a constant magnetic field. This setup has the advantage that the motion of the extremity of the fiber is easier to follow than for a sphere.

We can see in.Fig. 3-19 that the difference between the lower curve and the two other ones is that, after 0.2s, the displacement of the probe stopped, whereas for the two upper curves it continues to move, meaning that the applied stress is above the yield stress, $\tau < \tau_B$. The magnetic force F_m is calculated by FEMM.

S is the contact surface:

$$S = 2\pi R * l \tag{3.69}$$

In the case where the applied stress is below the yield stress, $\tau < \tau_0$, as the black square showed in Fig. 3-19, we can deduce the viscosity and shear modulus by fitting this displacement by:

$$x(t) = \frac{F_m}{CG}\left(1 - e^{-\frac{Gt}{\eta}}\right) \tag{3.70}$$

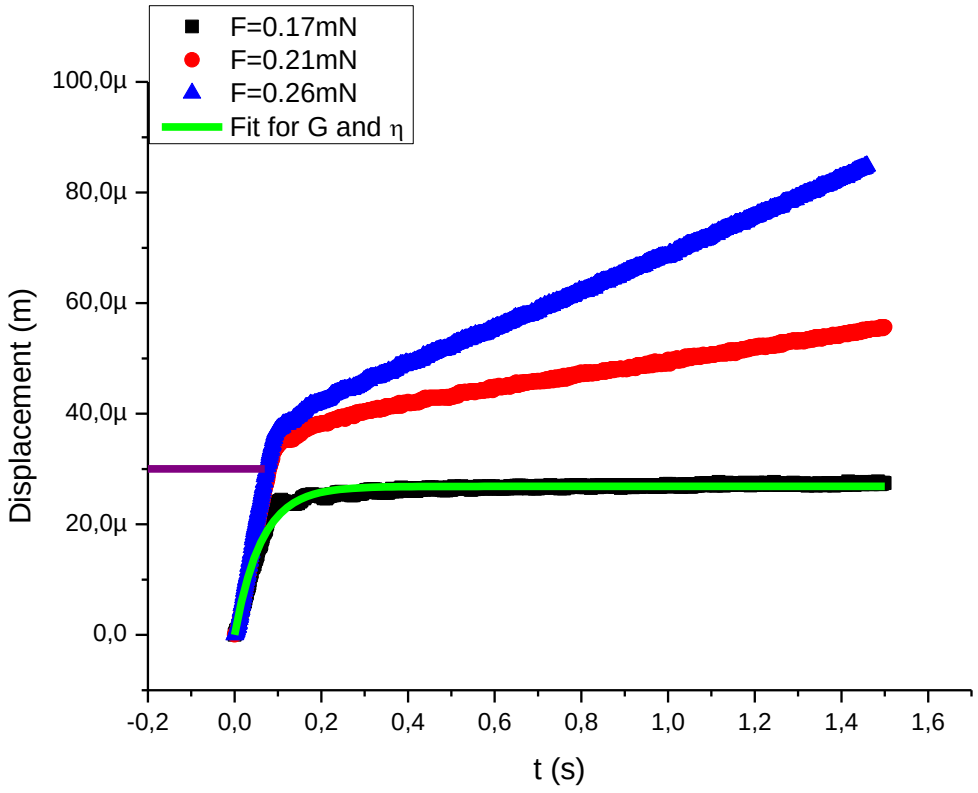

Fig. 3-19: The displacement of the nickel fiber versus time

We obtained $\eta = 17 Pa.s$ and $G = 282 Pa.s$.

The rheological behavior can be described by a Bingham model for $\tau > \tau_B$, Eq.(3.67) becomes:

$$F_m = C\eta \frac{dx}{dt} + S\tau_B \qquad (3.71)$$

The Bingham yield stress obtained from the two upper curves of Fig. 3-19, using Eq.(3.71) are respectively 126 Pa and 103 Pa. We shall keep this last value although the real value should be lower since it corresponds to a plastic velocity which tends to zero.

3.2.4. Summary of the results with Carbopol

In the table below we have summarized the results obtained with the 3 microprobes in carbopol and compared with the ones obtained in conventional rheometry:

	Sphere	Plate	Cylinder	Conventional rheometers
G (Pa)	270	163	282	250
η (Pa.s)	27	30	17	16.7
τ_0 (Pa)	/	/	103	70

Tab. 3-2 Summary of the results obtained with the 3 microprobes and conventional rheometry

It appears that the rheological parameters obtained with these three probes are rather close to the ones measured in conventional rheometry, the closer results being obtained with the cylindrical probe. In any event we do not expect a perfect agreement because this material has not really a linear response: the modulus depends slightly on the amplitude and on the frequency and the viscosity is not really well defined since the Bingham model is valid only in a small range of shear rates.

3.3. Discussion and conclusion

In this chapter, we have first studied the motion of microprobes in rotation and translation in a Newtonian fluid. In our experimental conditions the inertia was not negligible, and we found the range where its presence can hinder the rotation of the fiber. When the

inertia becomes negligible (smaller probe and/or higher viscosity) there are two regimes, one at frequencies smaller than $1/\tau_R$ where the fiber rotates with a rapid "flip-flop" when the field changes of direction and the other at higher frequencies where the fiber only oscillates around its initial position. Since τ_R is proportional to the viscosity and to the square of the aspect ratio (cf Eq.(3.26)), a particle of aspect ratio of 10 with a remanent magnetization of, say $2\ 10^5$ A/m, under a field amplitude of 10kA/m will rotate until frequencies of about 10kHz in water, but only 10Hz if the viscosity is 1Pa.s as can be the case at the surface of a cell. In order to measure the rheological properties at the microscale of a cell, we have explored the behavior of probes –with sizes in the range 100μm-1mm- in a reference viscoelastic solid: the carbopol. The external force being applied by a gradient of magnetic field, the probe can be placed everywhere in the medium to analyze, but we need to be able to follow its motion with a microscope. We have found that several different techniques (oscillating force, step force, sphere, cylinder, plate) were all giving reasonable evaluations of the rheological parameters. The more reliable result was obtained with the application of a step field on a fiber. This technique could be used with cells but the limitation is the optical resolution if we want to use microparticles of sizes well below the size of the cell. Furthermore the particles laying on the surface of the cell, and the force being applied parallel to the surface of the cell, there will be induced torques if the surface of the cell is not flat, which is often the case. Magnetic microprobes can be useful to measure the rheological properties of biological materials if the medium in which they are immersed is homogeneous at a scale well larger than the microprobe, which is not the case for the cells we want to study.

In the following we shall use a more reliable technique, based on AFM measurements to extract the rheological properties of the cells.

4. RHEOLOGICAL PROPERTY OF CANCER CELL BY AFM

4.1. Introduction

The rheological properties of single cells have been investigated in the past using a large variety of methods like micropipette aspiration(34), traction or compression between two microplates(35), optical tweezers(36,37), magnetic twisting cytometry(38,39), rotational microrheology(28), atomic force microscopy (AFM)(40–42) and many other methods. All these methods (except micropipette aspiration) have in common the tracking of a micro or a nanoparticle either at the surface of the cell or even inside the cell in response to an applied force. Then a model is needed to relate the force-displacement curve to the viscoelastic properties of the cell. If the probe is larger than the characteristic mesh size, ξ, of the actin network (typically $\xi=100nm$) a continuum approach can be used to model this response. A possible approach rests on a two fluid description with a viscoelastic network coupled by a frictional force to *a* viscous fluid (32). The approximation of low Reynolds number, which is the ratio of inertial forces to viscous ones, can be written as:

$$\mathrm{Re} = \frac{\omega^2 a l \rho}{G(\omega)} << 1 \qquad (4.1)$$

With *a* is the radius of the probe, *l* is the amplitude of motion of the probe, ρ the density of the fluid and G(ω) the frequency dependent shear modulus.

The order of magnitude of a and l being the micron and the order of magnitude of G(ω) being between 0.1 and 10kPa, it is readily seen that this condition holds even for frequencies as high as 100 kHz. The other condition needed for the use of a frequency generalized Stokes' law is that a compressive wave in the elastic network would be overdamped on a characteristic length equal to the dimension of the probe; this is realized for frequencies above(32,43):

$$\omega_b = \frac{(2\mu + \lambda)}{a^2 \Gamma} \qquad (4.2)$$

Where λ and μ are Lamé coefficients and $\Gamma \sim \eta / \xi^2$ is the friction coefficient between the fluid phase and the elastic network. Introducing $\tau = \eta / G$ with G the static shear modulus, the crossover frequency becomes:

$$\omega_b = \left(\frac{1}{\tau}\right)\left(\frac{\xi}{a}\right)^2 \qquad (4.3)$$

We shall see in the following that the order of magnitude of the relaxation time is the second , so we get $\omega_b \sim 10^{-2}$; it means that the deviation from generalized Stokes' Einstein equation is only expected at very low frequencies, that is to say on a long time scale. In AFM experiments, as well as with optical tweezers the bead is not completely immersed in the viscoelastic medium, so this continuum approach must be modified to take into account different boundary conditions. When the motion of the probe is perpendicular to the surface as in AFM or indentation experiments, the basic relation who can be generalized in the frequency or time domain is no longer the Stokes law, but the Hertz law, which applies to a spherical probe which settles in an elastic medium. Due to the change of the contact surface with time, the time dependent generalization of the Hertz law, which rests on the hypothesis of a linear superposition of delayed response to increments of force or displacement, must be properly written. Such a generalization was described, for instance in the book by Johnson(44) and applied to nanoindentation of cells(45). As the cell thickness is often not very large compared to the indentation depth, a correction of the Hertz formula has been proposed(46) for elastic media which introduces a function of the indentation depth over the cell thickness; this correction was used to model the time dependent response to an approximate step displacement, with the approximation that during the relaxation of the force, the indentation depth could be considered as a constant(47). Besides the time dependent generalization of the Hertz model, including the cell thickness correction, a description of the viscoelastic response function is needed because, due the limited range of time -or frequency- in the experiment, it is more direct to fit the experimental curve with a model response function, G(t) for a stress step, or J(t) for a displacement step than to deduce it from a deconvolution equation. Furthermore the viscoelastic models can give some insight in the physical process underlying their representation. One of the most common models to describe a viscoelastic solid is the Zener model consisting of a Maxwell element in parallel with a spring representing the zero frequency elastic modulus G_0, the Maxwell element introduces a relaxation time:

$$\tau_i = \frac{\eta_i}{G_i} \tag{4.4}$$

This simple model of viscoelastic solid containing three parameters, can describe quite well the mechanical response of different kinds of cells(48,49), nevertheless some other experiments show a more complex response which can be described by a set of relaxation times or by a power law. In this last case an interpretation of the power law behavior was proposed in terms of a distribution of relaxation times associated with a power law for the distribution of the lengths of the elementary units of the actin network which is supposed to present a fractal structure(50). The mechanical response of a cell to different stimuli is important, because several biological functions are regulated by their contact with the neighboring cells or the extracellular matrix(51). On the other hand it has recently been demonstrated that a small mechanical stimulus induced by the periodic motion of magnetic nanoparticles at the surface of the membrane can cause the death of the cell(52,53). Since a magnetic field can easily be applied in vivo it could be an attractive way to destroy tumors if the magnetic nanoparticles specifically bind to the cancer cells. In this paper our objective is to obtain the rheological characterization of a given type of cancer cells in order to use it in a future work to model the motion of different kinds of magnetic nanoparticles deposited on the surface of the cells. An atomic force microscope was used and in a first section we describe briefly the operating conditions and the biological material. As explained above, different approximated methods are used to identify the viscoelastic parameters from the experiments, so the second section will be devoted to a presentation of the equation used to deduce the material properties from the indentation depth versus time of a spherical indenter, and the prediction of this equation will be tested against the trajectory of the bead deduced from a finite element simulation which mimics the operating condition of the AFM. In the third section the results are analyzed through different rheological models and it is shown that the rheological characteristics of the cell depend strongly of the indentation velocity; furthermore their dependence on the temperature is also presented and discussed.

4.2. Materials and methods

Besides imaging, another major application of AFM is force spectroscopy through the direct measurement of tip-sample interaction forces as a function of the indentation depth of the tip

into the sample. Compared to conventional rheometers the use of AFM to get rheological properties raises three problems. The first one is the determination of the position of the probe relatively to the surface, the second one is due to the fact that the contact surface between the probe and the biological material is changing during the experiment and at least we have no independent measurement of the position of the probe and of the applied force. As presented in the introduction there are many papers dealing with these problems and we do not intend to make a review of them here, but just to present what we think to be the best way to overcome them.

4.2.1. Cancer cells

- ***Cell Hep G2***

One of cancer cell which has been studied is called Hep G2, a human liver carcinoma cell line. Hep G2 cells were grown at a BD Falcon™ 35 mm Easy-Grip™ Cell Culture Dish, in Dulbelcco modified Eagle culture medium (Invitrogen, Carlsbad, CA) containing 10% fetal calf serum, glucose (4.5g/L), glutamine (2mM), penicillin (100units/mL), 10 mg/mL gentamycin in a wet (37°C) and 5% CO2/95% air atmosphere.

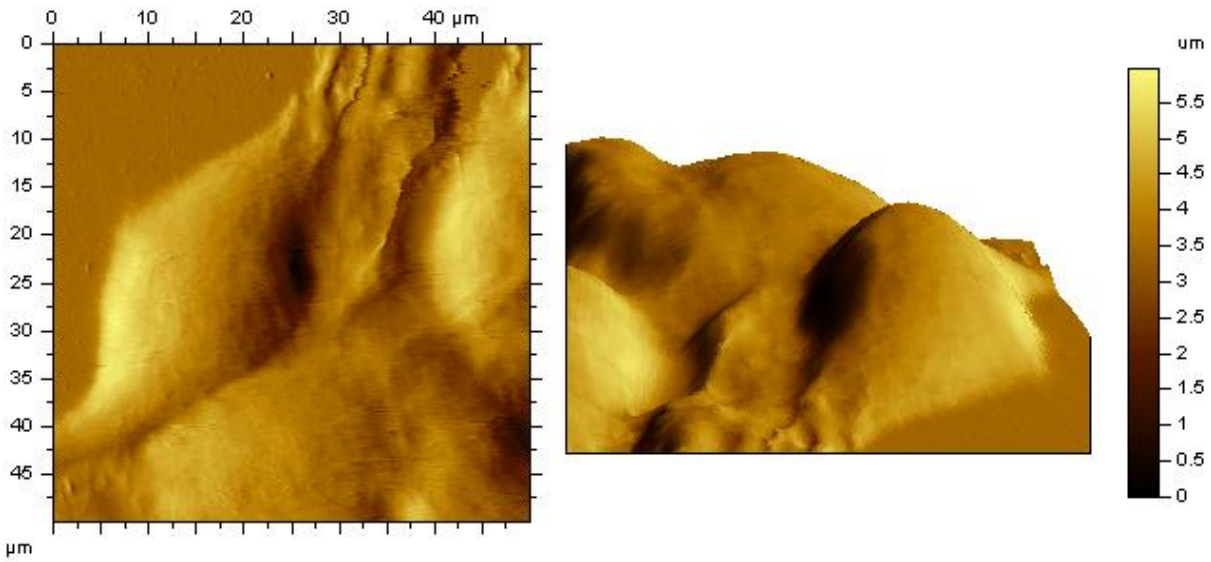

Fig. 4-1: An AFM image of Hep G2

- ***BNL CL.2***

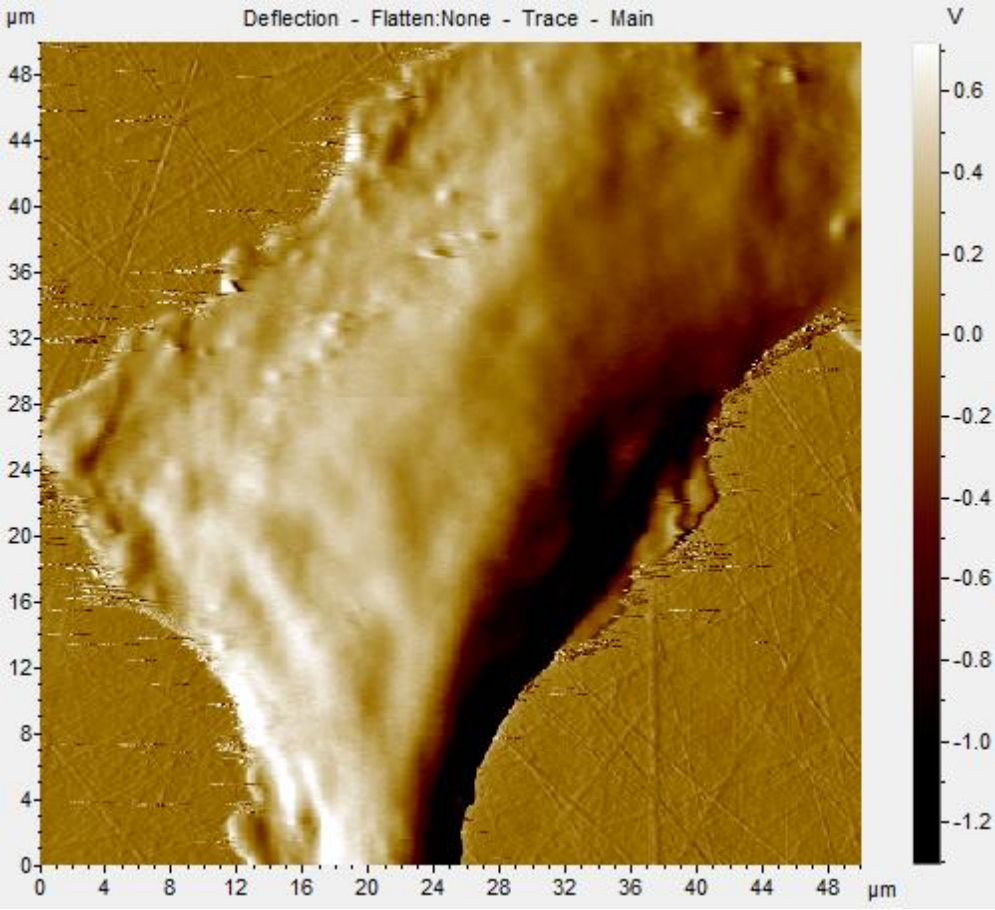

Fig. 4-2: An AFM image of BNL CL.2

The other cell line called BNL CL.2 is a mouse liver embryonic cell. They grow also inside a Petri dish, in the medium of DMEM, with 5% CO2/95% air atmosphere.

For fluorescence microscopy, HepG2 cells were grown on glass cover slips for 48h and fixed with 4% paraformaldehyde for 15 min. Cells were then permeabilized with PBS(Phosphate buffered saline) 0,1% triton. For microtubule staining, cells were incubated with anti beta-tubulin followed by secondary anti mouse antibody coupled to Alexa-488 (Molecular Probe). For actin staining, cells were incubated with phalloidin (Sigma Aldrich). Nuclei were stained with Hoescht. Cover slips were mounted on slides using Permafluor (Thermo Scientific) and observed with Zeiss Axioimager microscope.

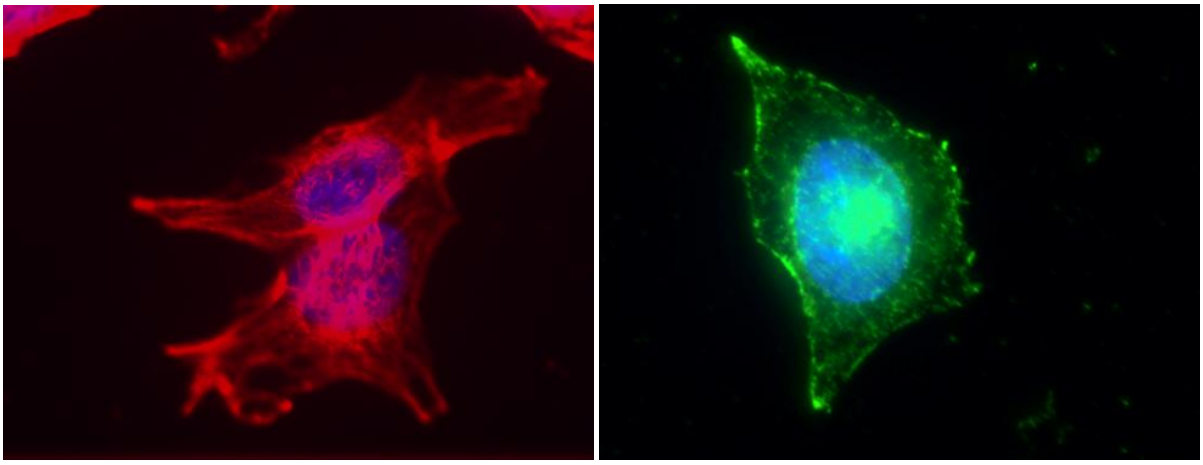

Fig. 4-3: The organization of actin (left) and microtubules (right) of Hep G2 shown by fluorescent microscopy

The organization of actin and microtubules are shown separately, respectively on the left and right hand side of Fig.1. The nucleus is stained in blue. It appears that the microtubule network is homogeneous and dense right above the nucleus.

4.2.2. Force spectroscopy with AFM

Atomic force microscopic experiments were performed with an Agilent series 5100 AFM/STM (Agilent, Santa Clara, CA). The probe of AFM, which has been used to obtain the rheology of cancer cells is a spherical borosilicate glass probe (Novascan, Ames, IA). The spring constant of the cantilever is obtained by using an AFM option called Thermal K. which calculates the cantilever spring constant through the use of the equipartition theorem who states that the kinetic energy stored in a system, here on a coordinate which is the deflection of a cantilever from its equilibrium position, is equal to one half of the thermal energy of the system(54). The spring constant of spherical borosilicate glass probe was 0.047N/m. The radius of the spherical probe was: R= 2.5 μm. The mechanism of this AFM is represented in Fig. 2-13.

The probe of AFM which have been used to obtain the rheology of cancer cells is a spherical borosilicate glass probe (Novascan). The spring constant of the cantilever is obtained by using an option called Thermal K includes in our AFM. Thermal K calculates AFM probe spring constant by describing the motion of the cantilever as a harmonic oscillator through the use of the equipartition theorem who states that the kinetic energy stored in a system, here on a coordinate which is the deflection of a cantilever from its equilibrium position, is equal to one

half of the thermal energy of the system(54). The spring constant of spherical borosilicate glass probe (Novascan) was 0.047N/m. The radius of the spherical probe, determined from a MEB picture (cf. Fig. 4-4), was: R= 2.5 µm.

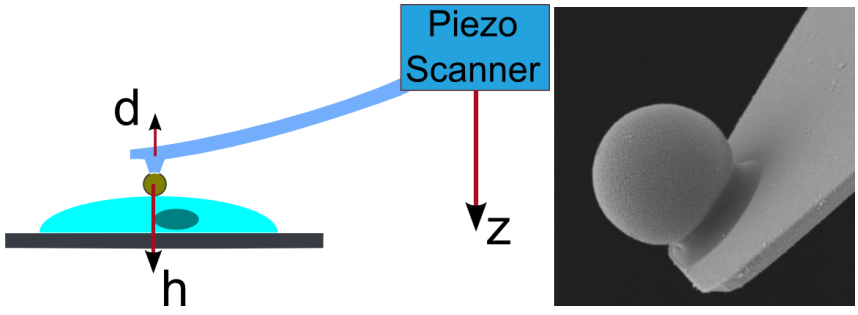

Fig. 4-4: AFM spherical probe for rheological study

The deflection d, of the cantilever is related to the applied force by:

$$F(t) = kd = k\left[z(t) - h(t)\right] \qquad (4.5)$$

Where $z(t)$ is the position of the piezoelectric transducer and $h(t)$ the indentation depth. This equation only applies when the indentation begins that is to say for a given position $z_0(t)$. For positions above the surface, the deflection can change a little bit for the highest velocity of the cantilever due to the viscosity of the feeding liquid; the corresponding force is subtracted as indicated below. In a "force spectroscopy" mode, a first detection of the surface is related to a given indentation force, which is taken as a (false) reference surface by the AFM, which needs to be corrected. A fit of the indentation curve with two parameters (the surface position and the shear modulus) is the more usual procedure. Another technique consists in comparing the work done during different indentations, which are stopped at a same given trigger force. The work done is the integral of the force displacement curve whose value is quite insensitive to the position of the surface, so, supposing the validity of the Hertz formula, it allows to relate the ratio of the shear modulus at different positions of the cell to the ratio of the indentation depths(55). This is very convenient for cartography of the shear modulus of the surface of a cell, nevertheless a reference point is needed and, above all, this method relies on the validity of the Hertz equation.

We propose here a different method which allows determining accurately the contact point of the probe with the surface and the time dependence of the force. The process is exemplified in Fig. 4-5, where the upper plot is the applied force versus time, and the lower

one is the displacement of the piezoelectric head versus time. The (false) surface is found by setting an arbitrary force for which the piezo will stop and set *z=0*; this is the initial point at *t=0* in Fig. 4-5 (**sketch A**), then the piezo retracts during 10s at a given velocity and stops 2µm above this initial position (**sketch B**) and remains in this position during 10s to reach a **plateau (P)** on the force curve. Since this plateau in the feeding liquid corresponds to a zero force we use it to find the time t_{sf} and the corresponding position z_{sf} of the piezo where the bead leaves the surface. It only needs to extrapolate the horizontal plateau when the probe is at rest well above the surface (*t=15~20s* in Fig. 4-5), to get the time t1 where the bead leaves the surface and then the corresponding position (point 2) z_{sf} of the piezo head which is associated with the surface of the cell: *h=0*. After that, the cantilever head is lowered at a given velocity (from *100µm/s* to *100nm/s*), depending on our experiment need, and stopped at a given position (**sketch C),** which is kept constant during 50s; during this time the probe continues to deep and the force is relaxing (**sketch D**). Note that the time t_2 where the bead leaves the surface was obtained from the previously determined position of the surface z_{sf} (point 3 left insert) and so the force, F_2, corresponding to this time t_2 (point 4 on the insert) can be precisely determined. Finally, the piezoelectric head is raised in 10s towards its initial position at time *t=0*; and in all our measurements we recovered the same force as the initial one (red dashed curve), showing that we did not enter into the plastic regime. Finally this procedure also gives us access to the hydrodynamic force on the cantilever*: F(t2)-F(t1)* which should be subtracted from the total force (56). Even for high velocities, here *3µm* in *0.01s*, this hydrodynamic force is rather small (around *2nN*) compared to the total force and, of course, does not play a role on the relaxation part of the force.

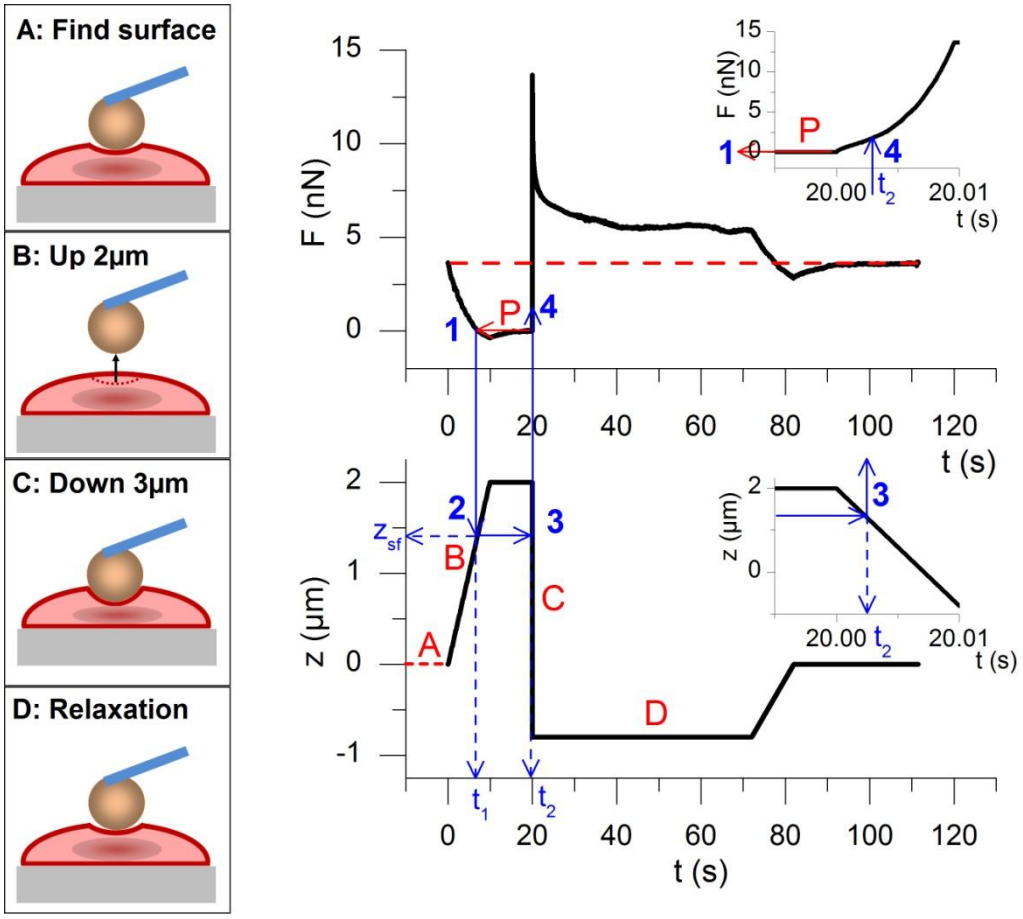

Fig. 4-5: Left is an indentation cycle; right is the method for the determination of the contact point and of the force/indentation curve. Upper graph: experimental force versus time. Lower graph: motion of the cantilever head versus time

The last important thing to note in this Fig. 4-5 is the fact that when the piezo returns to its initial position (red dash line on both graphs) the initial force is also recovered. Once again, it is a proof that there is no plastic deformation of the medium and the recovery time is about *10s* in this example.

4.3. Microrheology with a spherical indenter

4.3.1. Time dependent Hertz model

The quasi-static force is related to the indentation depth by the Hertz equation(57,58):

$$F = \frac{4}{3}\sqrt{R}\frac{G}{1-\nu^2}h^{\frac{3}{2}} \qquad (4.6)$$

or:

$$F = CGh^{\frac{3}{2}} \tag{4.7}$$

In the absence of information on the Poisson ratio, it is usual to consider the cell as an incompressible medium and to take ν=0.5 and E=3 G in this case the value of C is given by:

$$C = \frac{16\sqrt{R}}{3} \tag{4.8}$$

It is interesting to note that the Hertz formula can be recovered, within a constant number, by considering that the average strain for an indentation depth h is given by:

$$\gamma = \frac{h}{a} = \frac{h}{\sqrt{2Rh}} = \frac{h^{\frac{1}{2}}}{\sqrt{2R}} \tag{4.9}$$

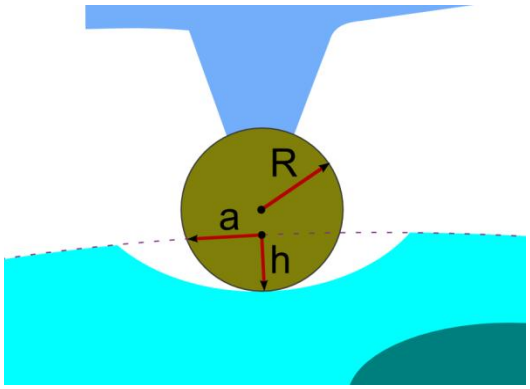

Fig. 4-6: Modeling of spherical afm probe contact with cancer cell surface, R is the radius of the probe, h the indentation of the probe

With R the radius of the spherical AFM probes. The average force is then

$$F = G\gamma S = G\gamma * 2\pi Rh \tag{4.10}$$

Where *G* is the shear modulus, and S the contact surface. We well recover the dependence in $R^{1/2}h^{3/2}$ predicted by the Hertz law but with the approximation $\gamma<<1$. We shall see in the following that, in our experimental conditions, the Hertz formula needs to be corrected. If we compare the chemical composition of both normal and cancer cells, they have the same components, more than 98% of molecules are water (12), so in the first instance, the cancer cell is usually considered as a viscoelastic liquid where the elastic part is due to the actin skeleton of the cell. The generalized Maxwell model for a viscoelastic solid consist in a

purely elastic part of shear modulus G_0 in parallel with a series of Maxwell units, cf. Fig. 4-7, representing different relaxation processes modeled by a set of relaxation times(46,57,58).

In the frame of the linear theory of viscoelasticity the increment of stress at a time t resulting from a stepwise increment of strain at time t' is given by:

$$d\sigma(t) = G(t-t')d\gamma(t') \tag{4.11}$$

Where $G(t)$ depends on the viscoelastic model under consideration. For instance, for the generalized Maxwell model represented in Fig. 4-7, we have:

$$G(t) = G_0 + G_1 e^{-\frac{t}{\tau_1}} + G_2 e^{-\frac{t}{\tau_2}} + ... + G_i e^{-\frac{t}{\tau_i}} + ... \tag{4.12}$$

It is important to note that the Eq.(4.12) is not directly relevant to the case where the contact surface between the medium and the tool is changing with time, which is presently the case. Actually the generalization of the Hertz model to the dynamic response of the force starts with Eq.(4.10). The increment of force at time t is related to the increment of indentation at time $dh(t')$ by:

$$dF(t) = CG(t-t')dh(t')^{\frac{3}{2}} \tag{4.13}$$

Where C is given by Eq.(4.8) in order to recover the Hertz formula in the static case .

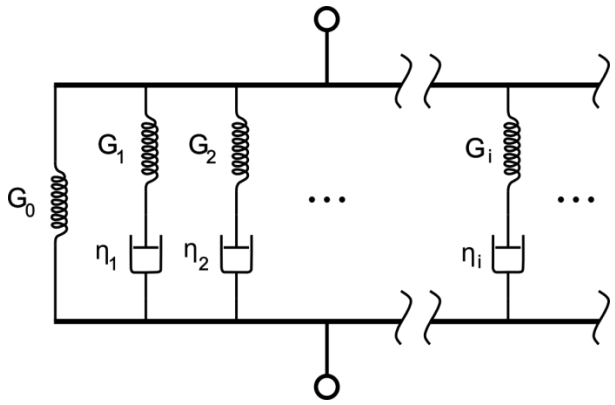

Fig. 4-7: Schematic representation of the Generalized Maxwell model

Integrating the Eq.(4.13) gives:

$$F(t) = C\int_0^t G(t-t')\frac{dh(t')^{\frac{3}{2}}}{dt'}dt' \tag{4.14}$$

or still:

$$F(t) = C\left[G(0)h(t)^{\frac{3}{2}} + \int_0^t \dot{G}(t-t')h(t')^{\frac{3}{2}} dt' \right] \tag{4.15}$$

This is a general formula for a spherical probe indenter, the rheological properties of the material being represented by the stress response function: $G(t)$. The same kind of reasoning with the compliance response function $J(t)$ will give:

$$h^{\frac{3}{2}}(t) = C'\int_0^t J(t-t')\frac{dF(t')}{dt'}dt' = C'\left[J(0)F(t) + \int_0^t \dot{J}(t-t')F(t')dt' \right] \tag{4.16}$$

$$h^{\frac{3}{2}}(t) = C'\left[J(0)F(t) + \int_0^t \dot{J}(t-t')F(t')dt' \right] \tag{4.17}$$

with $C' = 1/C$

The relation between the two response functions is obtained by taking the Laplace transform of the convolution products Eq.(4.14) and (4.16) which will give:

$$G(p)J(p) = p^{-2} \tag{4.18}$$

Eq.(4.16) and (4.17) are simply a time dependent generalization of the Hertz formula. If the relative indentation depth h/R, or the indentation depth relatively to the thickness of the sample: h/L, are not much smaller than unity, then these formula need to be corrected, that is what we are going to see in the newt section.

4.3.2. Corrections to the Hertz model

The Hertz model is known to be accurate only for small values of the contact area with respect to the radius of the probe. For larger indentation the corrections depend on the Poisson ratio (59,60). In order to find a correction adapted to our experimental conditions, we took ν=0.5 and compared, for a large indentation, the force calculated by FEM (using the software Abaqus) with the Hertz equation for a purely elastic cylindrical plate whose thickness and radius were very large compared to the probe radius (R=2.5µm). The thickness L and the radius of the cylinder were both taken equal to 200µm. The Young modulus E was 575 Pa corresponding to a value measured on a cancer cell. We found a small difference(4% for

h=1μm) between the Hertz equation and the result obtained by FEM. Introducing a first order correction factor in the Hertz equation (Eq.(4.19)), gave a result which very well reproduces the FEM result until h/R=0.4 :

$$F = \frac{4E\sqrt{R}}{3(1-\nu^2)} h^{\frac{3}{2}} \left(1 - \frac{h}{10R}\right) \tag{4.19}$$

On the other hand the effect of the thickness L on the force was calculated as an expansion in a small parameter $\frac{2\alpha_0}{\pi}\frac{\sqrt{R}}{L}$, In this case, the Hertz equation can be written as:

$$F = \frac{4E\sqrt{R}}{3(1-\nu^2)} h^{\frac{3}{2}} f(h) \tag{4.20}$$

Where:

$$f(h) = \left[1 - \frac{2\alpha_0}{\pi}\frac{\sqrt{R}}{L}\sqrt{h} + \frac{4\alpha_0^2}{\pi^2}\frac{R}{L^2}h - \frac{8}{\pi^3}\left(\alpha_0^3 + \frac{4\pi^2}{15}\beta_0\right)\frac{R^{3/2}}{L^3}h^{\frac{3}{2}} + \frac{16\alpha_0}{\pi^4}\left(\alpha_0^3 + \frac{3\pi^2}{5}\beta_0\right)\frac{R^2}{L^4}h^2\right] \tag{4.21}$$

$$\alpha_0 = -\frac{1.2876 - 1.4678\nu + 1.3442\nu^2}{1-\nu}$$

$$\beta_0 = \frac{0.6387 - 1.0277\nu + 1.5164\nu^2}{1-\nu}$$

Once again, there is a small difference between this modified Hertz equation Eq.(4.20) (Light green curve) and FEM (dark green bold curve), but this difference disappears by using the same correction as in Eq.(4.19). Finally the generalized expression of the Hertz model (Eq.(4.22)), represented by the green dotted curve with squares in the Fig. 4-8 is in excellent agreement with the FEM result.

$$F = \frac{4E\sqrt{R}}{3(1-\nu^2)} h^{\frac{3}{2}} \left(1 - \frac{h}{10R}\right) f(h) \tag{4.22}$$

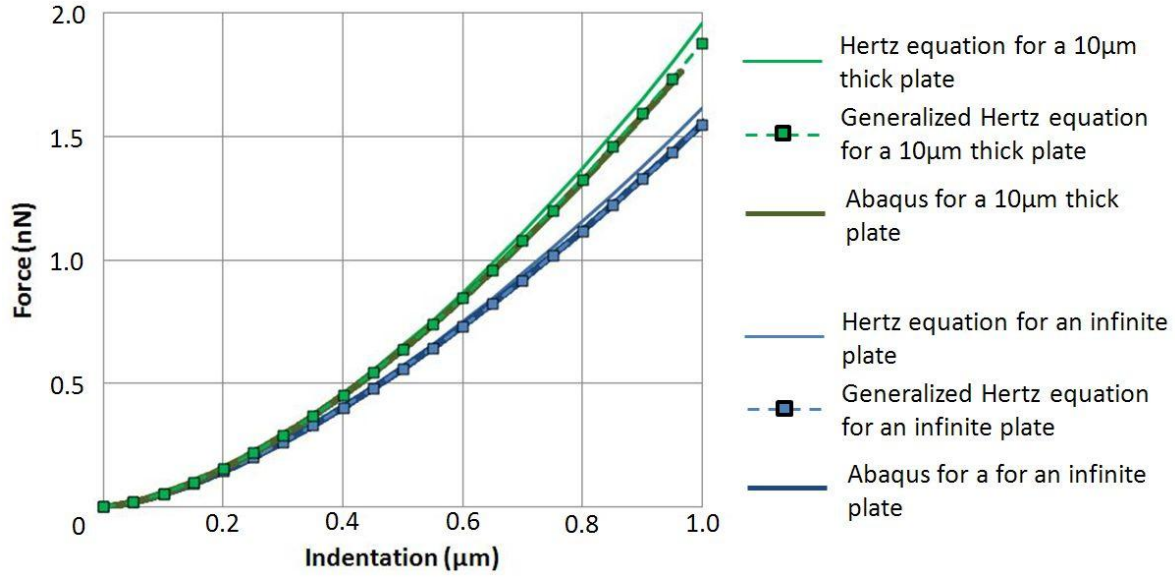

Fig. 4-8: Calculation of the force with respect to the indentation using Abaqus, the Hertz model and the generalized Hertz model in the case of an infinite elastic plate and of a 10µm thickness plate

The time dependent generalizations of these two corrections are straightforward. Let us call $g(h)$ the function which multiplies the Hertz equation:

$$g(h)=\left(1-\frac{h}{10R}\right)f(h) \tag{4.23}$$

Then, instead of applying the time superposition to $h^{3/2}$ it should be applied to $h^{3/2}g(h)$ so Eq.(4.17) becomes:

$$F(t)=C\int_0^t G(t-t')\frac{d}{dt'}\left[h(t')^{\frac{3}{2}}g(h(t'))\right]dt' \tag{4.24}$$

or

$$F(t)=C\left[G(0)h(t)^{\frac{3}{2}}g(h(t))+\int_0^t \dot{G}(t-t')\frac{d}{dt'}\left[h(t')^{\frac{3}{2}}g(h(t'))\right]dt'\right] \tag{4.25}$$

Before applying Eq.(4.24)) to find the function $G(t)$ from an experiment it is worth testing its application to a material represented by the popular Zener model.

4.3.3. Penetration of a sphere in viscoelastic medium

We wish to predict the trajectory of the spherical probe inside a viscoelastic material represented by the popular Zener model consisting of a spring in parallel with a Maxwell element. For this model the response function to a unit stress step is:

$$G_z(t) = G_0 + G_1 e^{-\frac{t}{\tau_1}} \tag{4.26}$$

And from Eq. (4.25)

$$F(t) = C\left[\left(G_0 + G_1\right) h(t')^{\frac{3}{2}} g(h(t)) - F_1(t) \right] \tag{4.27}$$

With $F_1(t) = \frac{G_1}{\tau_1} \int_0^t e^{-\frac{t-t'}{\tau_1}} h(t')^{\frac{3}{2}} g(h(t'))dt'$

Deriving Eq.(4.27) and taking into account that:

$$\dot{F}_1(t) = -\frac{F_1(t)}{\tau_1} + \frac{G_1}{\tau_1} h(t)^{3/2} g(h(t) \tag{4.28}$$

and (cf. Eq.(4.5)) that: $\dot{F}(t) = k\left[\dot{z}(t) - \dot{h}(t) \right]$

We shall end up in the case of the Zener model with the following equation

$$\frac{dh}{dt} = \frac{C\left[\frac{dz}{dt} + \frac{z(t)}{\tau_1} - \frac{h}{\tau_1} \right] - \frac{G_0}{\tau_1} h^{\frac{3}{2}} \left(1 - \frac{h}{10R}\right) f(h)}{(G_0 + G_1)\left[Q(h)\left(1 - \frac{h}{10R}\right) - \frac{h^{\frac{3}{2}}}{10R} f(h) + \frac{3}{2}\sqrt{h}\left(1 - \frac{h}{10R}\right) f(h) \right]} \tag{4.29}$$

Where

$$Q(h) = -\frac{\alpha_0}{\pi}\frac{\sqrt{R}}{L} h + \frac{4\alpha_0^2}{\pi^2}\frac{R}{L^2} h^{\frac{3}{2}} - \frac{12}{\pi^3}\left(\alpha_0^3 + \frac{4\pi^2}{15}\beta_0 \right)\frac{R^{\frac{3}{2}}}{L^3} h^2 + \frac{32\alpha_0}{\pi^4}\left(\alpha_0^3 + \frac{3\pi^2}{5}\beta_0 \right)\frac{R^2}{L^4} h^{\frac{5}{2}} \tag{4.30}$$

$$C = \frac{3k}{16\sqrt{R}} \tag{4.31}$$

In order to check the validity of this approach the indentation and the force versus time are calculated from Eq.(4.29) and compared with the result obtained from a simulation done with the software Abaqus. In Abaqus, a 2D axisymmetric geometry is used; the cantilever is represented by a spring of stiffness 0.05N/m and the spherical probe by a rigid sphere (Fig. 4-9). The cell is modeled by a plate with thickness L whose viscoelastic properties defined by the Zener model are the following: G_0=191.6Pa, G_1=118.4Pa, τ_1=8.4s which are those obtained for a given cell.

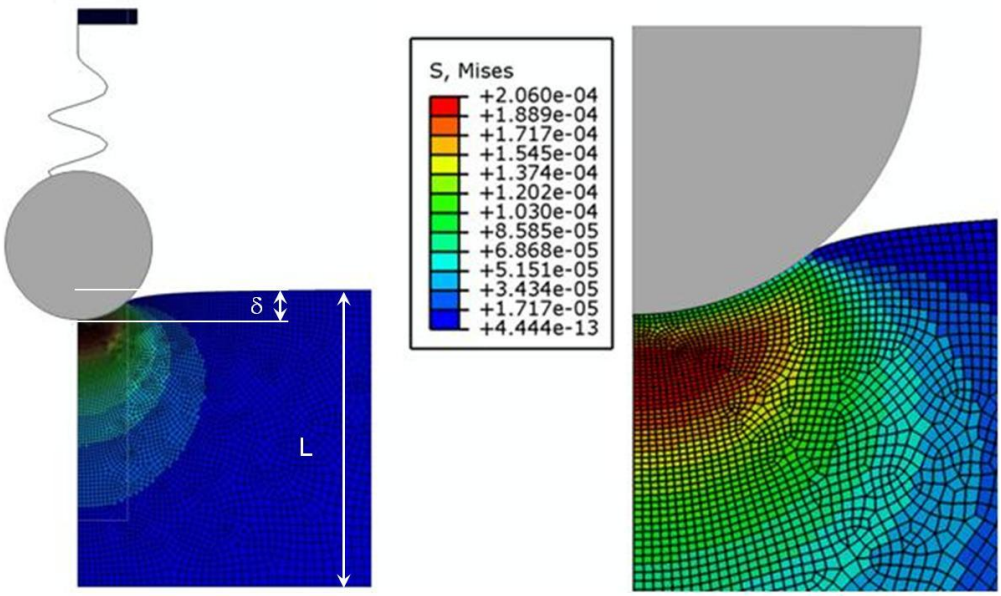

Fig. 4-9: Calculation of the force with respect to the indentation in a viscoelastic medium with a spherical probe mounted on a spring using the software Abaqus

The result is shown in Fig. 4-10 where the force is plotted versus time when a slow displacement at a velocity of 0.1µm/s during 10 seconds is applied on the top of the spring and stopped at z=1µm for larger time. The numerical solution of the differential equation (4.29) is compared to the Abaqus result for a plate whose thickness is infinite (L=200µm in Abaqus) and for finite thicknesses of 5 and 10µm. Fig. 4-10 shows a very good agreement between FEM calculation and the solution of Eqs.(4.29)(4.31) in all cases, so we can say that the corrections used for the Hertz formula and its generalization to time dependent forces are the right ones. Now that we are sure that these corrections and the way to generalize them to time dependent phenomena are correct, we wish to find the material properties for any kind of representation, and not only for the Zener model.

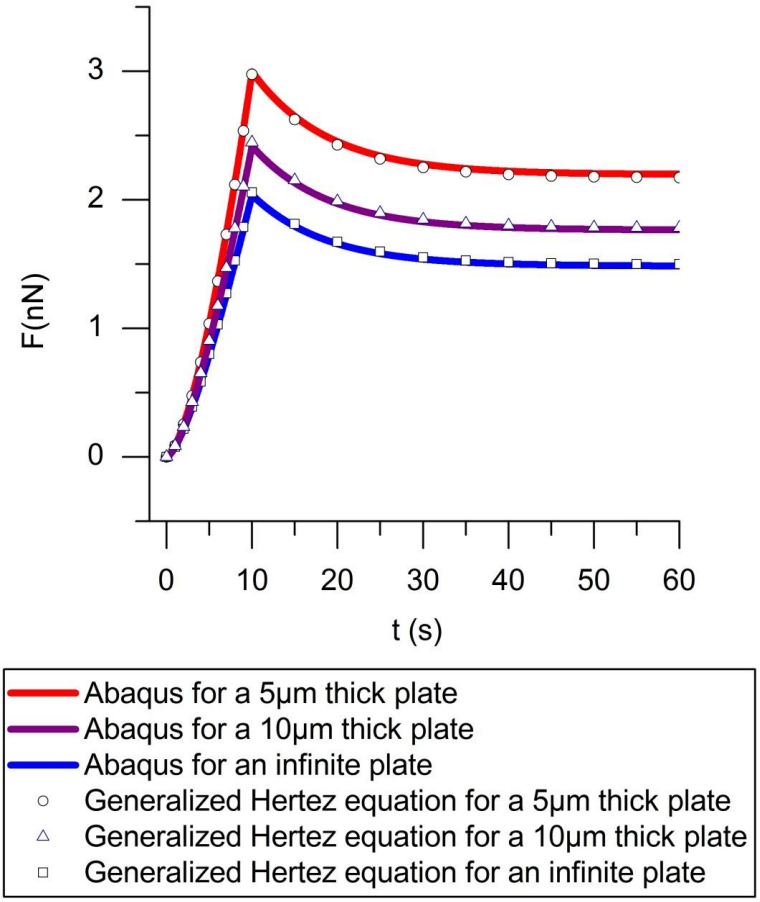

Fig. 4-10: Comparison between FEM result and the solution of Eq. (4.29) for the indentation versus time in disks of different thicknesses

Another interesting point revealed by the FEM calculation is that the maximum stress generated by the motion of the spherical probe is not situated directly on the surface of the probe but below, on the axis of indentation (cf. Fig. 4-9) This maximum stress depends on the indentation depth and, as long as no plastic flow is experimentally observed, it determines the range of stress that the cell can support without yielding. In Fig. 4-11 is plotted, in the case of a purely elastic medium, the evolution of the maximum stress with the indentation depth. The average stress can be approximated by putting: $\sigma=F/(2\pi Rh)$ with F given by Eq.(4.20). Of course this average stress is lower than the maximum stress (cf. Fig. 4-11:), but it is quite remarkable that the ratio between the maximum stress and the average one, remains approximately constant with the indentation at a value of about 1.6 up to $0.6\mu m$ and then increases slowly until 1.8 for a deepness of $1.7\mu m$.

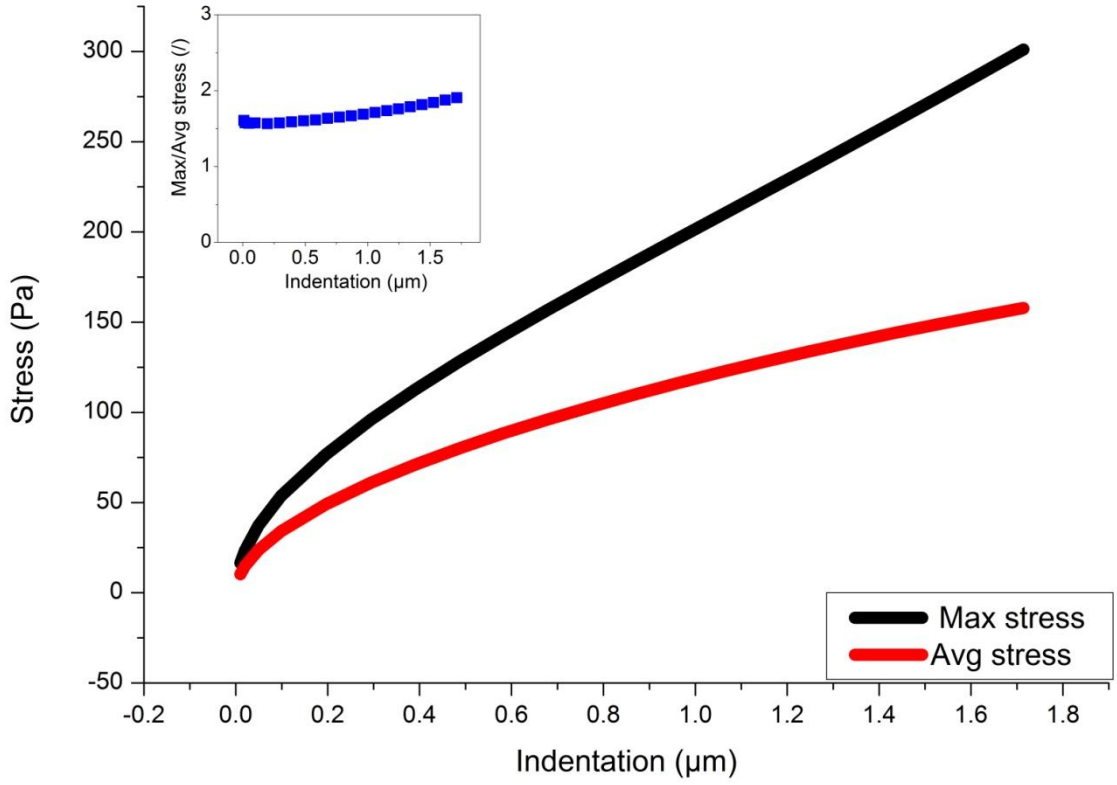

Fig. 4-11: Maximum and average stress with respect to the indentation depth for a purely elastic medium; the diameter of the bead is 5µm and the thickness of the layer is 10µm; the insert is the ratio of maximum stress to average stress

4.3.4. Deriving the material properties

Eq.(4.27) is a general equation relating the force, F(t), and the indentation, h(t), which are both known experimentally, to the response function G(t). In principle it is possible to extract G(t) by taking the Laplace transform of the convolution product in order to get G(p) and then to come back by inverse Laplace transform to G(t). Nevertheless ,the time scale on which the force is measured is not infinite as in a convolution product and the experimental data can be noisy, so the error coming from this double Laplace transform is difficult to evaluate; furthermore , even if we can get a reliable result for G(t) , we would like to compare it with known models. In practice it is much easier to directly begin with a given model for G(t) -like for instance the generalized Maxwell model of Fig. 4-7 and to see afterwards if this model can well represent the experimental curve. As an example of this procedure let us suppose that the function G(t) of Eq.(4.12) well describes the viscoelastic properties of the material; then using Eq. (4.12) for G(t) and inserting it in Eq.(4.25) gives:

$$F(t) = C\left[\sum_{i=0}^{n} G_i h(t)^{\frac{3}{2}} g(h(t)) - \sum_{i=0}^{n} F_i(t)\right] \tag{4.32}$$

Where $F_i(t) = \frac{G_i}{\tau_i}\int_0^t e^{-\frac{t-t'}{\tau_1}} h(t')^{\frac{3}{2}} g(h(t'))dt'$

This is just the generalization of Eq. (4.27) to a set of relaxation times.

In a fit of the parameters G_0, G_i, τ_i, ($i=1, n$), the force $F(t)$ is the experimental function whose values are known for a given set of time values: $F_{exp}(t_j)$ ($j=1,N$) and the left-hand side of Eq.(29) is the "theoretical" part: $F_{th}(t_j,G_0,G_i,\tau_i)$ containing the unknown parameters. The minimization of the residue, using the Levenberg-Marquardt method allows finding the unknown parameters. This procedure can, of course, be used for any kind of function $G(t)$ and will be used in the following both for the generalized Maxwell model (Eq.(4.12)) and a power law relaxation function: $G(t)=At^{\alpha}$

4.4. Results

As explained in section 4.2.2 all the experimental curves have been obtained in force spectroscopy mode with different velocities of the piezoelectric transducer on which is attached the cantilever head. The final position was corresponding to an indentation depth of about 1μm. The small viscous force coming from the hydrodynamic friction of the cantilever in the feeding liquid was subtracted and the indentation depth, $h(t)$, was obtained as shown in Fig. 4-4. The indentation was stopped at a time $t=t_s$. If there was no relaxation during the rising time, or in other words if $t_s << \tau_i$, then the terms $F_i(t)$ in Eq.(4.32) are negligible and the force at $t=t_s$ can be expressed as:

$$F(t) = C\left[\sum_{i=0}^{n} G_i h(t)^{\frac{3}{2}} g(h(t))\right] \tag{4.33}$$

This is the hypothesis which is usually done (48)(49) when dealing with the relaxation part for $t>>t_s$. It means that at $t=t_s$, which is the starting point of the relaxation curve, Eq.(4.33) gives access to the sum of the shear moduli of the model, which is called the high frequency modulus:

$$G_\infty = G_0 + G_1 + G_2 + \cdots \tag{4.34}$$

On the contrary, if the time t_s is longer than all the relaxation times, the integrand representing $F_i(t)$ in Eq.(4.32) will be different from zero only for $t\text{-}t' < \varepsilon$ where $\varepsilon << t_s$, so the term containing $h(t)$ can be taken out of the integral in $F_i(t)$ with its final value $h(t_s)$; then considering that $t_s >> \tau_i$ we shall end up with:

$$F\left(t_s\right) = CG_0 h\left(t_s\right)^{3/2} g\left(h\left(t_s\right)\right) \tag{4.35}$$

This is now the low frequency limit of the shear modulus which is measured at $t=t_s$ but in this situation the indentation is a quasi static one and after stopping there will be no relaxation. This is the way to obtain the static shear modulus G_0.

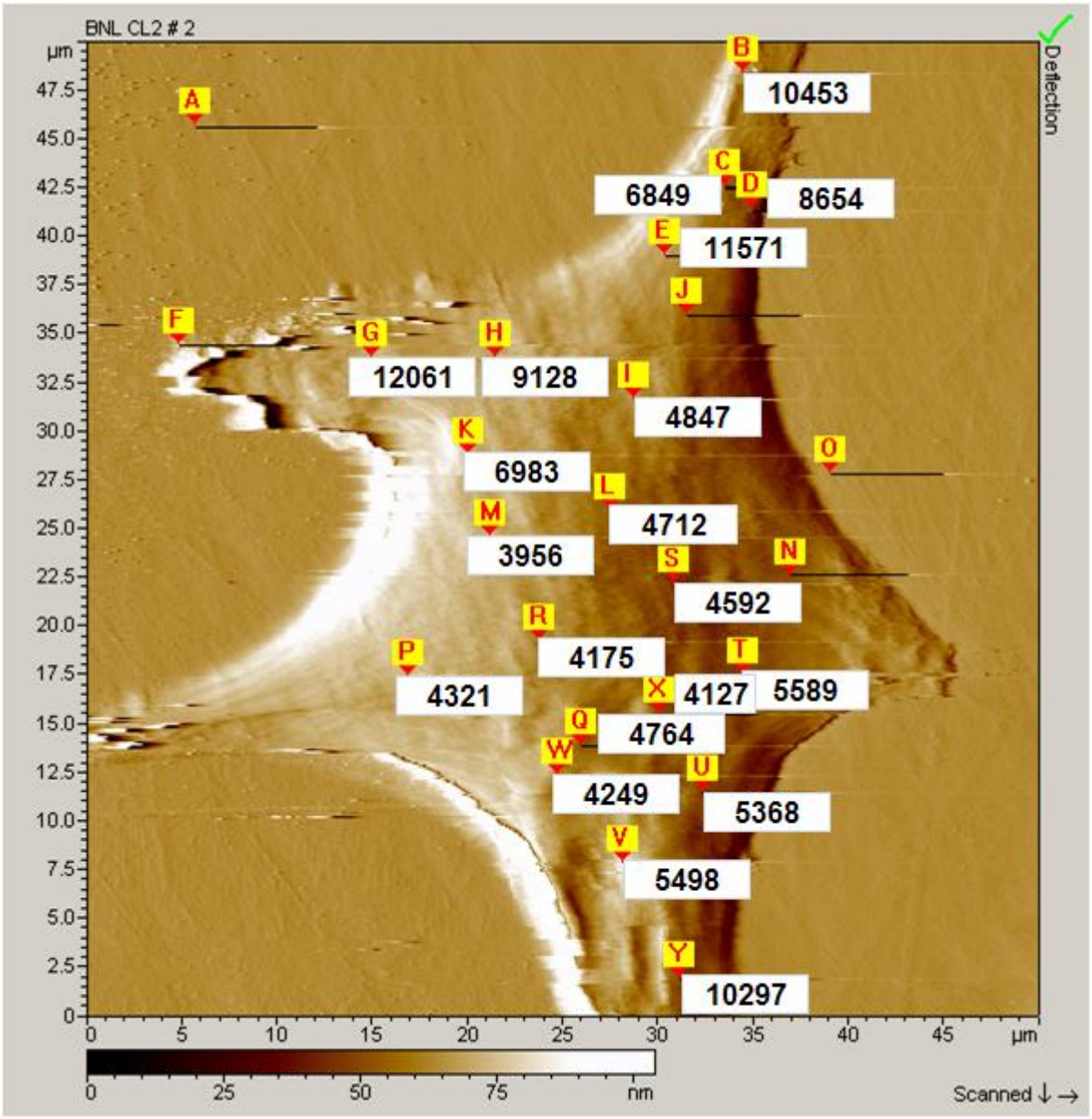

Fig. 4-12 The map of Young's modulus of BNL C2

The value of the Young modulus can depend quite strongly on the location of the probe on the cell as shown in Fig. 4-12 for a BNL-C2 , especially if the measurement is done on the edge of the cell

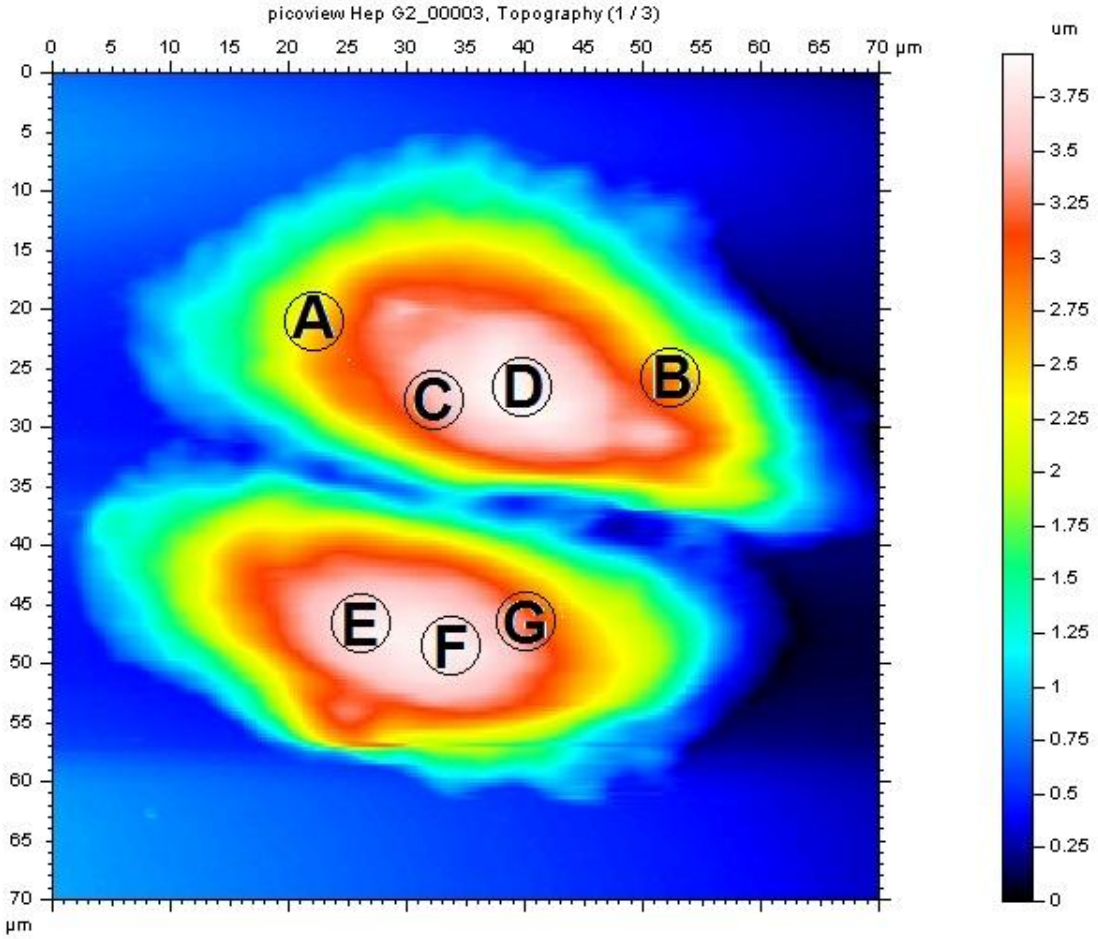

Point	A	B	C	D	E	F	G
E(Pa)	731	894	621	465	545	513	618

Fig. 4-13: AFM topography of Hep G2 cell, the point A to G are the place where the measurements have been carried out

All the experiments that we are going to discuss in the following were made on the central part of the cell where the height of the cell is maximum and is about 4 µm. Actually, as shown in Fig. 4-13 and in the table just below, the values of G_0 do not vary significantly for different points in the region above the nuclei in the white zone (points *E*, *F*, *D*), but they increase when the measurement is done closer to the border of the cell. These measurements were made in a quasi static way; on the other hand, if only the relaxation part of the force is used then t_s needs to be as small as possible to minimize the error, but in any event it will be safer to fit the full curve from the beginning of the indentation. In order to illustrate this point we have presented in Fig. 4-14 the values of the shear modulus which are obtained from Eqs. (4.33) or (4.34) after an indentation made at different velocities on the same cell. It clearly

shows that the shear modulus obtained in this way depends on the indentation velocity but this value has no clear meaning in the frame of the viscoelastic models and only a fit of the total indentation curve can allow to attribute safely the values of the fitted parameters to a given model as we shall see in the next section.

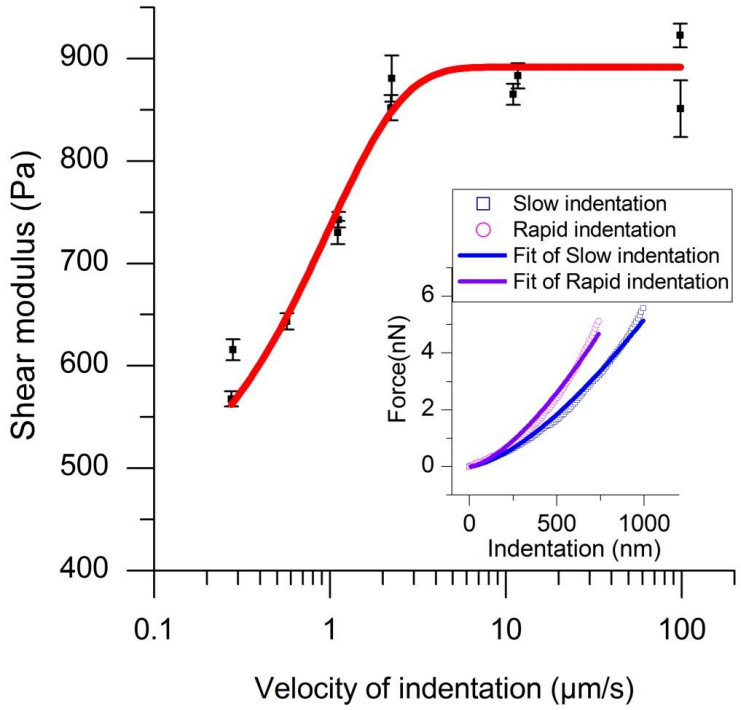

Fig. 4-14: Young's modulus versus indentation velocity. In the insert: force versus indentation for two different velocities (v=100µm/s and 100nm/s) and their fit by Eq. (4.22)

4.4.1. Response function G(t) of the cells Hep G2

A typical curve representing the force versus time for a "slow" velocity of the cantilever: *v=0.25µm/s* is plotted in; the indentation depth corresponding to the maximum of the force is h_s*=1.08µm*. The force (black square line) passes through a maximum when the cantilever stops and then decreases as the probe continue to go down until the elastic stress becomes equal to the stress applied by the cantilever. This curve was fitted with the generalized Maxwell model with a single branch (Zener model) for the 3 parameters: G_0, G_1, τ_1.

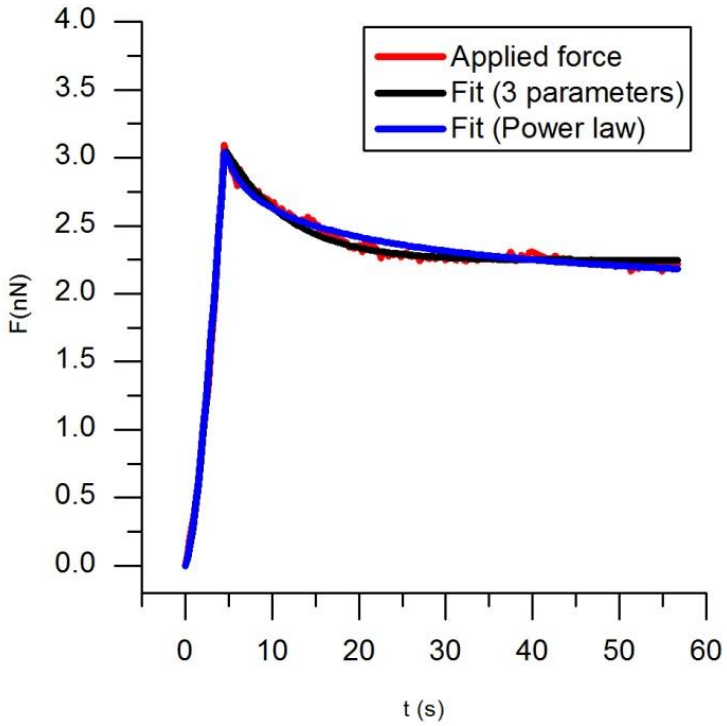

Fig. 4-15: Applied force (in red) versus time during an indentation with a velocity: v=0.25µm/s and a maximum indentation depth: h_s=1.08µm .The blue triangles represent a fit with a power law for G(t) and the black circles a fit with a one branch Maxwell model

As can be seen in Fig. 4-15, the fit is good on all the time scale for the following parameters: G_0=198Pa, G_1=101Pa, τ_1=7.1s. This model was also observed to give a good representation of the viscoelasticity of some bacterial cells(49) and of chondrocytes(48). Nevertheless it is worth noting that in these previous works the fit was only done on the relaxation part of the curve, supposing that the indentation was fast enough so that the medium did not have time to relax during the indentation. If this hypothesis was used for the experiment represented in Fig. 4-15 the relaxation part would be fitted by the function:

$$F\left(t-t_s\right)=Ch_s^{3/2}g\left(h_s\right)\left(G_0+G_1e^{-\frac{t-t_s}{\tau_1}}\right) \text{ when } t\geq t_s \qquad (4.36)$$

Where t_s and h_s are respectively the time and the indentation corresponding to the maximum of the force. In our example it would give G_0=203Pa, G_1=70Pa, τ_1=8.4s instead of G_0=198Pa, G_1=101Pa, τ_1=7.14s. The error is not that big, the maximum error being 40% for G_1, nevertheless the degree of approximation of Eq.(4.36) depends on the importance of G_1 compared to G_0 and on the relaxation time τ_1 compared to t_s since it supposes that for t=t_s the modulus is equal to G_0+G_1, that is to say that the material did not have time to relax during

the rising indentation.. On the other hand it is clear that the velocity of the cantilever head will give a limit on the smaller relaxation time which can be detected: roughly speaking a relaxation time which would be smaller than t_s would not be detected. In practice our Hep G_2 cell gives a good example of this remark. In Fig. 4-16 is plotted the force versus indentation for a velocity of the piezoelectric head: *v=250µm/s* and about the same indentation depth h_s*=1.27µm*. The maximum of the force is higher than in Fig. 4-15, and above all, shows a very fast relaxation of large amplitude. A fit of this curve with a single relaxation time, τ_1, (red circle curve in Fig. 4-16) no longer works, and it is necessary to add another relaxation time, τ_2, to give a satisfying agreement (blue triangle curve).

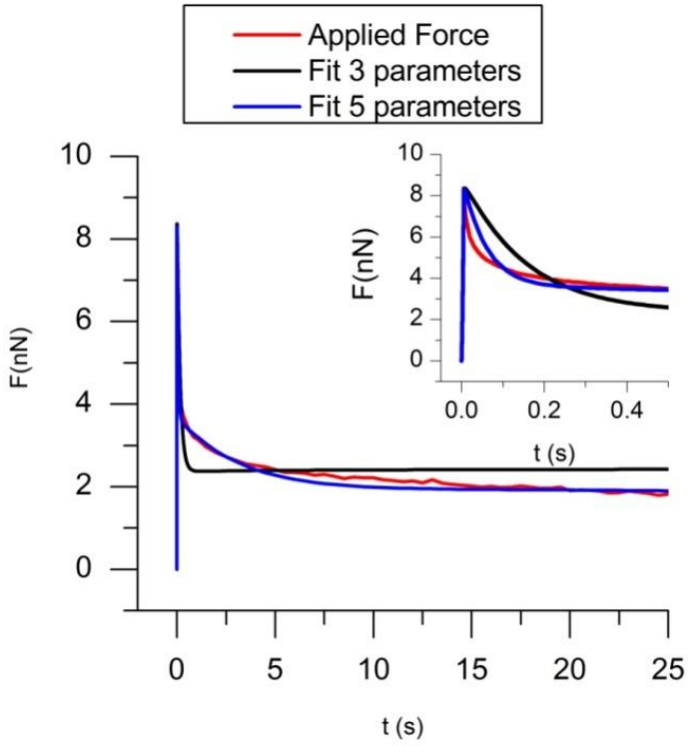

Fig. 4-16 : Rapid indentation: applied force versus time during an indentation with a velocity: v=250µm/s. Red dots represent a fit with 3 parameters (the Zener model) for G(t) and the blue triangles a fit with 5 parameters (two Maxwell branches)

The results obtained on several experiments both for fast and slow indentation velocities are summarized in Tab 1. In parentheses are the values calculated without taking into account the thickness of the cell which overestimates the moduli of about *15-20%* because the increase of stiffness due to the presence of the bottom wall was attributed to the elasticity of the cell. The rapid relaxation time τ_2*=0.06s* associated with a modulus G_2 of about *450Pa* means that some elastic part of the cytoplasm, whose elasticity is more than two times larger than the static one,

is associated with a rather low friction during its relaxation ($\eta_2=\tau_2 G_2=27Pa.s$) compared to the one associated with the slow relaxation process ($\eta_1=\tau_1 G_1=450Pa.s$). In previous experiments, either with AFM [18] or with specific devices like microplates [2], the time scale of the indentation or of compression in the case of microplates was much longer so a Zener model with a single Maxwell time as in Fig.8 was able to represent the viscoelastic behavior of the cell and this fast relaxation time associated with a lower viscosity was not detected.

Slow indentation	G_0	G_1	τ_1
Average	210 (247.6)	118.4 (128.3)	5.6 (6.1)
Standard deviation	22.8 (28.5)	19.8 (20.7)	2.1 (2.2)

Rapid indentation	G_0	G_1	τ_1	G2	τ_2
Average	184.3 (214.5)	149.4 (168.6)	3.07 (3.84)	451.4 (538.5)	0.057 (0.065)
Standard deviation	65.8 (74.0)	30.2 (35.1)	0.99 (1.16)	110.2 (142.7)	0.003 (0.018)

Tab 1: Viscoelastic parameters deduced from a fit of G(t) with the generalized Maxwell model (Eq.(4.32)) with one Maxwell branch for slow indentation and two Maxwell branches for rapid indentation; the thickness of the cell was taken as L=10μm; the values between parenthesis are obtained for an infinite medium

Different branches of the Maxwell model can tentatively be associated with different deformations of the actin network; the first spring with the shear modulus G_0 gives the solid like behavior and is likely mainly due to the enthalpic bending stiffness of the actin network. The first Maxwell branch could represent the entropic part associated with the shear elongation of the crosslinks and the second Maxwell branch with a faster relaxation and a higher modulus could come from the change of entropy associated with the compression of the main filaments of the network(61). Of course many others explanations can be proposed, but the interest of the Maxwell model is that it can be interpreted more easily than other models on a physical basis. Another model which is often used too represents the viscoelastic behavior of gels consists in a power law distribution of the relaxation times:

$$G(t)=\frac{1}{A}\frac{1}{\Gamma(\alpha+1)}\frac{(t+t_0)^{-\alpha}}{\Gamma(1-\alpha)}=\frac{B}{(t+t_0)^{\alpha}},\qquad 0<\alpha<1 \tag{4.37}$$

It was also argued to represent the viscoelastic response of the actin network, leading to a power law for the creep relaxation function(50):

$$J(t) = At^{\alpha} \tag{4.38}$$

The Laplace transform of $J(t)$ is:

$$J(p) = A\frac{\Gamma(\alpha+1)}{p^{\alpha+1}} \tag{4.39}$$

Since the Laplace transforms of $G(t)$ and $J(t)$ are related by $G(p)J(p)=p^{-2}$ (cf. Eq.(4.18)) it is easy to show that $G(t)$ will be given by:

$$G(t) = \frac{1}{A}\frac{1}{\Gamma(\alpha+1)}\ \frac{(t+t_0)^{-\alpha}}{\Gamma(1-\alpha)} = \frac{B}{(t+t_0)^{\alpha}}, \qquad 0<\alpha<1 \tag{4.40}$$

Where $B = \dfrac{1}{A\Gamma(\alpha+1)\Gamma(\alpha-1)}$ (4.41)

Formally we should have $t_0=0$ but this time shift is an ersatz which is used to avoid the divergence of $G(t)$ in $t=0$(62). In practice the fitting realized on the three parameters, B, α, t_0, knowing that t_0 should be small compared to the relevant relaxation times. This power law gives a reasonable fit although not as good as the Zener model for a slow indentation, with parameters: $t_0=0.056s$, $B=288.3$, $\alpha=0.104$ (cf. blue curve in Fig. 4-15). In the case of a rapid indentation, the comparison between the Maxwell model with two relaxation times and the power law model is shown in Fig. 4-16. The obtained parameters were $t_0=0.016$, $\alpha=0.265$, $B=199$; clearly the agreement with the experimental curve is less satisfactory for the power law model than for the Maxwell model with two relaxation times, especially at short times where the decrease of the force is too slow (insert of Fig. 4-16). Nevertheless it is worth noting that the value of the coefficient α is not very different from the one $\alpha=0.20$ found by a different experimental method (50).

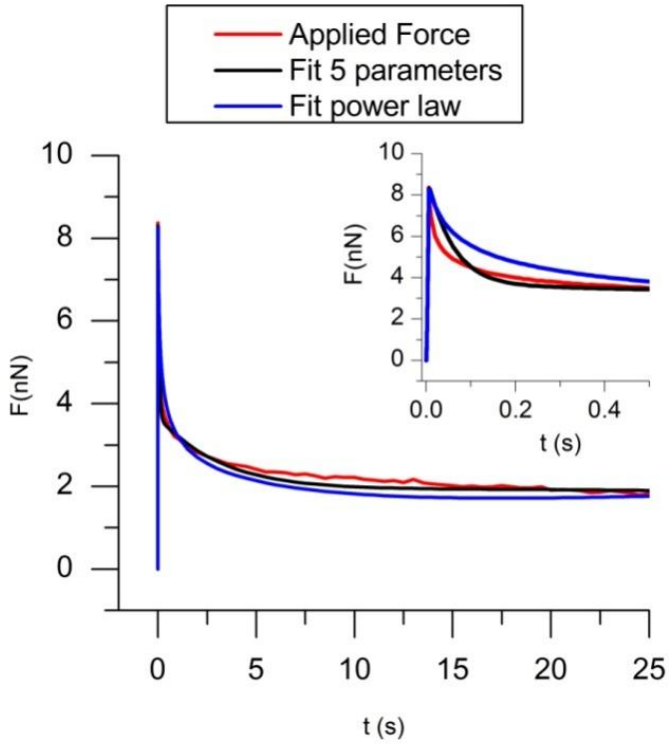

Fig. 4-17 : Same conditions as in Fig. 4-16 Comparison between a fit with two Maxwell branches and a fit with a power law

The comparison of these two models is still more instructive in the frequency domain. The real part of the shear modulus is given by

$$G'(\omega) = \Re\left[pG(p) \right] \tag{4.42}$$

Which leads respectively for the Maxwell and the power law model to:

$$G'_M(\omega) = G_0 + \frac{G_1\omega^2}{\omega^2 + \left(\frac{1}{\tau_1}\right)^2} + \frac{G_2\omega^2}{\omega^2 + \left(\frac{1}{\tau_2}\right)^2} \tag{4.43}$$

And

$$G'_P(\omega) = \Re\left[Be^{j\omega t_0} (j\omega)^{\alpha} \Gamma(1-\alpha, t_0) \right] \tag{4.44}$$

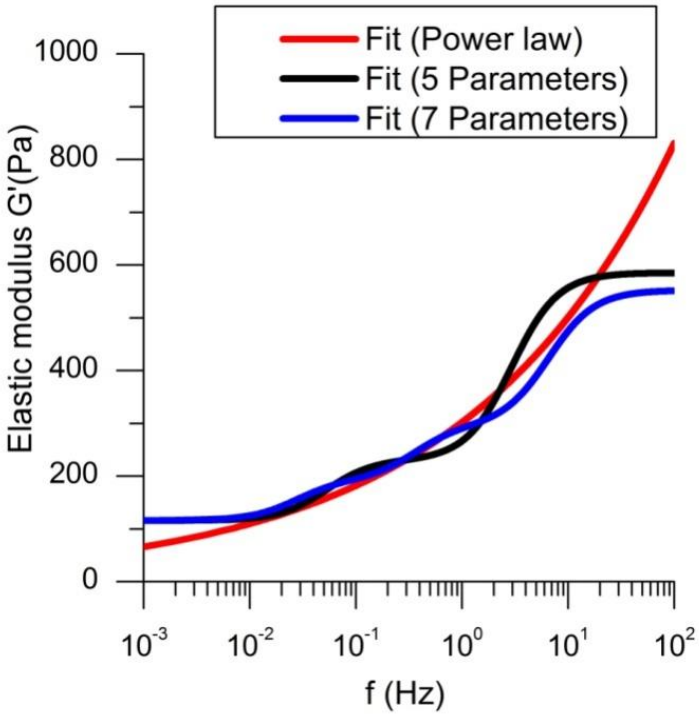

Fig. 4-18 : Frequency dependence of the real part of the shear modulus: G'(ω) deduced from the fit of G(t) by different models. Black line: power law model (Eq.(4.44)), redline: Maxwell model with two branches (Eq.(4.42)), Blue line: Maxwell Model with three branches

Note in Eq.(4.44) the presence of t_0 in the imaginary exponential which would give a non physical oscillation for $\omega > 1/t_0$. In Fig. 4-18, we put $t_0=0$ and the incomplete gamma function $\Gamma(1-\alpha,t_0)$ becomes $\Gamma(1-\alpha)$ so:

$$G'(\omega) = B\Gamma(1-\alpha)\cos\left(\frac{\alpha\pi}{2}\right)\omega^{\alpha} \qquad (4.45)$$

The red curve clearly shows the two relaxation frequencies of the generalized Maxwell model, and a high frequency plateau, whereas the power law model shows a continuously increasing modulus. The addition of more than two relaxation times in the generalized Maxwell model is difficult to perform because of too many parameters which can give similar residue for different set of parameters; it can improve a little bit the fit and gives a smoother frequency dependency (blue line in Fig. 4-18) but in any event it remains true that both at low and high frequencies the behavior of the two models remains very different. At low frequency we find clearly a zero frequency modulus, G_0 corresponding to a constant position of the indenter after the relaxation sequence; this also confirmed by the elastic recovery of the indenter position at the end of the cycle described in Fig. 4-5 whereas in the power law model there is

a continuous decrease of the modulus with the frequency. Actually it is possible to add a zero frequency modulus in Eq.(4.40) to take into account the solid like behavior, but at high frequency we find a plateau with the Maxwell model contrary to the power law model. This plateau is, of course, inherent to the Maxwell model and is imposed by the shortest relaxation time; it could be that experimentally it is not possible to test higher frequencies because the indentation velocity is limited. Actually, as can be seen in Fig. 4-14, we are well able to detect this plateau for indentation velocity higher than 10μm/s. Furthermore, as can be seen in the insert of Fig. 4-17, the experimental relaxation is faster than the one predicted by the power law model, which means that this model does not well capture the physics of the relaxation process in the high frequency range. This frequency cut-off could be, for instance, related to a typical unbinding time of crosslinks, which blocks the relaxation of the actin network for smaller times (63).

4.5. Conclusions

In the section 4.2 of this paper it was shown, with the help of a comparison with FEM results on a viscoelastic solid, that a generalized Hertz theory was very well adapted to describe, not only the relaxation part, but the whole indentation curve, obtained with a spherical probe mounted on the tip of an AFM. Furthermore this equation takes into account the finite thickness of the cell with respect to the indentation depth. In the case of a Zener model, the differential equation relating the indentation to the vertical motion, $z(t)$ of the piezoelectric transducer can be written explicitly: Eq.(4.29) whatever the shape of $z(t)$. For any creep function $G(t)$, the integral equation Eq.(4.25) can be used to obtain the parameters included in the function $G(t)$. A proper determination of the contact between the probe and the cell and also the correction due to the viscous dissipation on the cantilever was proposed and described in Fig. 4-5. Based on these methods, the viscoelastic properties of Hep G2 cancer cells were obtained. It appears that high velocities of indentation reveal a short relaxation time which is generally ignored due to the use of smaller indentation velocity, This is for instance the case in studies(35),(64), where the typical time of compression was several seconds which did not allow to observe this fast relaxation time. A generalized Maxwell solid with two relaxation times is shown to rather well describe the indentation function except for the very first part of the relaxation ($t<0.1s$). A power law function for $G(t)$ gives a poorer agreement in this domain and furthermore is not able to represent the solid behavior at low frequency. A

tentative interpretation of this result in terms of the actin network was proposed even if it was beyond the scope of this chapter which was to give a firm basis for the determination of viscoelastic functions with the help of AFM. These results will also be used in Chapter 6.4 to predict the motion of magnetic nanoparticles actuated at the surface of the cell by a magnetic field with the aim to destroy the membranes of the cells. But before going to this issue we have to describe the particles we have used in this study.

5. SYNTHESIS OF MAGNETIC PARTICLES

In the last decades, many reports have been devoted to ferric oxide colloids and magnetic nanoparticles. Such particles commonly consist of magnetic elements such as iron, nickel and cobalt and their chemical compounds. These nano-objects are very attractive materials, which might found applications in several domains from microelectronics, catalysis, water treatment to diagnostic and therapy, as MRI-traceable drug carriers, cancer cell inhibitors or for tumor cell magnetolysis(65,66). In particular, special attention has been paid to the formulation of nanoparticles with different shapes and sizes.

In this chapter, we are going to discuss four kinds of magnetic nanoparticles, which have been studied in this work, the spindle-type Iron@Gold core-shell nanoparticles, the cobalt nanoneedles and two commercial particles: spherical iron particle and iron oxide particle.

5.1. Spindle-type Iron@Gold core-shell nanoparticles

5.1.1. Introduction

In this section, we report on the synthesis of a quasi-monodisperse population of acicular Fe@Au core@shell nanoparticles (Fe@Au NPs) produced by the reduction of spindle-type hematite nanoparticles and their subsequent gold plating through a transmetalation reaction.

One-dimensional nanostructures of hematite (α-Fe_2O_3) with different morphologies such as wire-like, rod-like and belt-like or two-dimensional spherical, elongated (spindle), micro-ring, or pseudo-cubic ones have been elaborated. They are produced by forced hydrolysis of ferric salts. In general, the growth of monocristalline α-Fe_2O_3 takes from a few days using hydrothermal techniques to one week under forced hydrolysis at 100°C(67). The anisotropic growth of hematite is generally controlled by the presence of different anions like phosphates, sulfates, oxalates or hydroxide ions.

Hematite is furthermore used as a raw material to produce metallic iron with high magnetic properties. The reduction of α-Fe_2O_3 to α-Fe (0) takes place at roughly 400 °C under a H_2 atmosphere. The main challenge in hematite reduction at high temperature is undoubtedly the

aggregation of particles, mainly provoked by the sintering phenomenon that occurs at the interfaces between particles. Furthermore, to prevent uncontrolled re-oxidation of iron, one needs to protect the particles' surface using mainly passivation techniques. The passivation of metal powders is typically done by growing an oxide layer over the particles' surface, covering its surface with a silica layer or with an inert metallic shell (gold, silver, platinum) creating core@shell structures(71–73). Passivation of the nanoparticles is also required for biocompatibility when in vivo biomedical applications are contemplated.

Due to their spindle-type morphology and gold passivation, magnetic Fe@Au NPs may have a tremendous potential for cancer therapy thanks to tumor cell magnetolysis process (52,53) provided that biocompatibility as well as selectivity could be tuned. Aiming at this goal, we have also functionalized their surface with polyethylene glycols (PEG), which facilitate their dispersion into biological media. We have thus used a fluorescently-labeled PEG thiol as a proof of concept as well as a model to facilitate the characterization of the nano-objects. It is nevertheless important to note that the surface labeling can be easily adapted for providing specific targeting of cancer cells by tethering ligands such as folic acid, RGD peptides or growth factor (e.g. VEGF) ligands at the PEG extremity in place of the fluorescent label. Although acicular Fe@Au nanoparticles have already been described in Chen's paper(66) this is, to our knowledge, the first report of the preparation of spindle-type Fe@Au core@shell nanoparticles driven by the displacement reaction of iron by gold without the need of any additional agent, i.e. reducing agents or microemulsion.

5.1.2. Experimental synthesis

- ***Chemical compositions***

Reactions were carried out under inert atmosphere using appropriate techniques. Iron(III) chloride hexahydrate ($FeCl_3 \bullet 6H_2O$), trichloroethylene (C_2HCl_3),1,2 dichlorobenzene (DCB), tetraoctylammonium bromide (TOAB) $[CH_3(CH_2)_7]_4NBr$, and auric acid ($HAuCl_4$) were supplied by Sigma-Aldrich. H_2N-PEG_{5000}-STrt (α-amino-ω-tritylthio-poly(ethylene glycol) Mw = 5.000 Dalton) was supplied by IRIS Biotech GMBH. Sodium phosphate monobasic (NaH_2PO_4) was supplied by Fluka. Ultra pure water 18.2MΩ.cm was obtained from a Thermo Scientific water purification device.

- ***Characterization techniques***

Structure and properties of iron and its passivation were characterized by transmission electron microscopy (TEM) on a TEM, JEOL JEM-1400 apparatus and by scanning electron microscopy on a SEM, FEI XL30 ESEM LaB6 device coupled to an energy dispersive analyzer (EDX, EDX Oxford/INCA). Surface modification of particles with the fluorescent polymer was analyzed with a Leica SPE confocal microscope using a 63x1.4 N.A. oil immersion objective. Hematite and iron powders (3~5%) were analyzed by diffuse reflectance infrared Fourier transform spectroscopy (DRIFTs, Spectrum BX, Perkin Elmer) mixed with KBr. Samples were directly placed in the cup and the background spectrum of KBr was subtracted. All reflectance spectra were taken at a resolution of 4 cm-1 for 16–64 scans from 4000 to 400 cm^{-1}. Magnetic properties of samples were investigated using a M2000/2100 hysteresis meter.

- ***Hematite spindle-type particle's synthesis***

The preparation of α-Fe_2O_3 particles was performed according to a method, which has been described elsewhere(74,75) and adapted for a larger scale (5-10g) synthesis. Briefly, 5.41g (0.02M) of $FeCl_3 \cdot 6H_2O$ and 0.054g (0.45mM) of NaH_2PO_4 were dissolved in 1 L of ultra pure water and kept undisturbed during 6 days at 100°C. Then, a filtration method to wash off sub-products (mainly salts) of hematite suspensions was applied. The filtration system allowed particles to be continuously washed without drying or concentrating particles. The filtration system was composed by a ceramic hollow membrane coupled with steel membrane housing. The particles' suspension was injected into this system, washed with ultra pure water until the suspension conductivity reached $10S.m^{-1}$ and finally freeze-dried. This filtration method, combined to freeze-drying procedure, prevented hematite from agglomeration and ensured the full dispersion of lyophilized nanoparticles.

By X-ray diffraction, as showed in Fig. 5-1, we can confirm that the synthesized particles are clearly hematite.

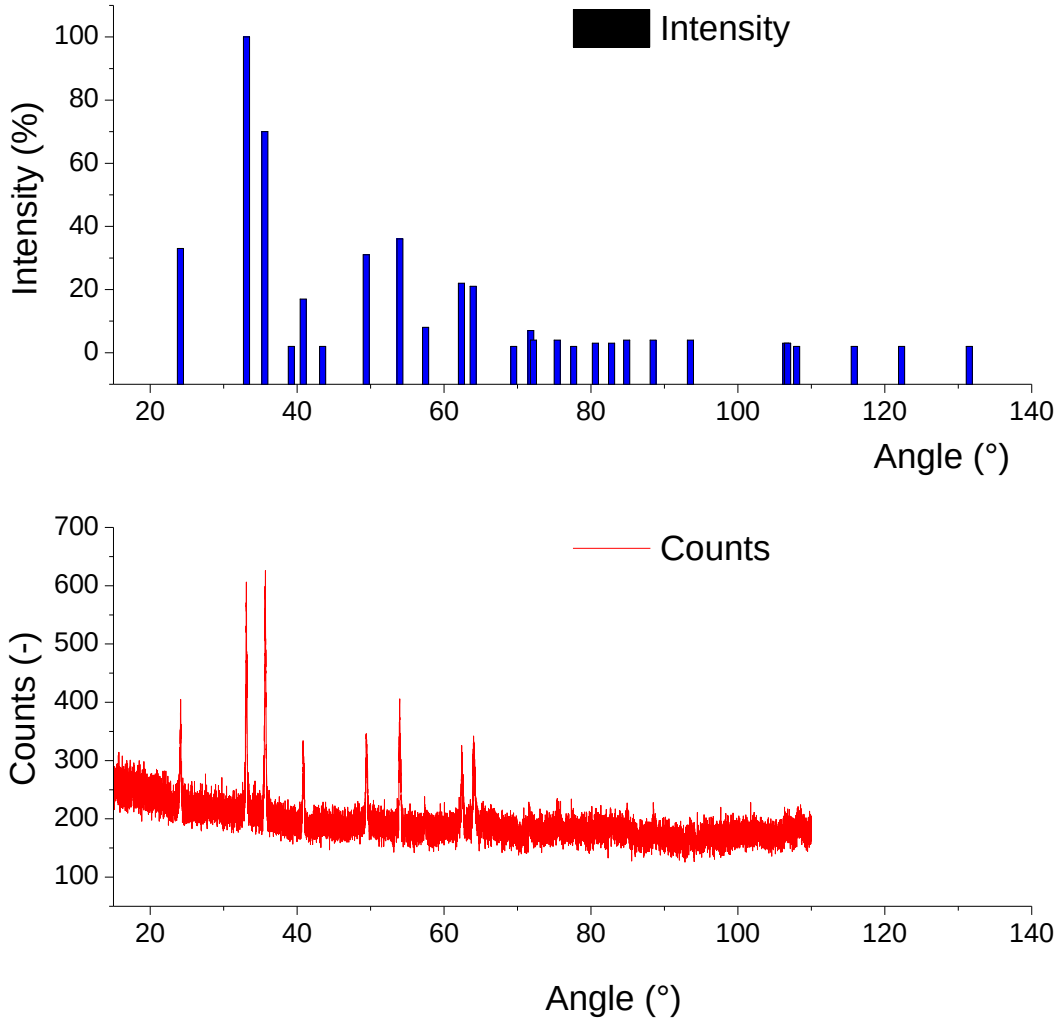

Fig. 5-1: Diffractogram of hematite particle, upper: theory, down: measured by XRD

- ***α-Fe(0) NPs' preparation***

The non-agglomerated hematite α-Fe_2O_3 powder (10g) obtained above was calcinated in a modified furnace chamber at 450°C under a continuous H_2 flow (0.5L.min^{-1}) during 4h. The temperatures were controlled by PID-controllers included in the tube furnace (Pirox). The vertical tube furnace was modified to introduce a vertical column support adapted to spread H_2 through the sample (Scheme 1). The home-made column support came from a modified Pirex Buchner filter funnel lengthen in bottom. The column incorporated a sintered silica distributor in bottom, and a quartz wool was placed on top to prevent the fluidized powder to escape from the column.

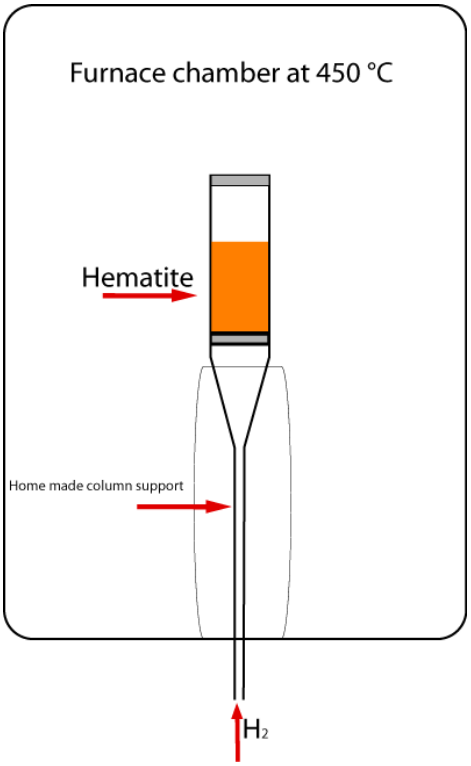

Fig. 5-2: Furnace scheme of α-Fe_2O_3 particles' reduction into α-Fe(0) NPs.

The whole particles turned from reddish to black indicating conversion of Fe(III) into Fe(0). After cooling under a N_2 stream, the column was pulled down and trichloroethylene (20 mL) was added under N_2 flow to avoid oxidation of the resulting α-Fe(0) NPs, which were kept into this solvent for further experiments. Very interestingly, it should be mentioned that no sintering was observed during this step.

5.1.3. Surface modification of iron particles

- ***Gold coating***

Gold coating of α-Fe(0) NPs was performed according to a procedure described elsewhere(76). First, hydrophobized gold (III) salt $[(C_8H_{17})_4N]+[AuCl_4]-$ were obtained from phase transfer after mixing solutions of TOAB in DCB and aqueous HAuCl4 with vigorous stirring. Basically, α-Fe(0) NPs (100 mg, 1.79 mmol), $[(C_8H_{17})_4N]+[AuCl_4]-$ (290 mg, 0.36 mmol) were dissolved into 20 mL of DCB under N_2 atmosphere and heated to 90 °C for 2 h while kept under inert atmosphere and maintained under vigorous mechanical stirring. Reaction was then quenched by adding 40 mL of absolute ethanol. Fe@Au NPs were

subjected to centrifugation/washing steps with absolute EtOH (five times). Finally, particles were suspended into absolute EtOH and kept under a N_2 atmosphere for further experiments.

- ***Surface modification of Fe@Au NPs***

500 µL of a Fe@Au NPs' stock suspension (10 mg/mL in absolute EtOH) were degassed. Then 500 µL of freshly made fluorescein-PEG5000-SH stock solution (10 mM in ultra pure water), which was previously degassed and filtered (0.22 µm, cellulose acetate), was added under N2. The resulting mixture was then stirred for 2h under N_2. Pegylated Fe@Au NPs were purified by several centrifugation /resuspension cycles into ultra pure water until the fluorescence signal of discarded water reached background level. Finally, fluorescein-PEG5000-labelled Fe@Au NPs were suspended into ultra pure water (1mL) and further analyzed by TEM and with a fluorescent confocal microscope to evidence functionalization.

Even if use the stronger reducer H_2, it is likely than pristine iron will be also partially oxidized into magnetite or maghemite, which bear a lower magnetic moment than α-Fe, but are nevertheless magnetic phases(77).

5.1.4. Results and discussion

- ***Morphology and structure of hematite and Fe NPs***

Hematite α-Fe_2O_3 and α-Fe(0) NPs resulting from the reduction process were analyzed by TEM and FT-IR. Particles' morphologies and sizes were evaluated throughout a series of TEM pictures. Fig. 5-3 displays a typical single particle of α-Fe_2O_3(A) and α-Fe(0) NPs (B). One can observe that the particles' shape is kept constant during the whole process of reduction of the oxide into a metal phase. The average sizes measured from the TEM pictures were of 580 (±50) nm in the major axis and of 80 (±5) nm in the minor axis.

Fig. 5-3 presents also the FT-IR spectrum of both hematite and iron. Hematite exhibits three absorption bands at 577, 538 and 487 cm^{-1} that are typical vibration bands corresponding to the perpendicular and parallel modes of the Fe-O bound(78).

Peaks at 1037, 1002 and 968cm^{-1} correspond to phosphate residues introduced during the synthesis of the particles. The dominant absorption band of hematite (538cm^{-1}) is shifted to

563 cm^{-1} in the iron spectrum, this is probably due to a partial reduction of the oxide producing defects or dislocations in the internal structure of iron particles(79). That residual oxide phases as a result of partial reduction are present within the α-Fe(0) NPs seems further to be supported by the lower density (ρ_p), i.e. 5.3 ± 0.1g cm^{-3}, determined experimentally for the α-Fe NPs as compared to the literature density value reported for bulk iron (ρ_{bulk} =7.86g.cm^{-3})(80).

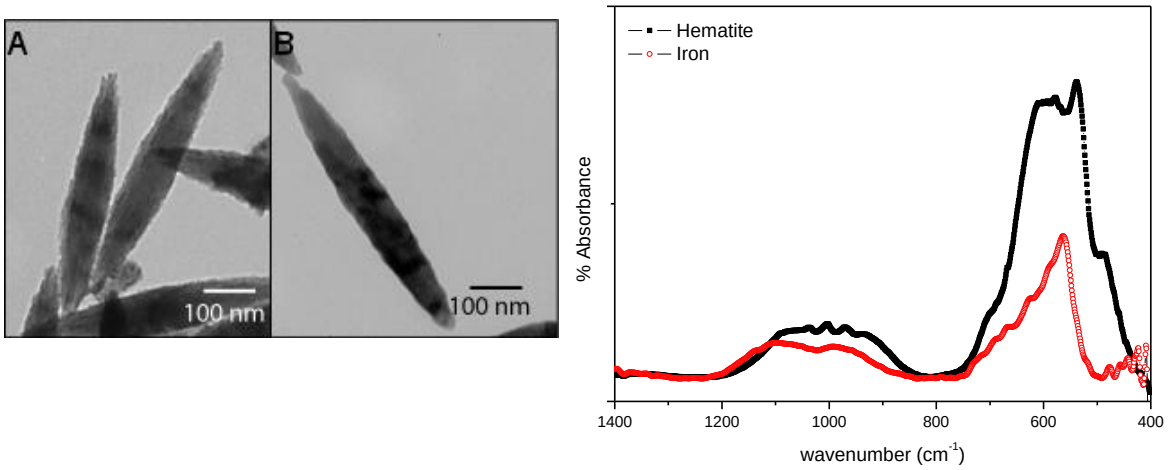

Fig. 5-3: TEM pictures of (A) α-Fe_2O_3 and (B) α-Fe(0) NPs. (C) IR spectrum of α-Fe_2O_3 (black line) and α-Fe(0) NPs (red line)

The presence of such phases is also corroborated by TEM pictures where pores and rough surfaces can be seen, and by the magnetization measurements, since the magnetization saturation was 156 emu/g instead of 220 emu/g for pure iron.

- ***Synthesis and composition of Fe@Au NPs***

Fig. 5-4 and its inset picture shows the EDX spectrum and a typical SEM image of the gold-coated acicular Fe@Au NPs, respectively. They were obtained from the acicular Fe NPs, which were coated with metallic gold as a result of a gentle redox transmetalation between surface Fe atoms of α-Fe(0) NPs and Au(III) ions of $[(C_8H_{17})_4N]^+[AuCl_4]^-$ in an non aqueous solvent. The resulting acicular Fe@Au NPs were observed by TEM analysis, and found to have an average length and diameter very similar to those of their starting α-Fe(0) NPs. Such a smooth reaction process, where shell layer formation and core metal consumption occur simultaneously, preserves the average particle sizes of the original Fe NPs. The EDX pattern exhibits important peaks for Fe and O and a weak signal for Au. The weak gold signal is due

to the thin gold coating shell (see next section). The presence of oxygen into the EDX pattern corroborates the FT-IR spectrum of the iron particles where we have observed residual Fe-O vibrations (see above section).

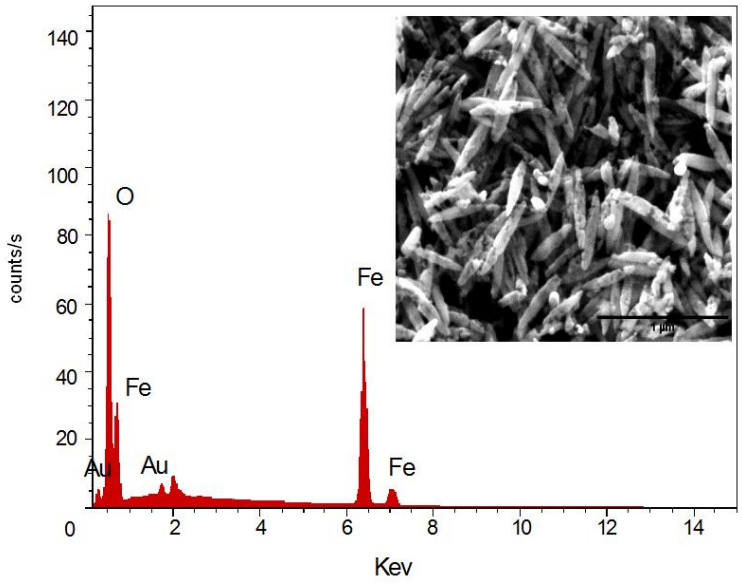

Fig. 5-4: EDX spectrum of Fe@Au NPs, inset SEM image of acicular Fe@Au NPs

- ***Magnetic properties of Fe and Fe@Au NPs***

Powders of acicular Fe and core@shell Fe@Au NPs were analyzed by magnetization hysteresis loops at room temperature as presented in Fig. 5-5,and Tab. 5-1 which gives the saturation magnetization (M_s), remanent magnetization (M_r), coercivity (H_c) and squareness ($S_r = M_r/M_s$) data determined from these curves.

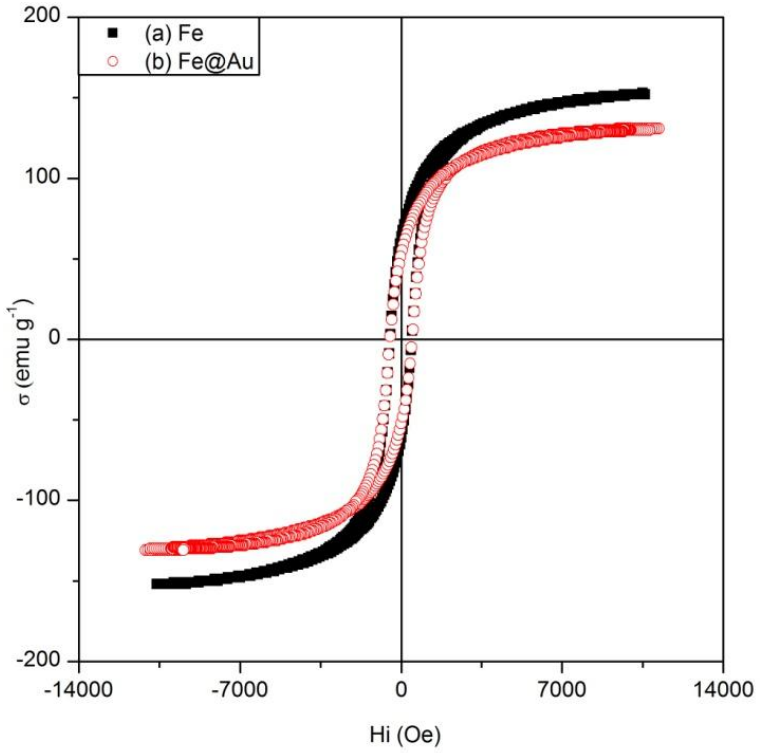

Fig. 5-5: (a) Magnetization curve of α-Fe, (black squared dots) (b) Magnetization curve of Fe@Au, (red triangular dots)

	H_c (Oe)	M_s (emu g^{-1})	M_r (emu g^{-1})	S_r
Uncoated acicular Fe	294	156	52.6	0.224
gold-coated acicular Fe@Au	485	131	34.9	0.401

Tab. 5-1: Magnetic properties of Fe and Fe@Au NPs determined from hysteresis loops

Particular attention has been paid to the saturation magnetization (M_s) parameter, which is defined as the maximum of the magnetization value achieved in a sufficient large magnetic field. Table 1 shows that the saturation magnetization of acicular gold-coated Fe@Au NPs ($M_s^{Fe@Au}$) is less than the value determined for acicular α-Fe NPs' powder (M_s^{Fe}), as expected owing to the non magnetic gold shell constituting the Fe@Au NPs. However, both these M_s^{Fe} and $M_s^{Fe@Au}$ values are lower than the M_s^{bulk} values reported for bulk iron (M_s^{bulk} = 222 emu/g). These differences are most likely related to the presence of residual oxide phases within the α-Fe and Fe@Au NPs, as attested above by FT-IR and EDX pattern and as also reported in literature for other iron nanoparticles(75).

- ***α-Fe and Fe@Au NPs magnetization and gold shell thickness***

Using the saturation magnetization M_s values, one can calculate the magnetic and non magnetic part in a single α-Fe NPs and furthermore deduce the thickness of the gold shell in the Fe@Au NPs. The magnetic moment, **m**, of a particle *p* is given by:

$$\mathrm{m} = V_p \cdot M_s^p \cdot \rho_p \qquad (5.1)$$

Where V_p is the volume of the particle, ρ_p its density and M_s^p its saturation magnetization, or by:

$$\mathrm{m} = V_{Fe} \cdot M_s^{Fe} \cdot \rho_{Fe} \qquad (5.2)$$

Where V_{Fe} is the volume of iron inside the particle, ρ_{Fe} the iron density and M_s^{Fe} the saturation magnetization of iron,so we get:

$$\frac{V_{Fe}}{V_p} = \frac{\rho_p \cdot M_s^p}{\rho_{Fe} \cdot M_s^{Fe}} \qquad (5.3)$$

Applying this equation to the data measured on the α-Fe NPs (Tab. 5-1 for the M_s values) and to the densities found(80) for ρ_p=5.3±0.1g.cm^{-3} and ρ_{Fe} =7.86g.cm^{-3}, one obtains:

$$V_{Fe} = 0.47 V_p \qquad (5.4)$$

This indicates that 47 % in volume (70 % in mass) of the α-Fe NPs is magnetic, the other non magnetic part being either voids or non reduced hematite.

For the calculation of the gold shell thickness, *e*, covering the acicular Fe@Au NPs, one can assume that *e* is related to the volume increment *dV/V* of the ellipsoidal particles, which is the total differential of the volume of an ellipsoid:

$$V = \frac{4\pi}{3} a^2 b \qquad (5.5)$$

As

$$\frac{dV_p}{V_p} = 2\frac{da}{a} + \frac{db}{b} \tag{5.6}$$

Assuming that the thickness *e* of the gold layer is homogeneous in both *a* and *b* axes of the ellipsoid ($da = db = e$), then the thickness of the gold layer is given by:

$$e = \frac{ab}{a+2b} \cdot \frac{dV}{V} \tag{5.7}$$

Concerning the volume increment *dV/V*, this parameter can be calculated from the magnetization of iron for Fe NPs (Eq.(5.8)) and of Fe@Au for core@shell NPs (Eq.(5.9)):

$$M_s^{Fe} \propto \frac{N_{Fe}}{m_{Fe}} \tag{5.8}$$

$$M_s^{Fe@Au} \propto \frac{N^*_{Fe}}{m_{Fe@Au}} \tag{5.9}$$

where (i) M_s^{Fe} and $M_s^{Fe@Au}$, (ii) N_{Fe} and N^*_{Fe} and (iii) m_{Fe} and $m_{Fe@Au}$ are the saturation magnetization, the number of Fe atoms, and the mass of one single Fe and Fe@Au particle, respectively.

Taking into account that the stoechiometry of the Fe/Au displacement reaction at the surface of the Fe particle is of 1:1 (any single Fe(0) atom at the surface is oxidized into Fe(III) and is replaced by a single Au(0) atom resulting from the reduction of one Au(III) present in the solution), this indicates that N'_{Fe} is equal to N_{Fe}-N_{Au}, where N_{Au} is the number of Au atoms forming the coating of one Fe@Au particle. This exchange reaction, which concerns almost exclusively the first outer layer of Fe atoms in contact with the Au(III) solution has furthermore no consequences onto the geometrical parameters (*a*, *b* and *V*) of the ellipsoid. One can assume therefore that:

Since the gold does not change the magnetic moment of a particle, one has the equality:

$$(m_p + m_{Au}) \cdot M_{Fe@Au} = m_p \cdot M_p \tag{5.10}$$

We have, $m_{Au}/m_p = (156-131)/131 \approx 0.19$, taking 19.3 g cm^{-3} for the density of gold and 5.3 g cm^{-3} for the core of the particles the ratio of the volumes is $V_{Au}/V_p = 5.2\%$.

This is in the hypothesis where the gold is deposited on the iron, but if, as claimed in Mandal's acticle(81), there is a substitution between iron atom and gold atom, then we obtain approximately:

$$\frac{m_{Au}}{m_p} = \frac{M_p - M_{Fe@Au}}{M_p}\left(\frac{1}{(M_{Fe@Au}/M_p).(1-r_a)+r_a/r_{Fe}}\right) \tag{5.11}$$

Where r_a=0.283 is the ratio of the atomic mass of iron by the one of gold and from Eq.(5.4), we have:

$$r_{Fe} = \frac{m_{Fe}}{m_p} = 0.7 \tag{5.12}$$

We suppose that:

$$R_M = \frac{M_{Fe@Au}}{M_p} \tag{5.13}$$

Then Eq.(5.11) can simplify as:

$$\frac{m_{Au}}{m_p} = \frac{1-R_M}{R_M(1-r_a)+R_M r_{Fe} r_a} \tag{5.14}$$

This equation predicts that m_{Au}/m_p = 16.6% which is quite close from the estimation of 19% in the first hypothesis. The volume fraction of gold being now: V_{Au}/V_p= 4.55%. For an ellipsoidal shape we obtain from Eq.(5.7), with *a*=80nm and *b*=580nm, e=1.6nm that is to say about ten atomic layers.

5.1.5. Synthesis of pegylated Fe@Au NPs and characterization

By taking advantage of the high Au-S affinity, the gold surface of Fe@Au NPs was stained through chemisorptions with fluorescein-PEG_{5000}-SH. The resulting particles were examined by TEM, which indicated that no modification of the original Fe@Au NPs had occurred. Surface gold staining with the fluorescent dye was attested by confocal microscopy. Fig. 5-6 shows a 3D-picture constructed with ImageJ recorded from a Z-stack of 28 different views

(longitudinal sections on the Z-axis) with the green emission mode (λ_{em}=520nm, λ_{ex}=490nm). It should be noted that an additional red emission mode (with λ_{em}=620nm, λ_{ex}=590nm) was also tested as negative control (data not shown). This latter, as expected, could not result into any red light emission. Green staining is only located at the surface of nanoparticles and clearly evidences their acicular shape. This experiment undoubtedly shows that Fe@Au NPs have been functionalized with the fluorescently-labeled PEG. It indicates also that PEG can provide dispersion of the Fe@AuNPs into aqueous solution by creating a steric and hydrophilic shield, and that this strategy can be applied to functionalize the surface of Fe@Au NPs for specific cell recognition by tethering a suitable ligand at the PEG extremity.

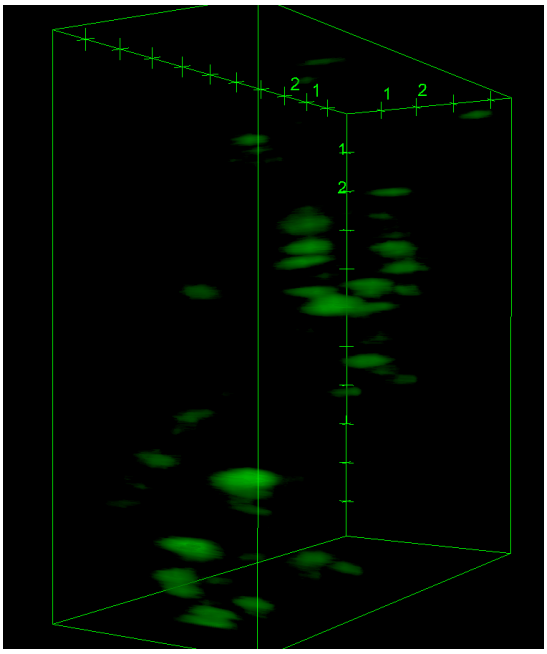

Fig. 5-6: Confocal microscopy 3D-picture of Fe@Au-S-PEG$_{5000}$-Fluorescein NPs in emission mode (green channel). The bounding box displays xyz coordinate system as well as units (scale in µm).

5.2. Cobalt nanofibers

We also synthesized the cobalt nanowires, which will be used in the hyperthermia experiments by using the method of polyol(82). The polyols are used because of their polarity, high capacity for reduction and high boiling temperature. Here we have used the 1-2 butanediol. The ruthenium acts as a nucleation agent. The synthesis procedure is the following:

5.2.1. Polyol method

The principle of synthesis is as followed(83):

- ***Nucleation by adding ruthenium (by heating)***

$$RuCl_3 \rightarrow Ru°$$

- ***Solvation***

$$\text{Co laurate} + NaOH \rightarrow Co(OH)_2 + \text{Na laurate}$$

- ***Thermal decomposition of butanediol***

$$CH_3 - CH_2 - CH(OH) - (CH_2OH) \rightarrow CH_3 - CH_2 - CH_2 - CHO + H_2O$$

- ***Reduction of cobalt***

$$2(CH_3 - CH_2 - CH_2 - CHO) + Co(OH)_2 \rightarrow (CH_3 - CH_2 - CH_2 - CO)_2 + 2H_2O + Co$$

5.2.2. Description of synthesis and results

Before the synthesis, we need to prepare the cobalt laurate. We dissolved 6g of sodium laurate in 15ml of distilled water by heating at 60-70°C. Then we add drop to drop a solution of $CoCl_2$ with a little excess of $CoCl_2$ compared to stochoiemetry to be sure to turn all the sodium laurate into cobalt laurate (it is easier to eliminate the excess $CoCl_2$ than sodium laurate by rinsing).

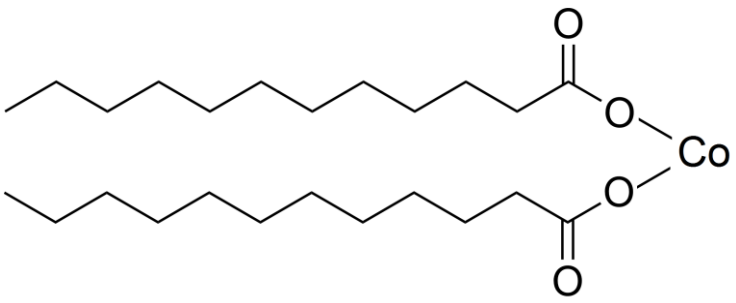

Fig. 5-7: Cobalt laurate

Then the precipitate of cobalt laurate is rinsed in ethanol until it is clear, and dried in a desiccator containing a cup of P_2O_5 to accelerate the drying. The drying process can take several days, but rinsing with ethanol is expected to decrease it; the final powder should be dark purple.

The synthesis procedure is now the following:

We dissolved 0.59g of NaOH in 100ml of 1, 2-butanediol in a two-neck flask, and 0.077g of RuCl3 in 30ml of 1, 2-butanediol in another two-neck flask, under magnetic stirring and N_2 atmosphere.

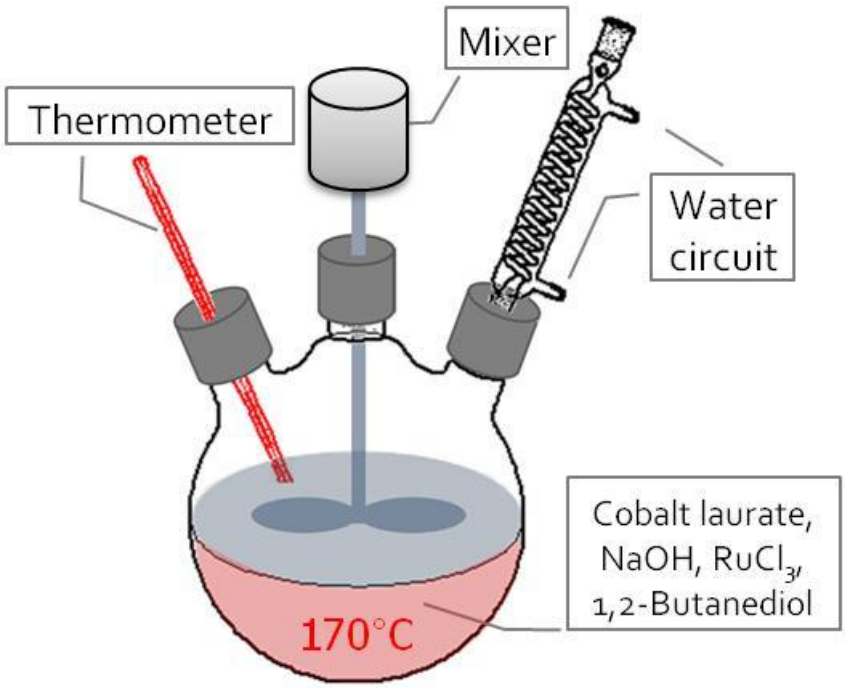

Fig. 5-8: Experimental setup for the synthesis of cobalt nanoparticles

As represented in Fig. 5-8, a three-neck flask is used for synthesis. We added 7.3 g of cobalt laurate in 70ml of 1, 2-butanediol. Before putting the powder in the flask, we must disaggregate it with a spatula; and then use the paddle blade for mixing.

Then we add the solution of NaOH and ruthenium chloride and degass the mixture during ¼ hour, under a stream of nitrogen. After that, the mixture was heated at 170 ° C with a heating ramp of 7° C/min (by using a PID controller, the parameters being: P = 1.7, I = 0.20, D=56) and then the temperature was maintained at 170°C during 30mn. Once the reaction is completed, we let it cool, and then rinse with DCB by alternating centrifugation and

ultrasound, until the filtrate is clear. We add a known volume of DCB at the end, so we can disperse and keep it in DCB at a known volume fraction.

The cobalt nanofibers are then observed in transmission electron microscopy (TEM). We see in the Fig. 5-9 that the diameter of the cobalt nanofibers is only about 10nm and their length about one hundred nanometers. Actually the length and shapes are very sensitive to the conditions of synthesis, in particular to the initial temperature ramp, and they must be verified after each new synthesis.

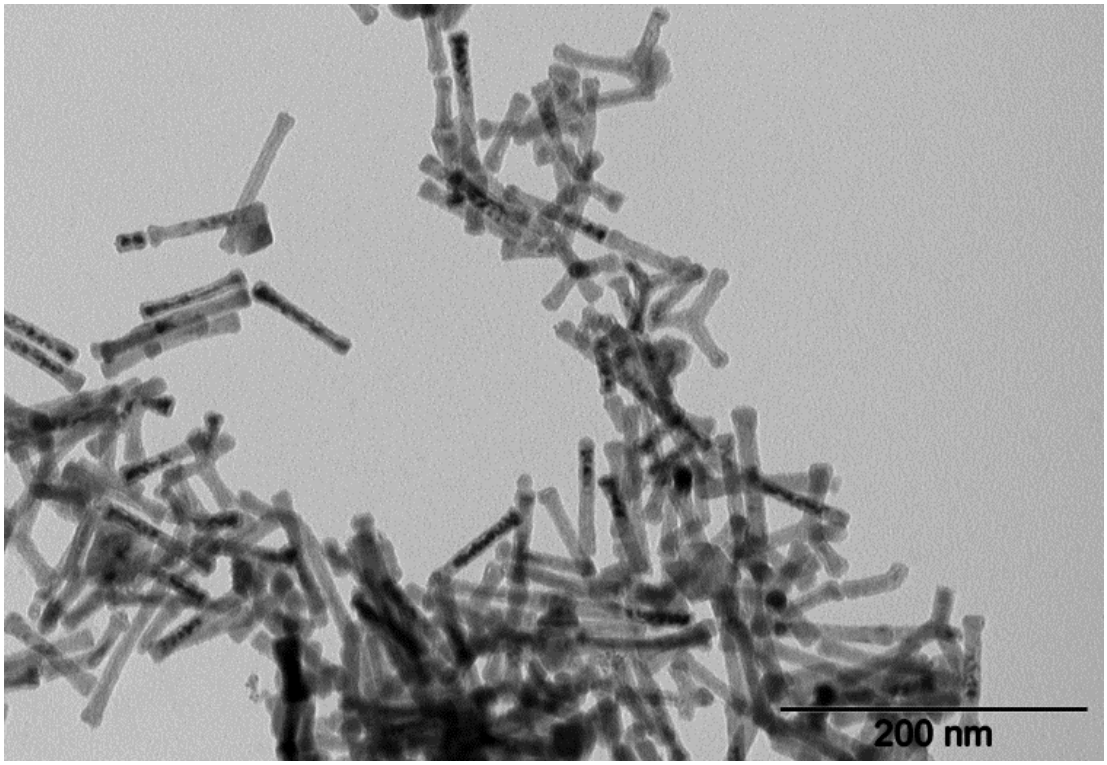

Fig. 5-9: The TEM image of Cobalt nanowires.

These particles present a quite strong hysteresis loop as we can see in Fig. 5-10:

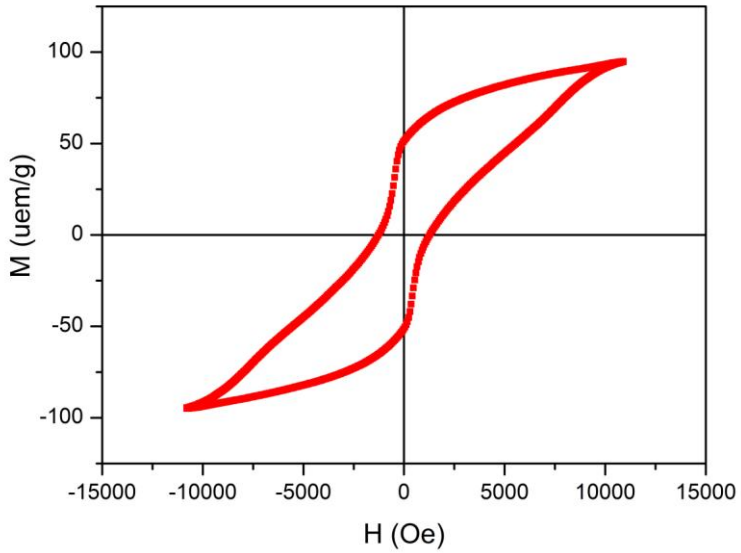

Fig. 5-10 magnetisation cycle of cobalt nanoparticles; H is in Oersted

This feature is important for hyperthermia applications as we shall see in chapter 7. The magnetization M=100 uem/g (890kA/m) a field of 10 000 Oe is still not saturated but clearly well below the magnetization saturation of cobalt M_s=1420 kA/m. This indicates the presence of surface defects or of surface oxidation, which can decrease the magnetization of the nanoparticles.

5.3. Iron and iron oxide particles

5.3.1. Iron particles

Beside these spindle-type particles we have also used commercial carbonyl iron powders (BASF, Germany). They are spherical ferromagnetic particles with diameters from several hundred of nm to 1.5 µm, as showed in Fig. 5-11.

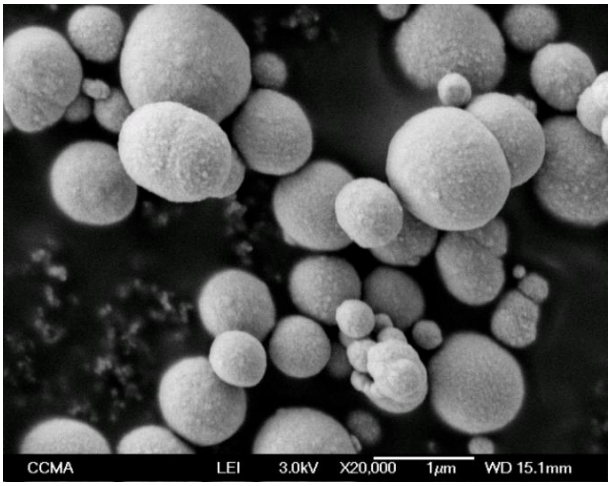

Fig. 5-11 : the SEM images of BASF particles

Their surfaces have been treated by aminosilane to avoid their oxidation in water. The surface treatment is the following: The iron powder is first heated in trichloroethylene under reflux during 4-6h and then rinsed with ethanol in order to remove oxide layer. The silane (here 3-aminopropyltriethoxysilane) is hydrolysed by mixing it (2-5% v/v) during 15 mn with an acidic solution of ethanol containing 5% of water and brought to pH 5 with acetic acid. Then the iron powder is added to this solution containing silanol groups and let on an oscillating table during one night.

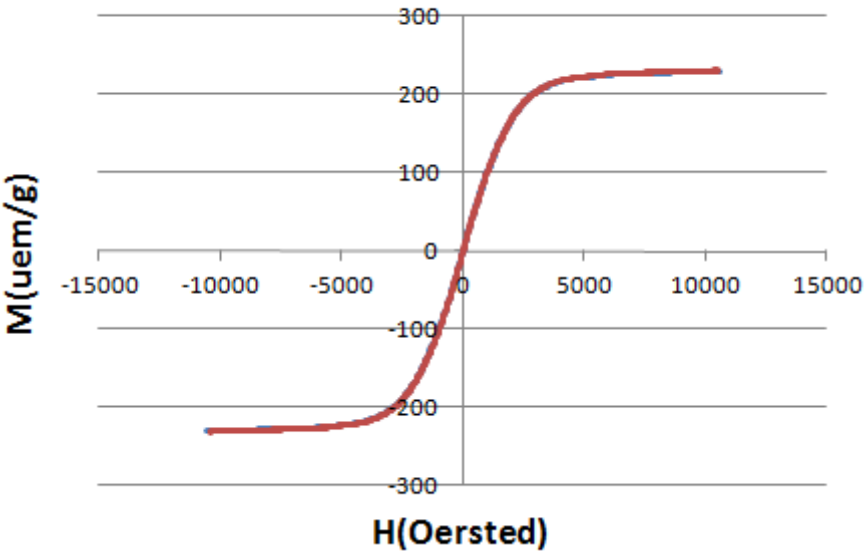

Fig. 5-12 Magnetization curve of BASF particles (HQ grade)

Contrary to cobalt nanofibers which present a large hysteresis loop, these particles do not present hysteresis at all (cf Fig. 5-12) and their saturation magnetization Ms=220 uem/g well corresponds to the saturation magnetization of the bulk iron.

5.3.2. Iron oxide particles

We also used the commercial iron oxide particle (Mapico Color / Columbian Carbon Company, NY), for the hyperthermia experiments. Their shape is very irregular and their sizes range from one micron to a few ten on nm as can be seen on electron microscopy images (cf Fig. 5-13). Their magnetic properties will be presented in chapter 7, Fig. 7-5.

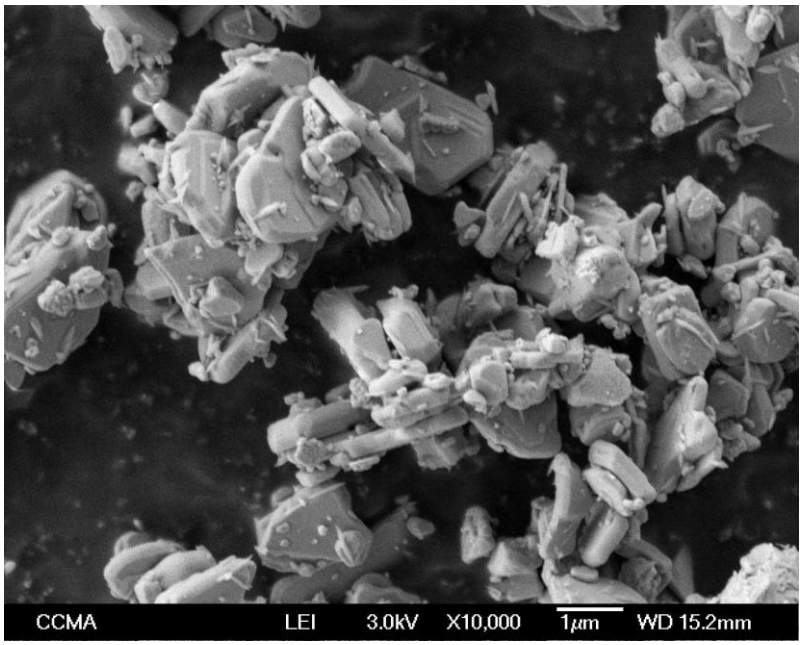

Fig. 5-13: SEM view of iron oxide particles

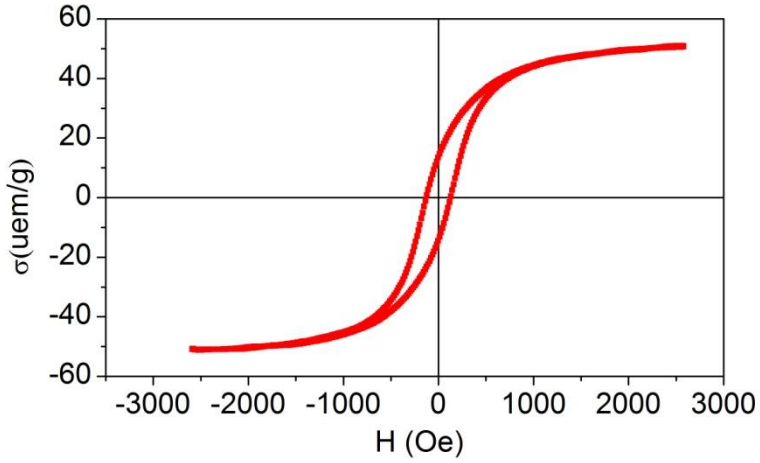

Fig. 5-14: Magnetization curve of iron oxide particles

5.4. Conclusions

In this chapter, we demonstrated the feasibility to obtain highly disperse spindle-type hematite NPs and to reduce these acicular NPs into acicular metallic iron NPs under a H_2 flow at 450°C without sintering. By using a redox transmetalation process, the Fe core serves as a nanoelectrode for the spontaneous deposition of gold onto the NPs' surface without the need of any additional agents. From the comparison of the saturation magnetizations, a thickness of the gold layer of about 1.6nm was deduced. The gold surface of the Fe@Au NPs was also functionalized with stained PEG thiol conjugates thus allowing dispersion of the Fe@AuNPs into aqueous solution. Interestingly, the magnetic properties of Fe@Au NPs were only slightly lowered by the presence of the gold shell when compared to non passivated α-Fe NPs. Concerning cobalt nanoparticles, by adapting the parameters like the temperature ramp and the concentration of NaOH we have obtained nanofibers with a length (about 100nm) and a diameter (about 10nm) which make them interesting for biological applications, especially in hyperthermia ones. The coverage of the cobalt by a gold layer as for iron particles is underway.

6. MECHANICAL DAMAGE INDUCED BY AN ALTERNATING MAGNETIC FIELD

6.1. Introduction

Magnetic particles (MPs) are extensively used in biological assays, mainly due to the possibility to separate them from a culture medium by using a simple magnet. If their surface is functionalized to capture a given molecule, it allows to detect this molecule and to concentrate it easily (84). For such applications, the size of the particles is around 1 µm in order to generate a high enough magnetic moment, this being proportional to the volume of the particles and, therefore, to obtain optimum magnetic separation.

MPs are also used as platforms for numerous biomedical applications including diagnostics by magnetic resonance imaging(MRI) (85), magnetically targeted drug delivery and/or cancer therapy by hyperthermia (86). For these last applications, the particles are heated by applying an alternative magnetic field and the increase of heat contributes to destroy tumor cells (87) or to expel the cargo drug molecules (88). The size of the magnetic nanoparticles, which are used for hyperthermia is quite small (about 10 nm) allowing their magnetic moment to fluctuate with a relaxation time of 10-5 to 10-6s order and thus to present an optimum frequency, high enough for energy dissipation in an alternative field. However, the force, which can be induced by the gradient of an external magnetic field, is very low and is not sufficient to retain the particles in the vicinity of the tumor (89). On the other hand, such small nanoparticles are quite easily taken up by cells through a clathrin-mediated endocytosis pathway (the limiting size of this process is around 200 nm) (90). In some cases, their internalization can strongly reduce the proliferation of cancer cells (91,92). Particles in the 300-600 nm range can also be used for the embolization of tumor vasculature to necrotize tumor tissue (93).

Concerning cell lysis and tumor treatment, most of the research with MPs is focused on hyperthermia techniques with high frequency alternative magnetic field. However a few recent works have shown that tumor cells can be destroyed, both in vitro and in vivo, by the

application of a low frequency magnetic field on micronic or submicronic magnetic particles. For instance, the use of micronic iron particles injected in breast tumors of mice, when submitted to a strong permanent magnetic field (0.4T), resulted in tumor destruction (94). Nevertheless this result was obtained with a very concentrated suspension (60 % in weight) injected directly into the tumor. The other papers addressed the in vitro study of cancer cells with different kinds of field-responsive particles used at much lower volume fractions. In one of these reports, magnetic disks of 1 µm diameter and 60 nm thickness, when actuated by a magnetic field of 10-20 Hz frequency and about 90 Oe amplitude during 10 min, caused cell death (52). As the estimated amplitude of penetration of the particles inside the membrane due to the magnetic torque was quite low, the authors concluded that cell death was not the result of cell membrane damage but, instead, of the triggering of intracellular pathways activating programmed cell death (apoptosis), caused by the alternative low frequency motion. In another study, smaller organic particles with a diameter around 200 nm, containing magnetic nanoparticles of 5 nm diameter embedded into the polystyrene matrix were used (53). Due to phase separation during the embedding step, the magnetic nanoparticles were aggregated only on one side (pole) of the resulting organic particles. Here too, when submitted to a rotating field at a frequency of 50 rpm and after 15 min exposure to the spinning magnetic field, the majority of the tumor cells were killed as evidenced by trypan blue staining. The rapidity of the staining by the trypan blue indicated further that cell destruction was related to membrane damage and not to apoptosis.

Very recently, multiwall carbon nanotubes containing iron impurities making them paramagnetic when placed into a rotating field of amplitude above 40 mT during 20 min, were reported to induce a significant decrease of cell viability (95).

All these studies demonstrated a magnetolysis effect but only for some special experimental parameters, which are related to the type of magnetic particles and the conditions of application of the magnetic field. Nevertheless the explanation of the phenomenon remained qualitative and somewhat contradictory between direct damage caused to the membrane of the cells and apoptosis indirectly triggered by the application of a mechanical solicitation. The goals of the work reported here were (i) to confirm that, using anisotropic MPs, moderate magnetic fields can be sufficient to destroy cancer cells at low frequency, and (ii) to bring new insight in the in vitro magnetolysis process of cells in culture. Aiming at these goals, we have used two different kinds of MPs (spindle or spherical) in conjunction with a well

controlled magnetic field gradient (alternative or constant) allowing to calculate precisely the applied force. The resulting penetration into the cell by the different types of MPs (spindle or spherical morphology, size) was derived from the knowledge of the mechanical response function of the cell obtained from experiments made by atomic force microscopy (AFM). This model was used to explain how the MPs can mechanically cause cell damage. Furthermore, direct indentation of the cells by an AFM tip was used to confirm our hypothesis on the intensity of forces necessary to damage the cells, and also to determine the best conditions to obtain magnetolysis with MPs.

6.2. Materials and methods

The cancer cell which has been studied is called Hep G_2 see chapter 4.2.1, and two types of magnetic particles for our experiences, the spindle-type and spherical-type, presented in chapter 5.1 and 5.3.

The magnetic moment *m* of one particle is given by:

$$\mathrm{m} = \mu_0 V_p M \tag{6.1}$$

Where μ_0 is the magnetic permeability of vacuum constant and *M*, the magnetization is given by:

$$M = \chi(H) H \tag{6.2}$$

Where $\chi(H)$ the magnetic permeability and *H* is the field inside the particles, it can be written as a function of the applied magnetic field H_0:

$$H = H_0 - nM \tag{6.3}$$

Where *n* is the demagnetization factor, with *n=1/3* for a spherical particle and *n=0* for a needle(96); for an ellipsoid(97) of aspect ratio of 8 we have $n \approx 0$, so we shall take $H=H_0$.

For a field lower than 2000*Oe* which is the maximum field acting on the particles, we can approximate the magnetization curve by a linear curve of slope $\chi = 5.0$. For a spherical particle, the field *H* is smaller than the applied field due to the demagnetization factor, so one can calculate it, by Eq.(6.2) and Eq.(6.3), we have :

$$H = \frac{3H_0}{3+\chi(H)} \tag{6.4}$$

If $\chi(H) \gg 1$, which is true at low field then we can use:

$$M = \frac{3\chi(H)H_0}{3+\chi(H)} \simeq 3H_0 \tag{6.5}$$

So we can take $\chi = 3$ for a spherical particle.

6.2.1. Experimental Setup

The experimental setup consisted of a non-magnetic plate tightly fixed above a modal exciter (Brüel & Kjær type 4824, Nærum, Denmark) by 3 rods, as shown in Fig. 6-2, the 35 mm Petri dish (BD, Franklin Lakes, NJ) containing the cancer cells was fixed inside a cylinder, which is screwed inside a hole at the center of the plate and can be moved vertically. A 58 mm diameter neodymium magnet was stuck on the top of the exciter, right under the plate, coaxially.

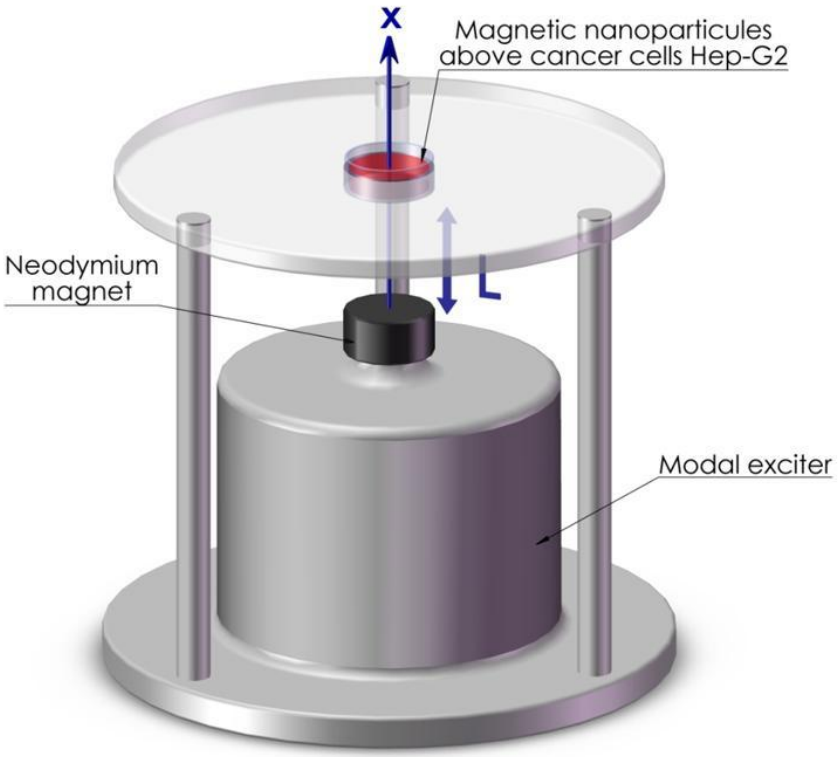

Fig. 6-1: Experimental setup

The exciter is controlled by a sinusoidal signal-through a dedicated amplifier. The magnet can easily vibrate at full amplitude from 0 to 10 Hz and the amplitude of vibration was adjusted in such a way that the magnet almost touches the dish bottom at its upper point.

The determination of the magnetic field of this setup is straightforward: first of all, we measured the magnetic field of the neodymium magnet in function of the distance x, the result is shown in the upper part of Fig. 6-2; these data can be quite well fitted by a linear function, so we approximate the magnetic gradient fields ∇H_x as:

$$\nabla H_x = \frac{H_{\max} - H_{\min}}{L} = \frac{\Delta H}{L} \tag{6.6}$$

Since the vibration is sinusoidal in the direction of x, the motion of the magnet as a function of time is:

$$x = x_0 + \frac{L}{2}\left(1 + \sin \omega t\right) \tag{6.7}$$

Where L is the amplitude of the sinusoidal motion, and x0 is the initial position of the magnet, and ω is the angular frequency.

So the magnetic field created by the magnet is:

$$H = H_{\min} + \frac{\Delta H}{2}\left(1 + \sin \omega t\right) \tag{6.8}$$

Where $H_{\min}$ is the magnetic field in the Petri dish when the magnet is at x_0, and Hmax is the magnetic field in the Petri dish when the magnet is at x_0+L.

This function is showed in the lower part of Fig. 6-2.

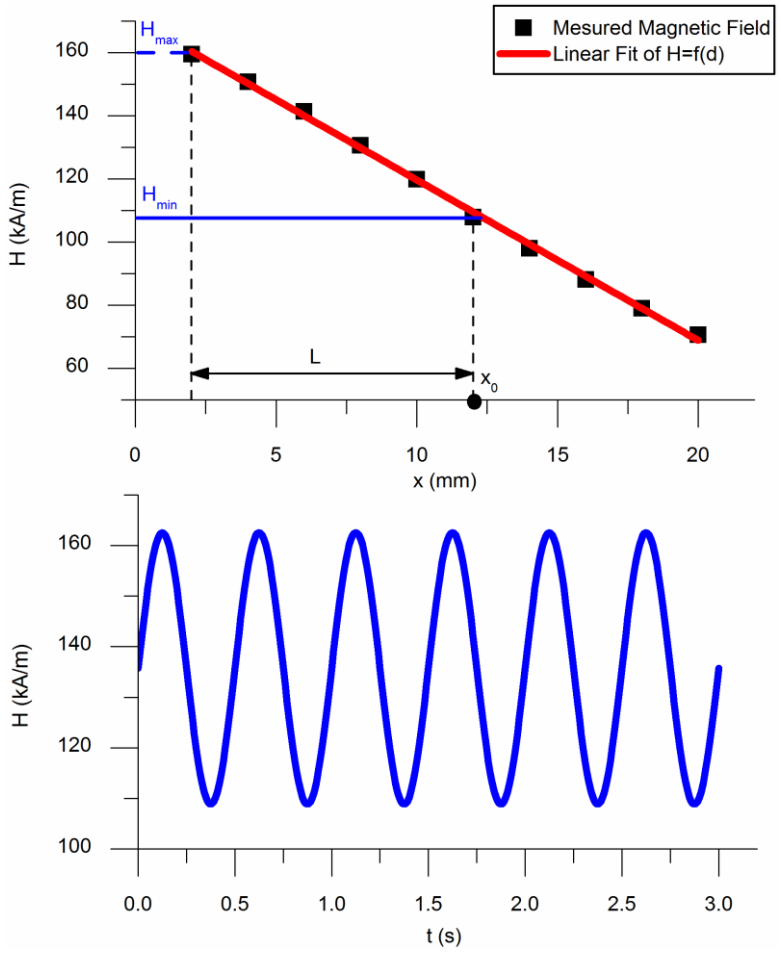

Fig. 6-2: Upper graph: Measurement of magnetic field vs. distance between magnet and cells. Lower graph: magnetic field vs. time for a frequency of 2Hz)

The applied magnetic force on a particle is given by:

$$F_H(t) = \mu_0 \chi V_p H(t) \nabla H_x \tag{6.9}$$

V_p is the volume of the particles.

From Eqs.(6.6), (6.8) and.(6.9), we have:

$$F_H(t) = \mu_0 \chi V_p \frac{\Delta H}{L}\left[H_{\min} + \frac{\Delta H}{2}(1+\sin \omega t)\right] \tag{6.10}$$

Or in a more condensed way:

$$F_H(t) = C_0 + C_1 \sin \omega t \tag{6.11}$$

Where

$$C_0 = \mu_0 \chi V_p \frac{\Delta H}{L}\left[H_{\min} + \frac{\Delta H}{2} \right] \text{and } C_1 = \mu_0 \chi V_p \frac{\Delta H^2}{2L}$$

So we can calculate the magnetic force.

6.3. Results

6.3.1. Mortality rate

A suspension of magnetic nanoparticles was made by mixing the magnetic nanoparticles with the culture medium. This suspension with a known volume of culture medium and of particles was put into the Petri dish containing the cells, and then kept at 37°C in the incubator for 4 hours. During this time the magnetic nanoparticles sediment on the cells surface, and likely adhere to the cell surface. Then the Petri dish is placed above the vibrating magnet during a given period of time. During the same time a reference Petri dish with the same content of cells and magnetic particles were just placed in contact with another identical magnet. After the experiment, the two Petri dishes were put in the incubator for 30 minutes, and then the culture medium with most of the particles were removed to get a better vision under optical microscopy, and some 200 μl of culture medium are added to supply the live cell.

The mortality of HepG2 cells has been measured by the trypan blue assay. The reactivity of trypan blue is based on the fact that the chromophore is negatively charged and enters into the cell only when the membrane is damaged (98).

Each Petri dish, prepared as mentioned in section Materials and Methods and containing medium, adherent HepG2 cells with spherical or acicular MPs, was placed above the vibrating magnet during a given period of time (20, 40 or 60 min). During the same time, a reference dish with the same content of materials, i.e. medium, cells and MPs but not subjected to the magnetic field was used as a blank. At the end of this experiment, all Petri dishes were put in the incubator for additional 30 min. Then, the different dishes were treated as mentioned in section Materials and Methods and stained for the trypan blue assay. The results of the mortality (expressed as a mortality ratio, i.e. number of died cells divided by the total number of cells) are shown in Fig. 6-4 and Fig. 6-5 for spindle like particles and

spherical particles, respectively. It should be noticed that the counting was realized only on the cells which were still adherent to the dish bottom; consequently, the mortality ratio could be underestimated. However, the microscopy pictures show a density of cells that seems identical before and after the treatment, indicating that only a few cells came out of the support. The results presented in Fig. 6-4 are given for different initial concentrations of particles and for 20, 40 or 60 min of exposure to the field. The concentration is a weight ratio and the total volume of feeding liquid above the layer of cells is 1 mL. The data at zero frequency represent both the results obtained with the blanks (not submitted to magnetic field) and those, in blue and shifted to the left of zero frequency, performed with a constant field, corresponding to Hmax.

As shown in Fig. 6-4 and Fig. 6-5, there is a significant increase of cell mortality when the particles are submitted to an oscillating magnetic field with a clear relationship between mortality and the utilized mass fraction of particles or the time of exposure. Besides, cell mortality shows a small tendency to increase with the applied frequency between 2 and 10 Hz. At last, we can see that there is an increase of mortality ratio when the time of exposure was increased from 20 to 40 or 60 min.

In order to understand the process involved, and, more precisely, to determine whether the death of the cells is due to the pressure exerted on their surface by the magnetic particles, or to the vertical oscillating motion of the particles, we assayed the mortality by running dishes with a constant magnetic field whose value is equal to the maximum of the oscillating field. As shown in Fig. 6-4 and Fig. 6-5 (blue dot), the mortality ratio remains practically at the same level than in the absence of magnetic field, though the field was at its maximum value during the duration of the experiment, contrary to the vibrating case.

As the mortality takes place quickly after the application of the magnetic field, mechanisms like apoptosis, which requires a few hours for its activation, are excluded, and it is likely that mechanical damage of the membrane is responsible for the increase in cell mortality.

To confirm the mortality results, the flow cytometry has been used to detect the mortality, as showed in Fig. 6-3. This is one of classic experiences, with a frequency of 5Hz and 20min of treatment and concentration of spherical particle is about 0.05% wt. We can see that to compare the reference, in black line, the result of treatment is pretty significant, in red line

with clearly two peaks. Left one represent live cell, which is bond with the peak of reference, and right peak represent dead cell.

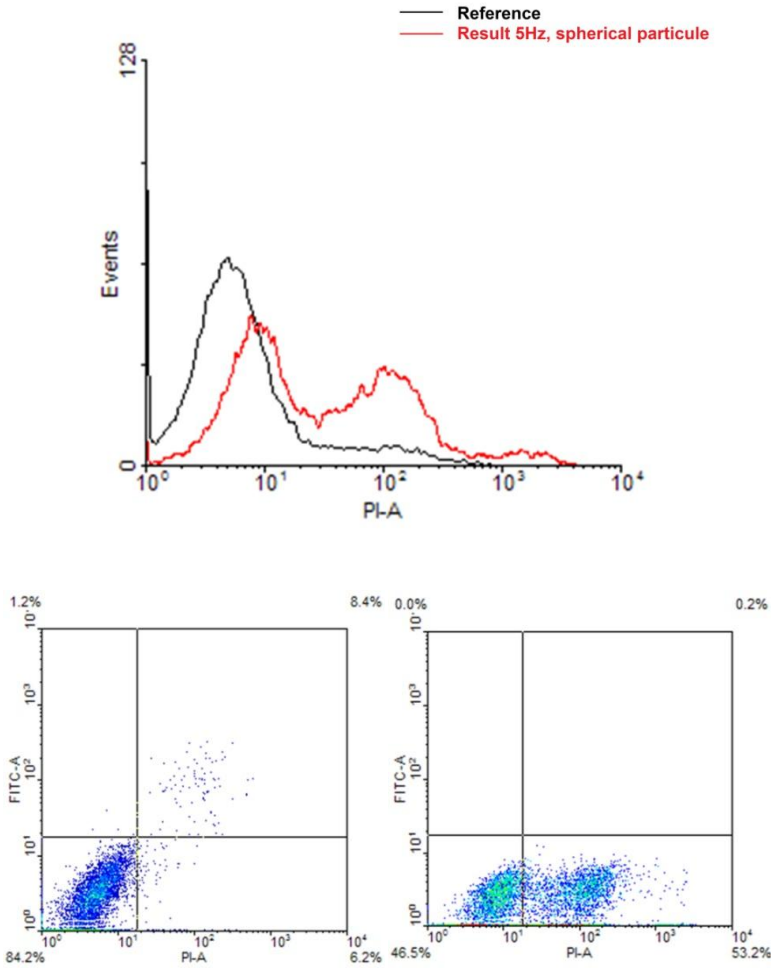

Fig. 6-3: The result of mortality test by flow cytometry, without field (left) and with field (right)

In order to confirm those results we have compared the mortality by putting one dish directly on the magnet (this is the first point in Fig. 6-5) to the other experiments where the magnet is vibrating below the Petri dish. Although the field was at its maximum value all the time, contrary to the vibrating case, the mortality remains slightly lower than at higher frequency, nevertheless it is almost in the uncertainty range and more precise experiments would be needed to confirm frequency dependence. The last observation is an increase of mortality when the time of exposure is increased from 20 mins to 40 mins.

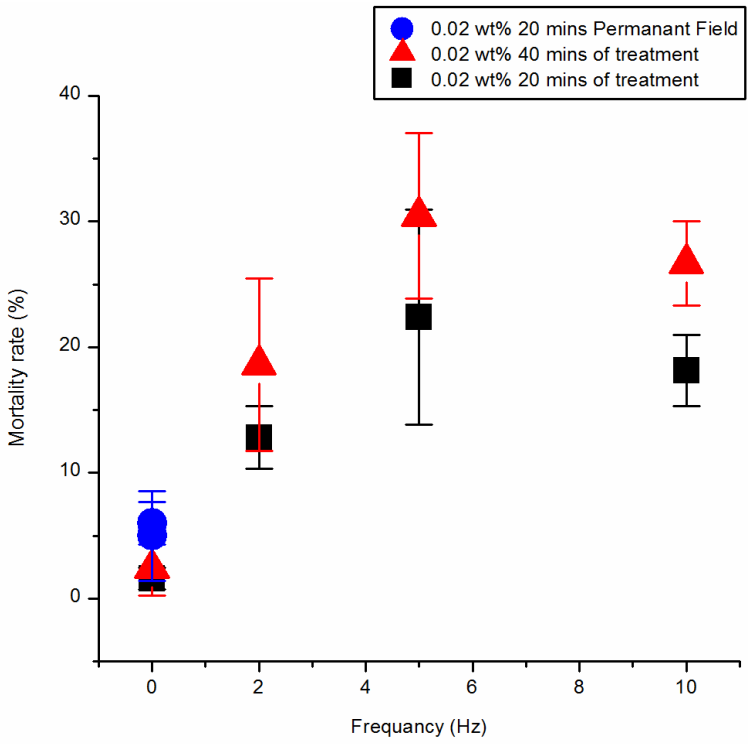

Fig. 6-4: The result of mortality test, with Spindle-type nanoparticle

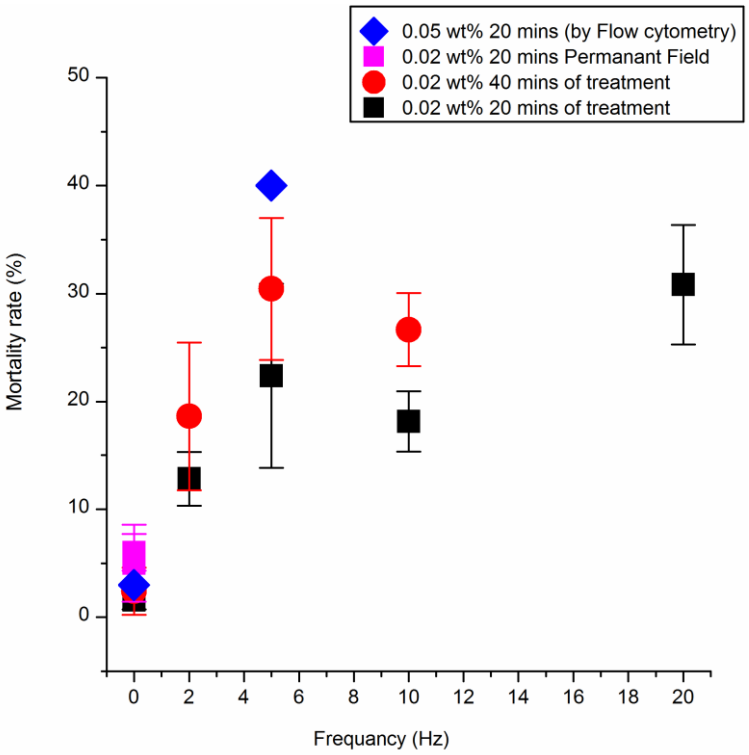

Fig. 6-5: The result of mortality test with spherical microparticle. The lower points at zero Hz are the reference results with no field applied on the magnetic particles; the upper points at 0Hz correspond to an exposure to the constant maximum field

As the mortality takes place quickly after the application of the magnetic field, induced mechanisms like apoptosis, which needs a few hours for its activation, is excluded, and it is likely the mechanical damage of the membrane which is responsible of this increase in cell mortality. In the next section we shall quantify the force applied to the magnetic particles and its resulting motion inside the cytoplasm.

6.4. Theory

In order to get a deeper insight into the magnetolysis mechanism, which leads to cell death, it was necessary to know more precisely about the penetration or indentation depth of the particles inside the cell when applying a given magnetic force, as showed in chapter 4, the penetration, δ, of a particle inside an elastic medium can be modeled by the Hertz theory. For a spherical particle of radius R, the relation between the force F and the penetration, δ, is given by:

$$F = \frac{4\sqrt{R}}{3}\frac{E}{1-\nu^2}\delta^{\frac{3}{2}} \qquad (6.12)$$

where, E is the Young modulus and ν the Poisson coefficient that we shall take equal to 0.5, since the cell is usually considered as an incompressible medium (46). For an acicular particle, the total indentation force is given by (99,100):

$$F = \frac{2}{\pi}\frac{E}{1-\nu^2}\frac{\delta^2}{\tan\beta} \qquad (6.13)$$

where β is the angle between the surface of the material and the surface of the cone; for the spindle Fe@Si particles that we described here, their extremity can be considered to be conical. Based on MEB image (Fig. 5-3), $\beta=\pi/2-\theta$ is equal to 75°.

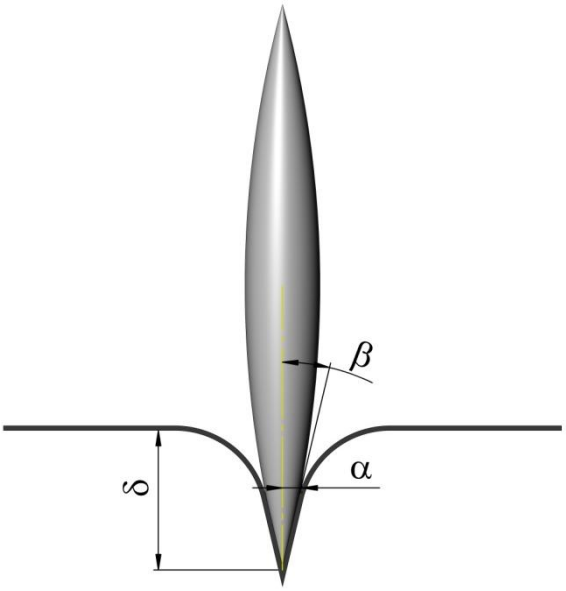

Fig. 6-6: Conical particles

In this case, the indentation depth and the radius of the contact area, *a,* are further related by:

$$\delta = \frac{\pi}{2} a \tan\beta \tag{6.14}$$

The Eq.(6.12) for a spherical contact and the Eq.(6.13) for a conical contact can then be written as:

$$F = CGH \text{ or } H = \frac{1}{C} JF \tag{6.15}$$

with $G = E/3$, $C = 4\sqrt{R}/1-\nu^2$ and $H = \delta^{3/2}$ in the case of a spherical contact; $C = 6/\left[\pi(1-\nu^2)\tan\beta\right]$, and $H = \delta^2$ for a conical contact.

For a linear viscoelastic model, the time-dependent generalization of Eq. (6.15) is given by (16):

$$H(t) = \frac{1}{C}\int_0^t J(t-t')\frac{\mathrm{d}F(t')}{dt'} = \frac{1}{C}\left[J(0)F(t) + \int_0^t \dot{J}(t-t')F(t')dt'\right] \tag{6.16}$$

where *J(t)* is the dynamic compliance of the system that is to say, the deformation of the material at time *t*: $\gamma(t)$ resulting from the application of a unit step of stress, $\sigma(0)$, at time $t = 0$:

$$\gamma(t) = J(t)\sigma(0) \tag{6.17}$$

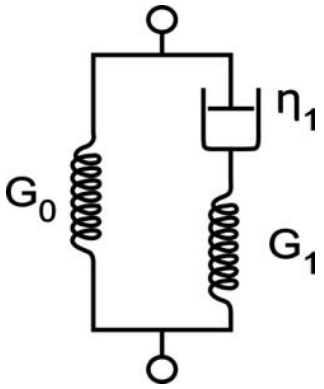

Fig. 6-7: A schematic of the Zener Model

For a Zener model representing a viscoelastic solid, we have:

$$J(t) = \frac{1}{G_0}\left(1 - \frac{G_1}{G_1 + G_0} e^{-t/\tau}\right) \tag{6.18}$$

with

$$\tau = \tau_1\left(\frac{G_1 + G_0}{G_1}\right) \text{ and } \tau_1 = \frac{\eta_1}{G_1}$$

η_1 and G_1 are respectively the shear modulus and the viscosity of one branch of the model and G_0 is the shear modulus of the second branch, placed in parallel with the first one, τ the characteristic/relaxation time.

With the help of Eqs. (6.16) and (6.18) we are able to predict the indentation $\delta(t)$ for a given applied force $F(t)$. In order to check the validity of Eqs. (6.16), (6.18), we have compared the prediction of this model of dynamic indentation to the numerical results, which can be obtained by Finite Elements Method (FEM). We did this test for a spherical indenter using the software Abaqus, which can integrate the Zener model for the rheology of the material. The force $F(t)$ applied to the spherical particle in FEM and appearing in Eq. (6.16) corresponds to a linear ramp reaching the value C_1 in 0.1 s and then obeying Eq.(6.11). The resulting indentation obtained either with the FEM software or with Eq. (6.16) perfectly coincide,Fig. 6-8, which validates the use of Eq. (6.16) to predict the indentation depth for any kind of applied force.

6.4.1. Generalization of the Hertz theory

For a linear viscoelastic model, the time dependent generalization of (17) is given by:

$$H(t) = \frac{1}{C}\frac{C_1}{G_0}\left[\sin\omega t - \frac{G_1}{G_1+G_0}\frac{\omega\tau}{1+\omega^2\tau^2}\left(\cos\omega t + \omega\tau\sin\omega t - e^{-t/\tau}\right)\right] + \frac{C_0}{C}J(t) \qquad (6.19)$$

where the constant C is depending on the shape of the indenter. For $t >> \tau$, which is the case in our experiments, the exponential term disappears in Eq.(6.19) and it remains an oscillating part $H_{osc}(t)$, and a constant indentation $H_p = \frac{1}{C}\frac{C_0}{G_0}$ related to the constant part of the applied force. The amplitude in microns of the oscillating part of the indentation: $A = \delta_{max} - \delta_{min}$ is plotted in Fig. 6-9 for the two kinds of particles. It can be seen that the amplitude decreases with the frequency and is approximately ten-fold larger for the spherical particle than for the spindle one. Actually this lower indentation of the spindle particle is due to the difference in volume between the two particles, which for the spherical particle is of 4.2 μm^3 and for the spindle-type particle of 0.002 μm^3, hence 2000-fold lower.

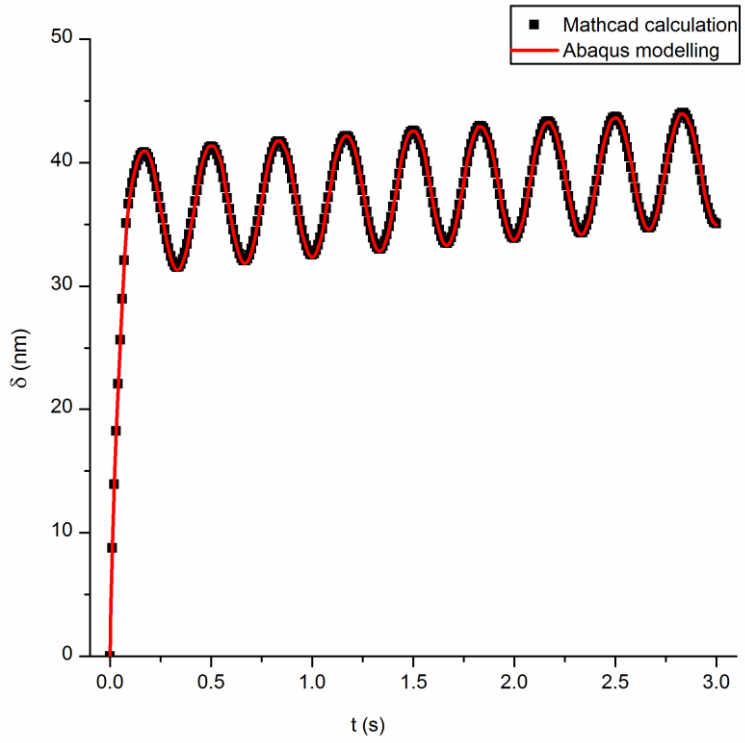

Fig. 6-8: Comparison between Eq.(6.19) and FEM results for a Zener model with the parameters G_0=210Pa, G_1= 181Pa, τ_1=5.6s

This indicates that, for particles of equal volume, it is much more efficient to obtain a mechanical perforation of the membrane with spindle particles rather than with spherical ones.

As can be seen in Fig. 6-9, for the spherical particle, the amplitude of indentation decreases from 20 nm when $\omega\tau \ll 1$ to 7 nm for $\omega\tau \gg 1$. For the spindle particle, the amplitude decreases from 2 nm for $\omega\tau \ll 1$ to about 1.2 nm for $\omega\tau \gg 1$. The transition frequency corresponding to $\omega\tau = 1$ is $\nu \approx 0.02 Hz$, indicating that with a few Hertz the "high frequency" regime is already attained.

In the experiments with the magnet at rest just under the Petri dish, the applied magnetic force is constant and equal to C_0+C_1 and the maximum indentation will be:

$$H_{\max} = \frac{1}{C}\frac{C_0 + C_1}{G_0} \qquad (20)$$

using $H=\delta^{3/2}$ for a sphere and $H=\delta^2$ for a cone together with the respective values of C (cf. appendix), one obtains, $\delta_{\max}$= 71 nm for the sphere and $\delta_{\max}$= 9.6 nm for the cone.

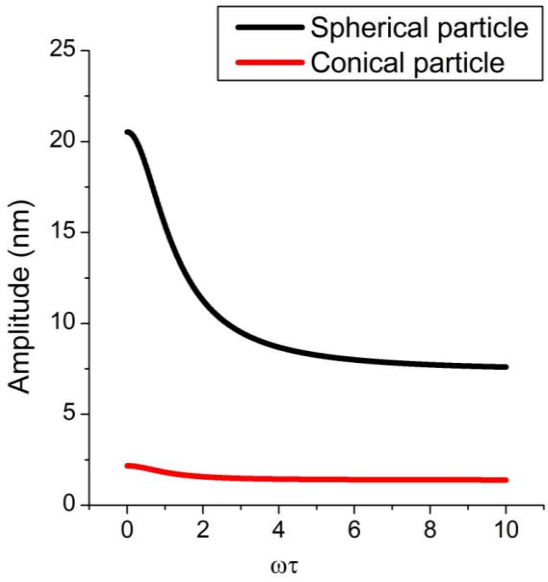

Fig. 6-9: Amplitude of the oscillation versus ωτ upper curve spherical particle; lower curve spindle like particle

In summary, the amplitude of the "oscillating" indentation should be around 1 nm for the spindle particles and 7 nm for the spherical ones, but the "static" indentation under the maximum permanent field is 9.6 nm and 71 nm for the spindle and spherical particle, respectively. This theoretical analysis indicates further that the indentation generated by a

static magnetic field is much larger than that obtained with an oscillating one of same amplitude and that the indentation depth remains quite small and in any case lower than 100 nm.

On the other hand, we have found experimentally (see above) that a static indentation has no noticeable effect on the cell viability and that an oscillation was needed to damage the cells. This likely indicates that the dynamics of indentation plays the major role and that, like in hyperthermia, it could be the dissipation of mechanical energy in heat, which provokes cell death, since this dissipation increases with the frequency. The dissipated power per particle is given by:

$$P(t_0) = \frac{1}{T} \int_{t_0}^{t_0+T} F_H(t)\,\dot{\delta}(t)\,dt \qquad (21)$$

where T is at least one period and $t_0 >> \tau$, in order to get the equilibrium value. The dissipated power versus frequency reaches a plateau at frequencies above $\nu = 1/\tau = 0$. However, its value is very low (4×10^{-20} Watt per particle). As only an average of a few tens of particles is interacting with a single cell, it is unlikely that the dissipated power results into any noticeable increase of temperature and, consequently, into cell death by hyperthermia.

6.5. Discussion

We have found in the previous section that the amplitude of the oscillating indentation due to an isolated magnetic particle was not larger than a few nm with an associated magnetic force in the pN range. Therefore, it is very doubtful that the observed cell death can be related to such a low indentation.

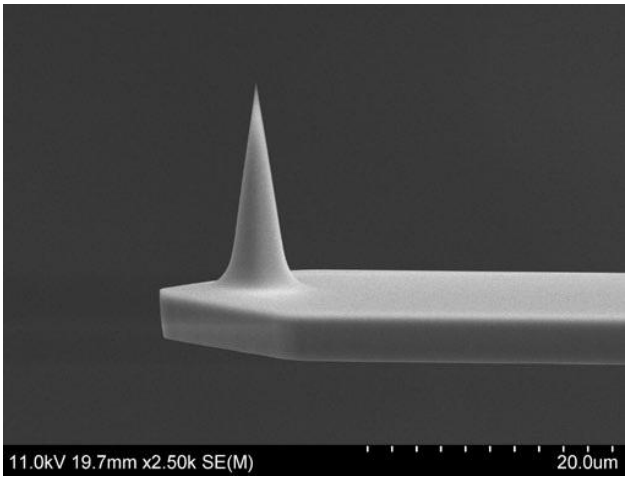

Fig. 6-10: A conical AFM probe, with the same overall dimension as a spindle type magnetic particle

The same kind of mechanical indentation can be applied on cells by use of an AFM tip. To check whether this force induces cell death, we then used an AFM tip either with a conical or a spherical shape in order to apply on a given cell an oscillating indentation of known amplitude. The conical probe had approximately the same conical angle and size as a spindle type particle. Applying a force of a few pN, the probe did not cause any damage to the cells. It is only when increasing the force in the nN range that membrane damage and then cell death could be obtained, as illustrated in the sequence of Fig. 6-11. At the beginning of the experiment (Fig. 6-11-1), we can see two cells, one is intact and the other is already dead and strongly coloured by the trypan blue, it serves as a position marker. Then the intact cell was periodically indented by the conical probe during 20 min, with a force of 1 nN, corresponding to an indentation depth of 400 nm and a frequency of 5 Hz (Fig. 6-11-2). Fifteen minutes after the indentation period, there are some blebs blown up (Fig. 6-11-3), then those blebs are expelled 45 min after the indentation and the cell loses its integrity and is stained by the trypan blue dye, indicating cell death (Fig. 6-11-4).

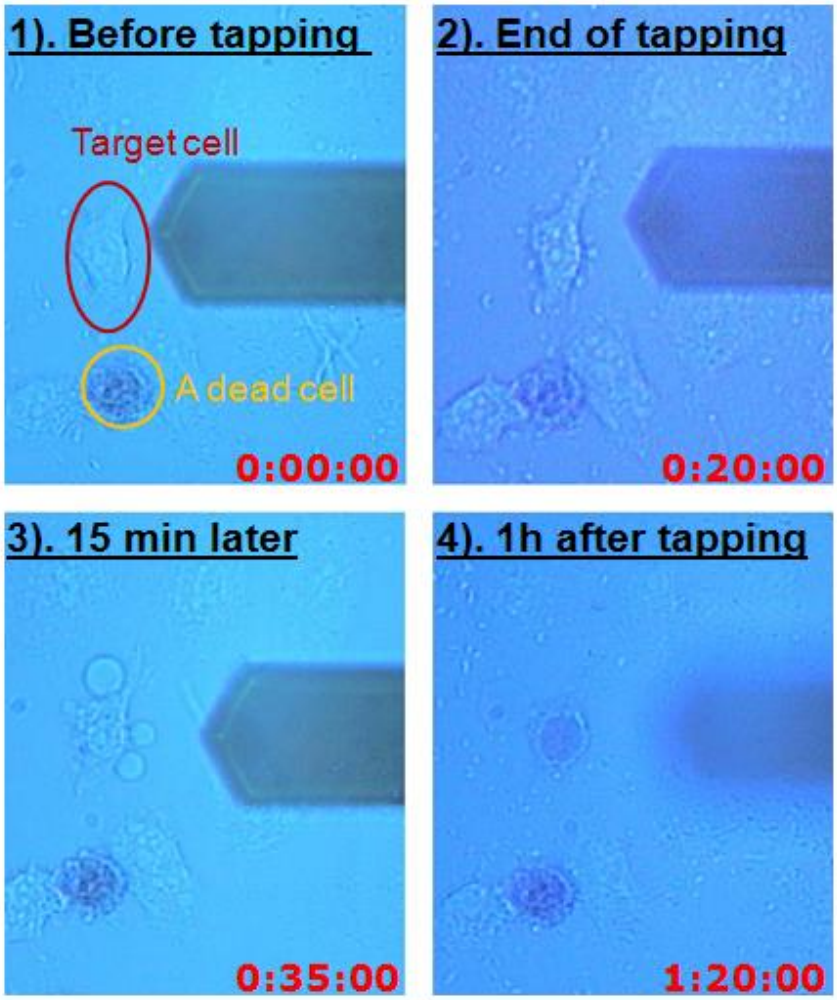

Fig. 6-11: Indentation with a conical tip during 20mn (upper part) Result after waiting 15mn and 1h (lower part)

To mimic the use of spherical magnetic particles, we also performed the same experiment by using a spherical tip of 2.5 µm radius instead of the conical one. Four amplitudes of oscillation, i.e. 100, 200, 300 and 400 nm were used. The red and yellow circles in Fig. 6-12 represent cells, which were submitted to two imposed amplitudes (400 and 300 nm respectively) for 20 min and with a frequency of 5 Hz. The impact of the amplitude is clearly evidenced in Fig. 6-12 where the cell stressed with an indentation amplitude of 400 nm becomes coloured by the trypan blue (red circle) whereas the other one stressed with the lower amplitude of 300 nm (or below, data not shown) remains intact (yellow circle).

It should be noticed that the associated oscillating force corresponding to the indentation amplitude of 400 nm is of 1.8 nN. This is coherent with the forces needed for the magnetolysis of red blood cells as reported by Hategan et al. (2003), which are in the nN

range (101). Then, in our magnetolysis experiments, it seems most unlikely that the magnetic force on a single particle, which is smaller by at least two orders of magnitude, is responsible for cell death. Thus, in the case of our experiments, magnetolysis can be related to the formation of clusters of particles on the cell surface, which are indeed observed when the magnetic field is applied, as illustrated in Fig. 6-13. These clusters of irregular shape are formed as a result of particle's self-attraction. When these clusters become large enough, their magnetic moment (which is increasing proportionally with their volume) can thus become sufficient for allowing the clusters to damage the cell membrane. Furthermore these elongated clusters should align in the direction of the field, hence perpendicularly to the surface of the cells. Consequently, the curvature radius of the indentation tip remains of the same order of magnitude as the one of a single particle. For instance, if a cluster contains 100 particles and as the indentation for an elongated cluster increases with the square root of the force, which is itself proportional to the number of particles, one obtains an indentation depth corresponding to a force of one order of magnitude larger than for isolated particles. As shown with AFM tips, this is large enough to mechanically damage the cells.

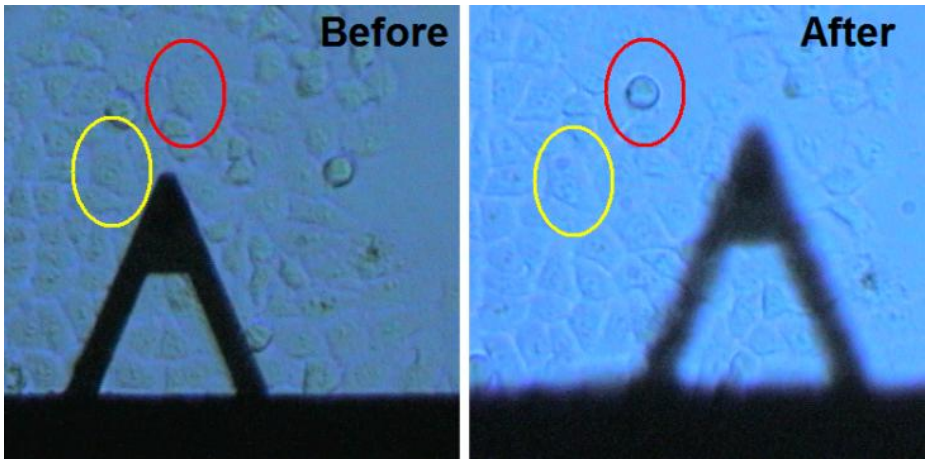

Fig. 6-12: The result of mortality test by spherical tips

The formation at the cell surface of clusters of paramagnetic carbon nanotubes when submitted to a rotating field has also been reported very recently (95). Here too the application of the field was associated with a net decrease of cell viability. It is therefore the clustering of magnetic particles under the applied field, which can be responsible for the destruction of the cells. Nevertheless, it remains a mystery about the need of an oscillating force, since a static one of comparable amplitude has no influence on cell viability. It could be however related to a characteristic time of membrane healing after perforation. The indentation of particles is likely inducing in its vicinity a size increase of the fluctuating

channels in the membrane. The resealing time of pores in cells is extremely variable but can be of the order of seconds in the presence of an hydraulic stress (102), and long enough in the case of an oscillating stress to lead to cell death. We intend in a further study to use conductivity measurements to verify if this hypothesis is supported by a correlation between the frequencies of the applied field and pore formation.

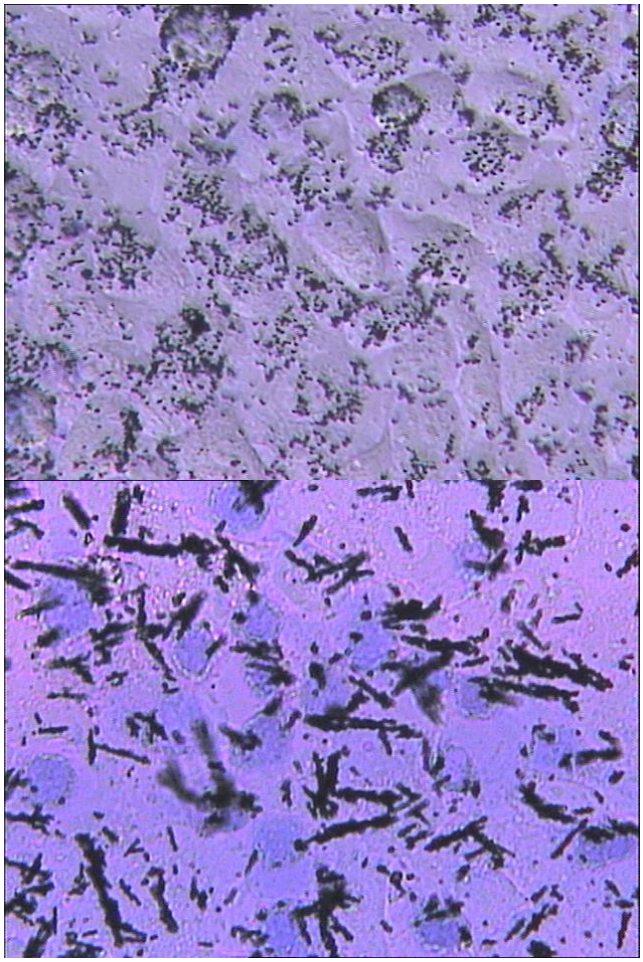

Fig. 6-13: The photo of spherical particles and cells before (upper part) and after (lower part) the application of the oscillating field, average cell diameter is 25µm the blue staining indicates the death of the cell

6.6. Conclusions

We have found that, as already observed in similar situations, it is possible to damage cancer cells with magnetic particles of sizes in the range of 100 nm to a few microns by exposing them to an alternative magnetic field. Besides, we show that a static magnetic force was much less efficient than an oscillating one. By using a device, which imposes a well defined

magnetic force, and with the help of AFM to characterize the mechanical properties of HepG2 cells, we demonstrated that the indentation caused by the magnetic force is only of the order of a few nm. Such a low indentation, imposed through an AFM tip, is unable to provoke cell damage. Indeed, at least a few hundred nm of indentation is needed to trigger cell death, as observed with the trypan blue staining assay. Our observation of a clustering of the particles under magnetic field, suggests strongly that it is the formation of magnetic particle aggregates, which considerably increases the magnetic force and their pressure onto the cells, and, consequently, causes membrane damage and ultimately cell death. The results obtained with submicronic spindle like particles are promising, since with particles of 10^{-3} μm^3 volume order, which can indeed circulate in blood capillaries without causing embolism, it was possible to destroy cells with a moderate field, such as those easily obtained in MRI scanners.

Concerning the need of an alternative field rather than a static one to obtain a clear cell mortality increase, a mechanism of delayed pore resealing could be at its origin. Further investigations coupling periodic indentation and conductivity measurements should help to verify this hypothesis. If this is the case, then a control of the applied magnetic force by magnetic particles could be a mean to trigger membrane permeabilization and intracellular drug delivery.

7. MAGNETIC HYPERTHERMIA

7.1. Introduction

As presented in section 2.1.5, hyperthermia has very interesting applications, especially in cancer treatment(103); it is one kind of thermotherapy, which consists in curing cancer by heating the tumor. In this chapter, we are going to discuss the primary stage of magnetic hyperthermia, the temperature increase of magnetic nanoparticles under an alternative magnetic field. This is usually done with spherical nanoparticles whose diameter is around 10nm and at frequencies of a few hundred kilohertz. The dissipated power comes from the lag between the magnetic moment and the direction of the field, which itself is related to the relaxation time, of the magnetic moment. Small particles have a fast relaxation time, τ, and the optimum frequency dictated by $\omega\tau=1$ is then high, as well as the dissipated specific power, which is given by:

$$P = \frac{\mu_0 H^2}{2} \frac{\omega \chi''(\omega)}{\rho} \qquad with \quad \chi''(\omega) = \chi_0 \frac{\omega\tau}{1+(\omega\tau)^2} \tag{7.1}$$

Here ρ is the density of the particles and χ_0 the zero frequency magnetic susceptibility, which at low field is $\chi_0 = \frac{\mu_0 M_r^2 V_p \phi}{kT}$ with V_p the volume of the particle, M_r its remanent magnetization and ϕ the volume fraction. At $\omega>1/\tau$ the limit power is proportional to $1/\tau$.

When the particles become larger, the Brownian relaxation time, τ, which is proportional to the cube of the radius, becomes much larger and the viscous dissipation decreases, but on the other hand larger particles are non longer magnetic monodomains and can present some hysteresis ,due to the motion of the magnetic walls, which can also dissipates some energy. The interest of this dissipation being that it is not dependent on the viscoelastic properties of the medium in which the particles are dispersed. We are going to study this hysteretic dissipation for two kind of magnetic particles: the cobalt nanowires which we have synthesized see section 5.2 and commercial iron oxide particles, section 5.3.2 which, thanks to a high hysteretic cycle, will serve as reference system to our study.

7.2. Experimental setup, material and methods

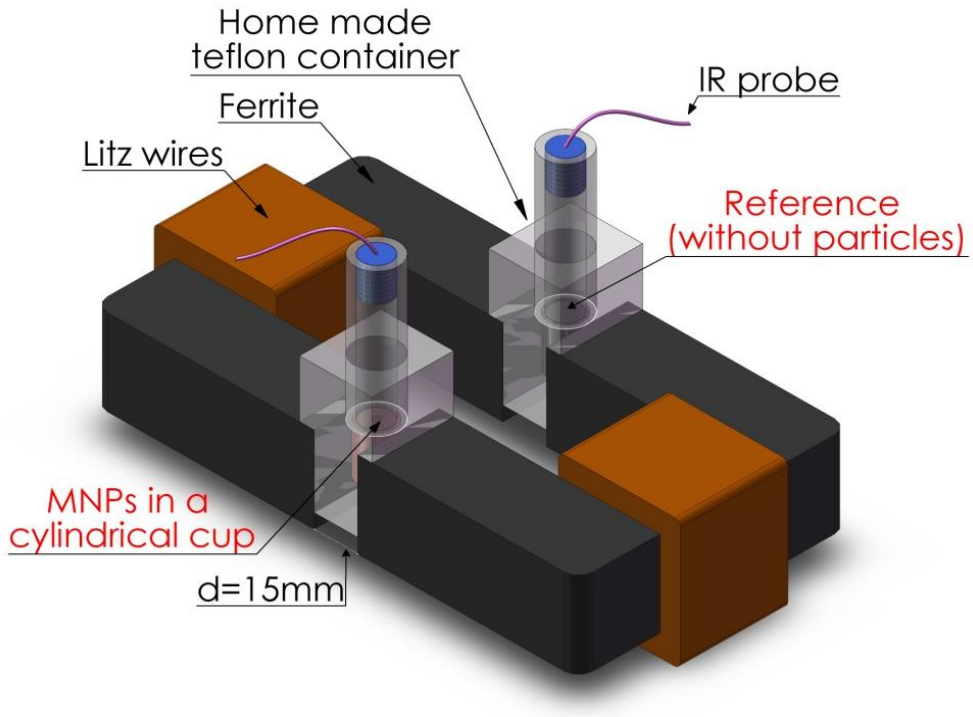

Fig. 7-1 : Experimental setup for hyperthermia

The experimental setup consists of two commercial U-shaped ferrites (Epcos, France) oppositely fixed on a wood support, the gap between the two ferrites is 15mm. To avoid the substantially increase of the impedance of standard copper wires at high frequency due to skin effects. we used Litz wires (LGM, France) to make the coil(104,105), the exterior diameter of the wire is 3.1mm the resistance of 1.3 Ohm and an inductance of 0.84mH. The amplifier is an audio Crown Macrotech 5002VZ which can gives 2500W in the range 20Hz-20kHz. In order to decrease the impedance at high frequency a capacitance bridge is used which is tune to the resonance frequency of the circuit: $LC\omega^2=1$. We made two identical electromagnets which are placed facing each other as shown in Fig. 7-1. Two homemade Teflon containers are located in the gap, and two cylindrical cups, easy to install, are inserted in the middle of the containers, every cup has a cylindrical hole in the middle, the diameter of the hole is 4mm, and the deepness is 5mm. One cup is filled with the nanoparticles, and the other one is for the reference.

A classical resistance thermometer as thermocouple or PT100 cannot be used for this experiment, due to the self-heating in an alternative magnetic field. In our case, two IR probes

(Rateck, Santa Cruz, CA) have been installed above the cylindrical cup, coaxially, and have been connected with one transmitter module DIN then through a USB cable; we can get the two temperature curves on the same screen. Thanks to the close focus lens, we can get a very small measurement spot, diameter about 2mm, and the distance between the probe and the cylindrical cup is about 7cm, which corresponds to the focal length of the device. This installation allows us to obtain precisely the temperature change after application of the field by recording the temperature difference between the two channels. The field in the gap is calibrated with respect to the applied current with a hall gaussmeter working up to a few kHz. The maximum current we can apply is 10A at 10 kHz, which corresponds to a field of 150 Oe (~12 kA/m) mainly because of the voltage break-up of the capacities at higher voltage.

7.3. Determination of thermal properties

In this section we need to obtain the thermal conductivity and the specific heat of the magnetic powder or of a magnetic suspension in order to calculate with a FEM software the increase of temperature for a given power input.

7.3.1. Effective thermal conductivity

There are some theories to calculate the thermal conductivity of a mixture(106–110), which are more adapted than the linear rule of mixture. The reduced thermal polarizability, is defined as follows:

$$\beta = \frac{k_2 - k_1}{k_2 + 2k_1} \tag{7.2}$$

Where k_2 is the thermal conductivity of metal, and k_1 the thermal conductivity of air or liquid.

We have noticed that the Maxwell(107) model for the thermal conductivity gives good predictions(111,112), so in this study, we use this model to calculate the thermal conductivity. According to the Maxwell model, which assumes randomly distributed and non-interacting spherical particles in a homogeneous continuous medium, the effective conductivity is given by the expression:

$$\frac{k_{eff}}{k_1} = \frac{1 + 2\beta\phi}{1 - \beta\phi} \tag{7.3}$$

A more accurate result was obtained by simulation on a cubic network (113) Their numerical result can be fitted by the power law:

$$k_f = k_1\left(1+\alpha.\phi^{\beta}\right) \qquad (7.4)$$

With β=Log(3)/Log(2) and α=3.2β

The comparison between the two equations (7.3) and (7.4) is shown in Fig. 7-2. It appears that the Maxwell model gives a quite good prediction, so we shall use it in the following

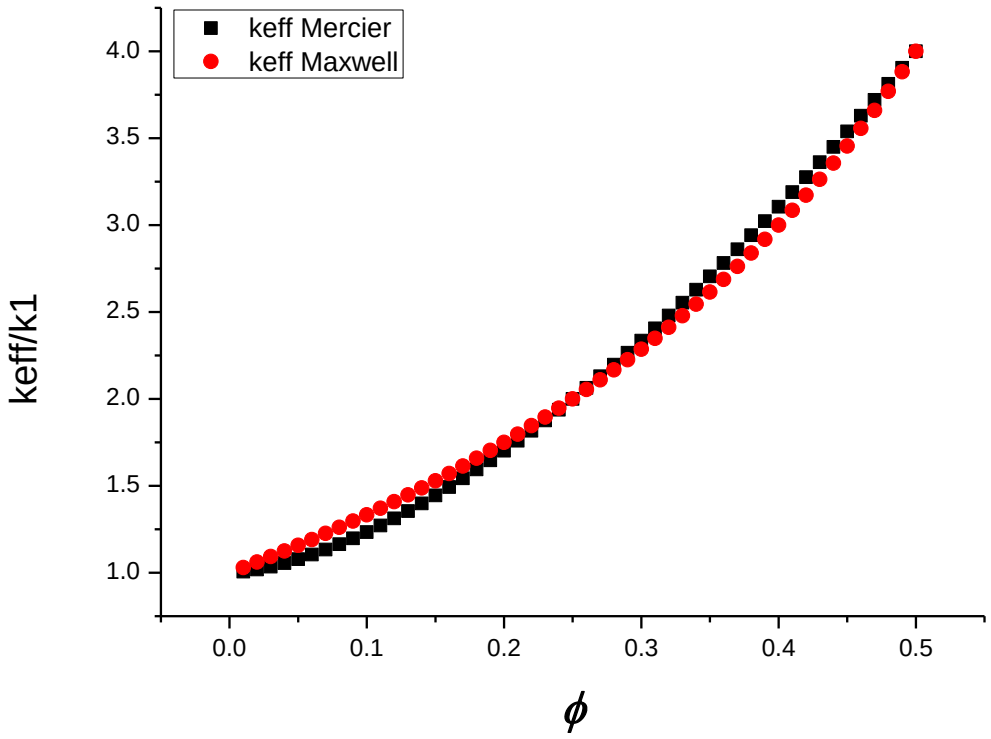

Fig. 7-2: Comparison between Maxwell model and the numerical result of Mercier et al for the relative thermal conductivityof a powder

7.3.2. (Mass) Specific heat capacity

For the specific heat capacity, the thermal equilibrium model for mixtures of materials of materials is used for the theoretical prediction(114,115)

$$C_{p,m} = \frac{\phi\rho_p C_{p,p} + (1-\phi)\rho_1 C_{p,1}}{\phi\rho_p + (1-\phi)\rho_1} \tag{7.5}$$

With $C_{p,p}$ the specific heat capacity of particle, and $C_{p,1}$ the specific heat capacity of air or liquid, ρ_p the density of particle, and ρ_1 the density of air or liquid.

7.4. Energy dissipated by hysteresis

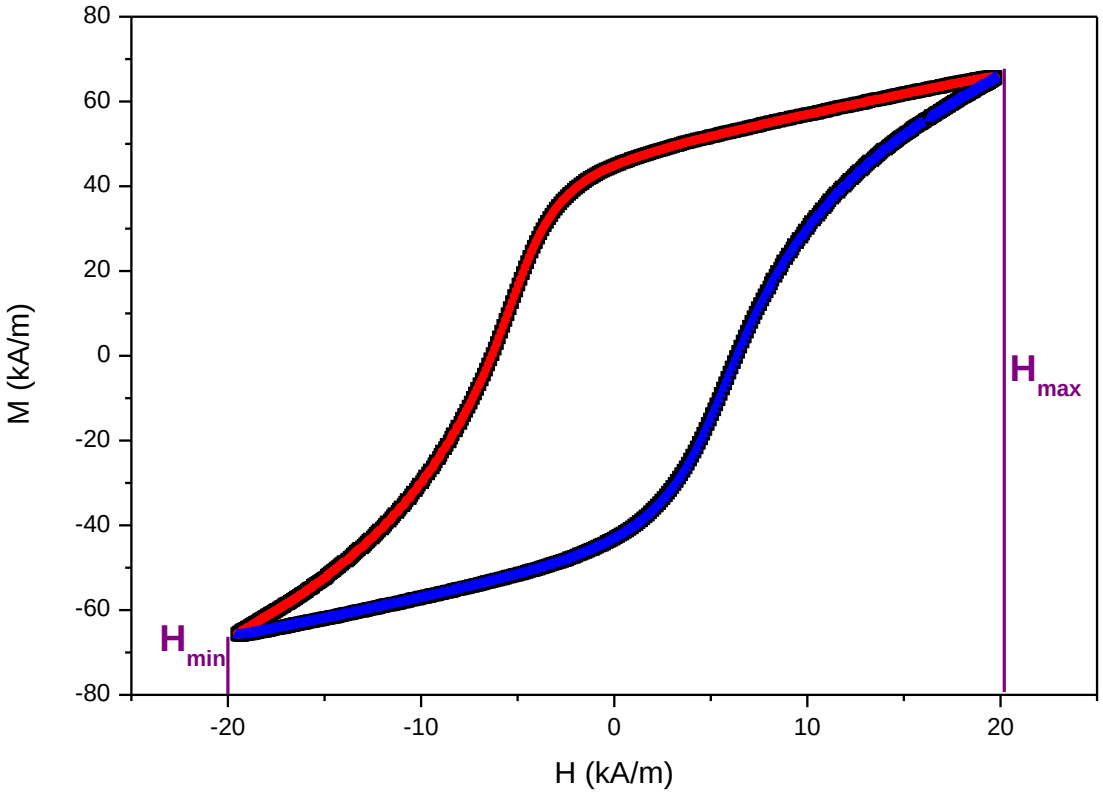

Fig. 7-3: Hysteresis loop, the dissipated energy is the area under red line minus the area under blue line. Here for cobalt nanowires

We already discussed in section 2.1.5, that the area of the hysteresis hoop is the energy dissipated in the environment under the form of thermal energy. The best way to calculate this area is to divide the hysteresis hoop in two parts as shown in Fig. 7-3, the area of hysteresis is just the area under red curve minus the area under blue curve, where the red curve is M_1 and the blue curve is M_2. So the energy of dissipation is given by:

$$W = \mu_0 V \int_{H_{\min}}^{H_{\max}} (M_1 - M_2)\, dH \tag{7.6}$$

We can fit these two parts from the data files of the hysteresismeter, as Fig. 7-3. Then we can calculate the energy dissipations in different applied magnetic fields. The change of the hysteresis loop with the amplitude of the field is shown in Fig. 7-4 and Fig. 7-5 for cobalt nanowires and iron oxide particles respectively.

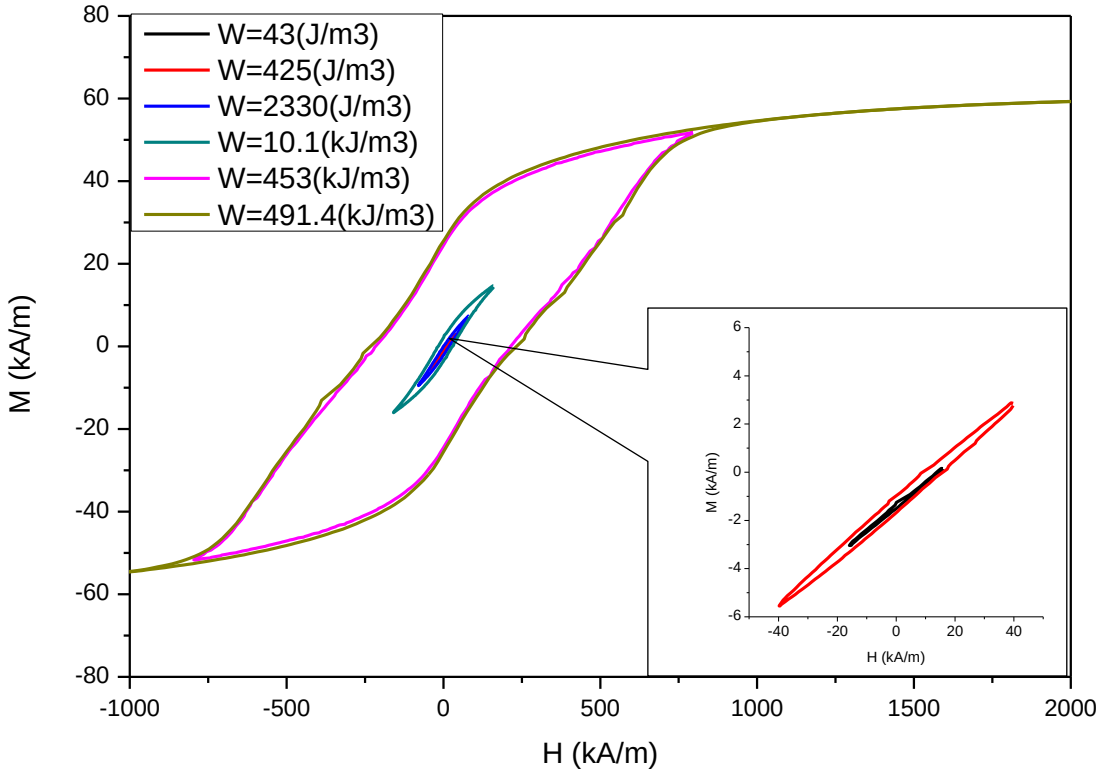

Fig. 7-4: Hysteresis loop of cobalt nanowires at different fields

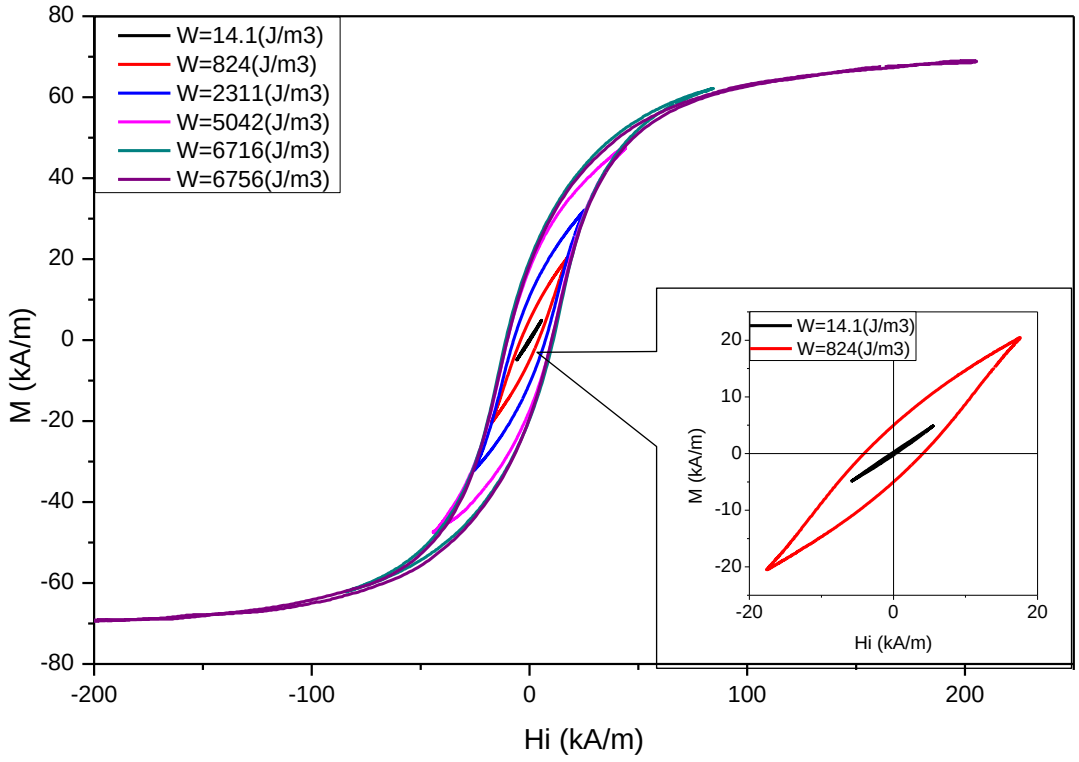

Fig. 7-5: Hysteresis loop of iron oxide at different fields

Iron oxide powder				Cobalt nanowires		
H(Oe)	H(kA/m)	W(J/m^3)		H(Oe)	H(kA/m)	W(J/m^3)
68.6	5	14		200	16	43
221	18	824		500	40	425
316	25	2311		1000	80	2330
553	44	5042		2000	159	10980
1060	84	6716		10000	796	453000
2570	205	6756		90000	7162	491400

Tab. 7-1: Disspated energy from Eq.* (7.6)*; left is iron oxide and right is cobalt nanowires

The dissipated energy obtained from the Eq. (7.6) is reported in the Tab. 7-1 . We can see that the cobalt nanowires produce more energy than iron oxide particles when the applied magnetic field is larger than 80kA/m; unfortunately, our device is not adapted to apply fields larger than 12kA/m. Then the maximum applied field (H=12kA/m) is smaller than the smallest one which has been used for cobalt measurement of hysteresis. In order to obtain nevertheless a value for the dissipation energy we have fitted the three lowest values of the table with a power law (cf. Fig. 7-6):

$$W = aH^b \tag{7.7}$$

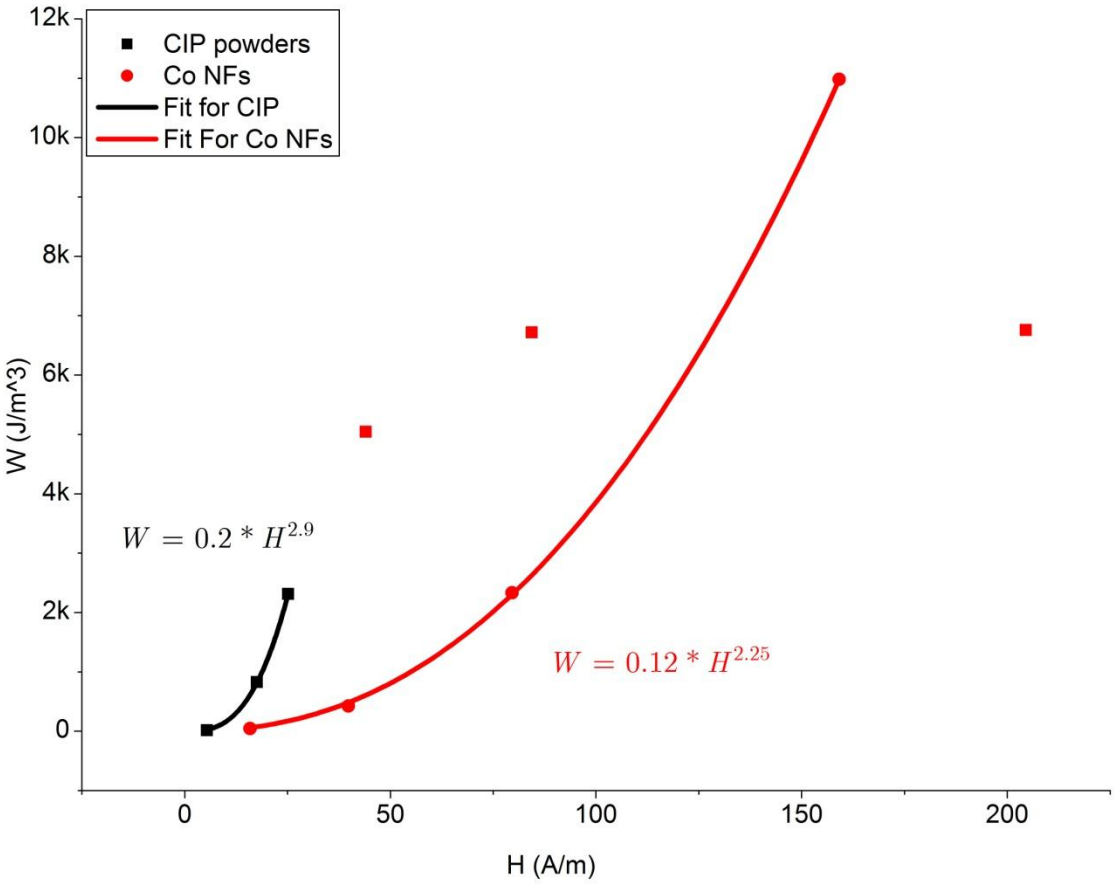

Fig. 7-6: The fitting of dissipated energy versus magnetic field, to extrapolate the dissipated energy

We obtained the following functions (with H in kA/m):

$$W = 0.12 * H^{2.25} \tag{7.8}$$

for the cobalt particles, and:

$$W = 0.2 * H^{2.9} \tag{7.9}$$

for the iron oxide particles

The maximum magnetic field we have applied is 12kA/m, so we obtain the corresponding dissipated energy as 22.4J/m^3 for cobalt nanowires and 270J/m^3 for iron oxide powders. Nevertheless, it is clear that this extrapolation can give rise to some uncertainty especially for the cobalt particles.

The power dissipated in our device represented in Fig. 7-1 is given by:

$$P = W \cdot f \cdot m_p / \rho \qquad (7.10)$$

With *f*: the applied frequency of magnetic field, m_p the mass of particles inside the cylindrical hole and ρ he metal density.

7.5. Solidworks simulation of temperature rise

In order to be able to simulate the increase of temperature in our device, for a given injected power, we have used Solidworks software. Firstly, we want to predict the increase of temperature in our experiment for a given injected power; the adjustement of the experimental curve with the theoretical one will then give us the experimental power injected that we can finally compare with the one obtained from the hysteresis loop.

First of all, we need to simplify the experimental setup of Fig. 7-1; we left only the parts close to the particles, to decrease the computer load, at the same time we have to take enough, to simulate the reality, as shown in the upper part of Fig. 7-7. The powder or the suspension is represented in red on the left side. Then we feed the properties of all parts, like thermal conductivities, heat specific capacities, densities etc, and we created the mesh, as shown in the second part ofFig. 7-7.

A typical result of the simulation is shown in the lower part of Fig. 7-7. We are looking to the temperature at the surface of the central part which contains the particles since the measurement of temperature by IR probe is taken at this place. The temperature versus time at this place can be collected and we can compare this curve with our experimental results.

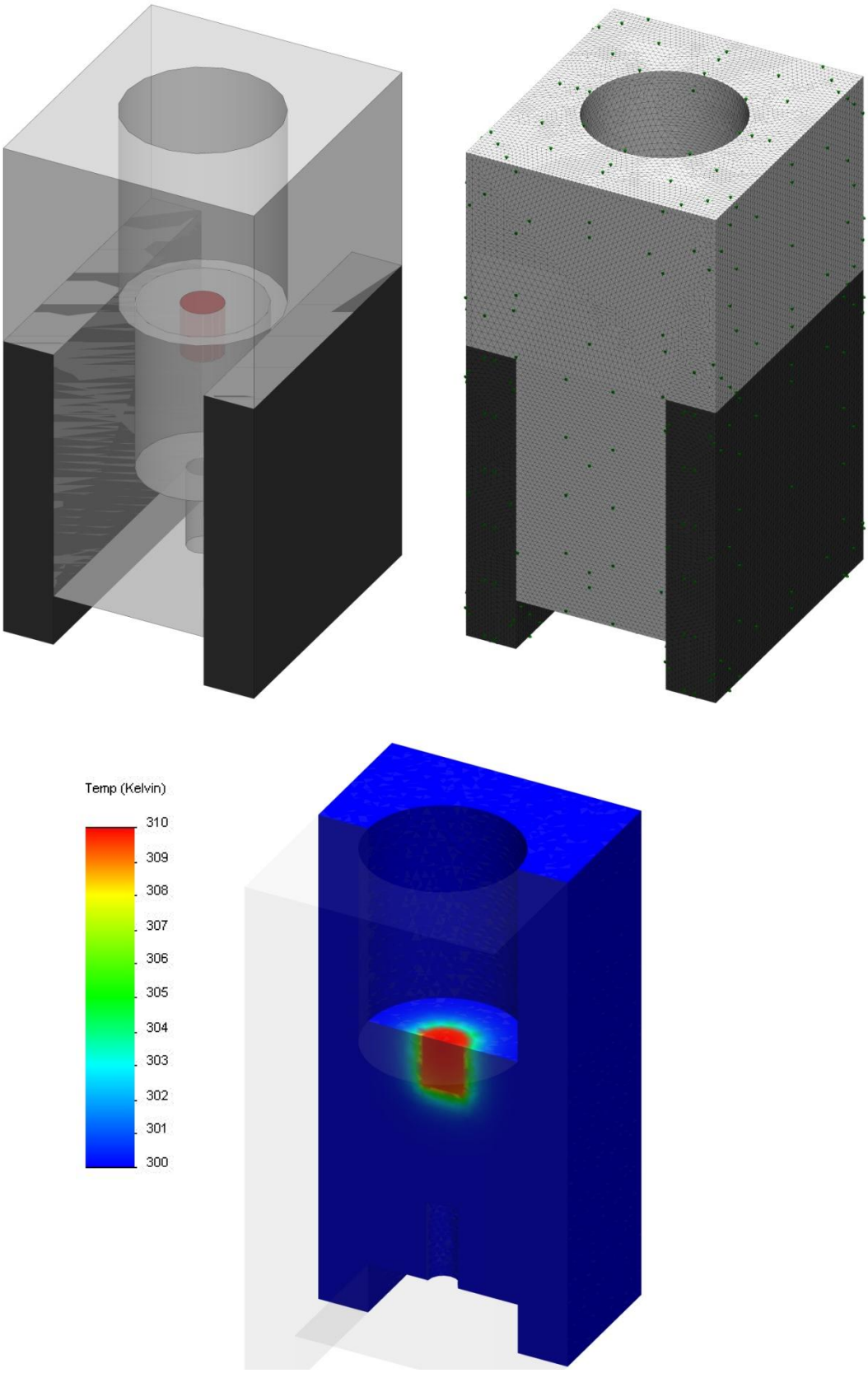

Fig. 7-7: Simulation by Solidworks, upper left: creation of model, upper right: meshing; lower figure: the result of simulation

	Mass (mg)	Density (g/cm^3)	Volume fraction (-)	Thermal conductivity (W/m/K)	Specific heat capacity (J/kg/K)
Air	0	1		0.024	1004
Ethanol	2.4	0.789		0.171	2440
Fe_2O_3	88	4.1		2.9	670
Fe_2O_3+Air	88	1.401	34%	0.060	777
Fe_2O_3+Ethanol	90	1.438		1.103	1835
Co	86	8.9		100	420
Co+Air	86	1.369	15%	0.037	643
Co 2	37.4	8.9		100	420
Co+Air 2	37.4	1.058	12%	0.034	685

Tab. 7-2: The table of material properties for simulation

The thermal properties of the samples mixture are calculated in section 7.3, the result is shown in Tab. 7-2.

In the next section we shall first deduce the heating power due to the field by comparing the experimental temperature rise to the one obtained by simulation with SolidWorks. Then we shall compare these values to the one obtained from the hysteresis curve and we shall discuss the effect of the rotation of the particles on the dissipated power; at last we shall give an estimate of the temperature field which could be produced around a tumor heated with a magnetic field.

7.5.1. Results for the heating power

The two solid lines in Fig. 7-8 represent the temperature rise after application of a field of 12kA/m for the same iron oxide powder, the only difference being that the upper curve corresponds to the powder alone, whereas the lower one corresponds to the powder completely wetted by 3ml of ethanol. The drop of temperature rise is mainly due to the much larger thermal conductivity of the mixture ethanol/powder than the powder alone. We have adjusted the injected power to P=25 mW in order to fit the upper curve (black triangles) We see that not only we very well represent the rise of temperature with time but also, with the same power, we are quite close to the experimental result in the presence of ethanol (red triangles compared to the solid line). This value must be compared with the one obtained from the hysteresis loop, Eq.(7.10), which is P=29mW. The difference is quite small and these results give us good confidence in both the experimental device and its simulation.

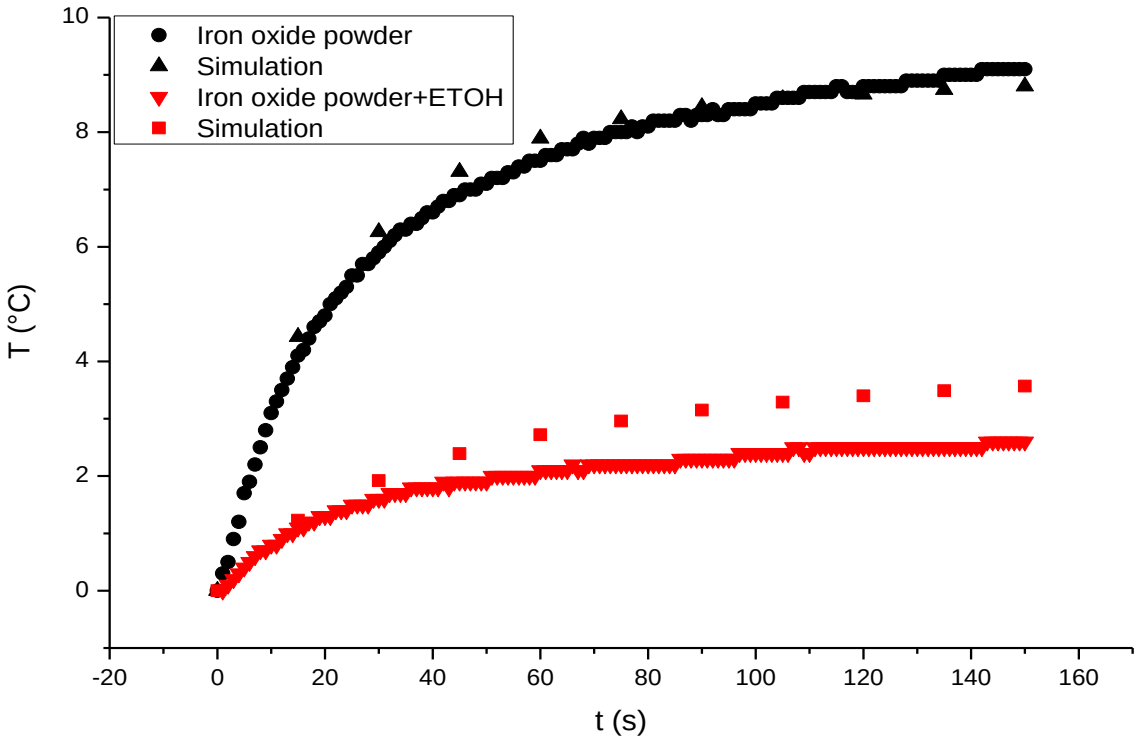

Fig. 7-8: Temperature rise versus time, comparison of experimental and simulation results for iron oxide powder with and without ethanol, the conditions of experiment: f=5 kHz, H=12kA/m

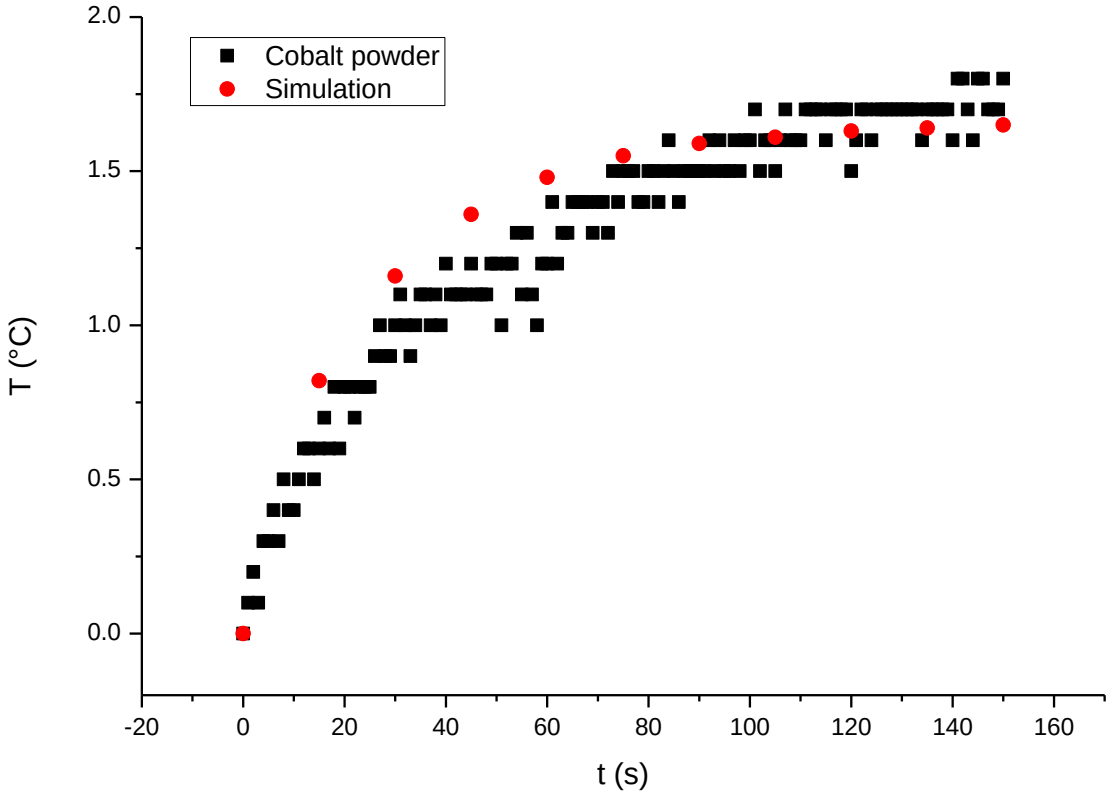

Fig. 7-9: Increase of temperature versus time, the comparison of experimental and simulation result of cobalt powder, same condition as in Fig. 7-8

We did the same analysis with cobalt nanowires. The rise of temperature is less important than for iron oxide and there is more scatter in the experiments ,cf Fig. 7-9, nevertheless, once again, we well reproduce with only one parameter, which is the injected power, the whole temperature rise for different frequencies and mass of particles;we found P= 2.3mW. The power dissipation obtained from Eq. (7.10) for a magnetic field of 12kA/m and a frequency of 5 kHz is 1.1mW, so this time we have a power obtained from the measurement of the temperature rise which is two times larger than the one cacculated from the area of the hysteresis curve. This quite large difference can come from the fact that we were obliged to extrapolate the energy curve in the absence of measurement at a field of 12kA/m. Furthermore these measurements were made by Squid in Versailles laboratory on very low quantities (1mg) which can be the source of supplementary errors, especially at low fields.

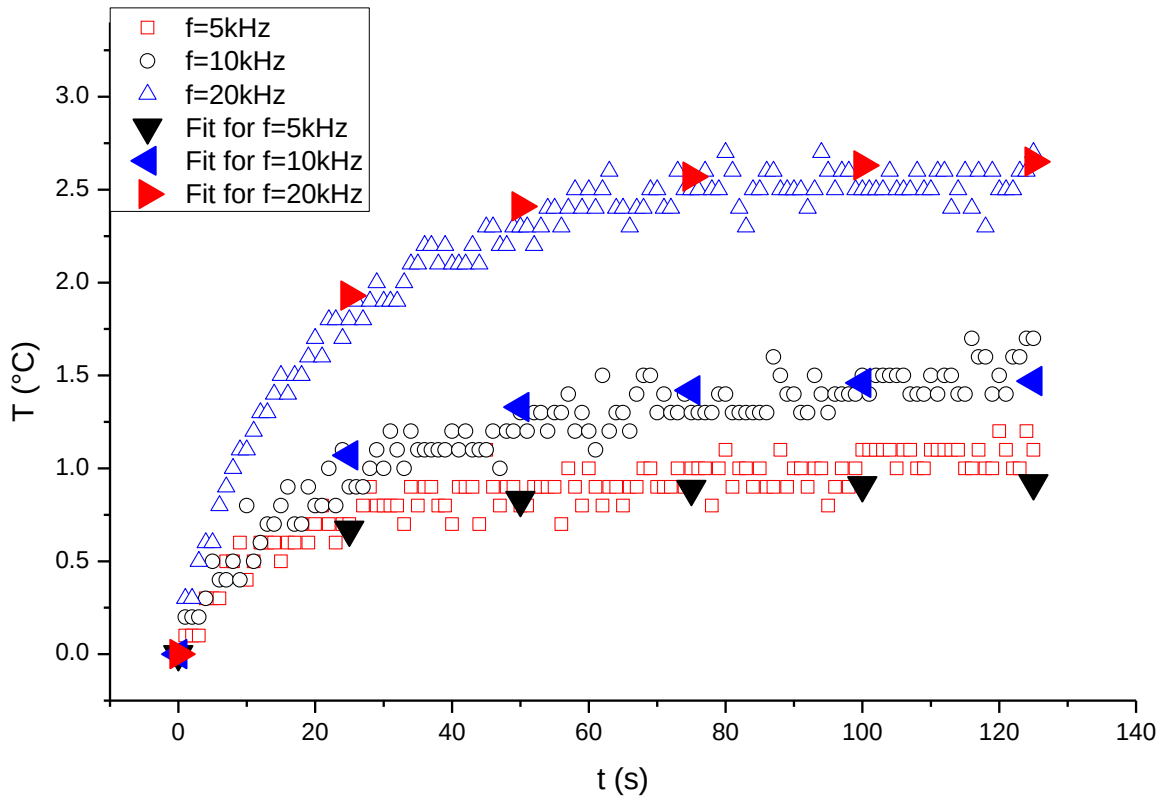

Fig. 7-10: Temperature rise of cobalt nanowires powders versus time, for different frequencies of the applied magnetic field (5, 10, 20 kHz)

The frequency plays an important role in hyperthermia experiments, because the higher is the frequency of the applied magnetic field, the more energy is dissipated. This is clearly seen in Fig. 7-10 where we have reported the temperature rise obtained at three different frequencies. Once again taking the injected power as a parameter for each frequency, well reproduces the whole curve. The values of the power corresponding to the adjustement are reported in the column "simulation" of Tab. 7-3.

f(kHz)	H(kA/m)	W(J/m3)	Power hysteresis(mW)	Power simulation(mW)	ratio
5	12	22	1.1	2.3	0.46
10	11	19	1.8	3.6	0.5
20	10	16	3	7	0.43

Tab. 7-3: Result of calculation and simulation of power dissipated of cobalt nanowires in different frequencies

Note that the fields are slightly decreasing with the frequency due to the heating of the wires at higher frequencies. The ratio of the column simulation to the column "hysteresis" remains almost constant, indicating that we have actually an increase of dissipation at constant field which is well proportional to the frequency.

7.5.2. Power produced by the rotation of the particles

In practice, due to the limitation on the field in our device, we were not able to observe a temperature change when the particles are dispersed in a liquid at low volume fraction, so that they can move freely inside the fluid. We can nevertheless get a theoretical value for this viscous dissipation. We have seen in section 3.1.2 that the angular motion of a needle was given by Eq.(3.33):

$$\theta(t) = 2\, arctg\left[tg(\frac{\theta_0}{2})\, e^{-\frac{1}{\omega.\tau_R}\sin(\omega.t)} \right] \tag{7.11}$$

Where $\tau_R = \alpha/\beta$ is the viscous rotational time and θ_0 the initial angle relatively to the field axis. Taking α and β respectively from (3.4) and (3.23) gives:

$$\tau_R = \frac{C.\pi.\eta.a^2}{3\mu_0 M_r H} \tag{7.12}$$

Here, for a first evaluation we can take C=1. M_r is the remanent magnetization and a is the aspect ratio of the cobalt nanofibers. At high frequency ($\omega\tau_R$>>1) we can expand the exponential term leading to:

$$\theta(t) = \theta_0 - \frac{\sin(\theta_0)}{\omega\tau_R}\sin(\omega t) \tag{7.13}$$

The viscous dissipation is equal to the energy provided by the magnetic field, so per unit volume and for one period we have:

$$W = -\mu_0 \int_0^T M_r(t)\frac{dH}{dt}dt$$

So the dissipated power per unit volume will be:

$$P = \frac{\mu_0 M_r H \omega}{T}\int_0^T \cos(\theta(t))\sin(\omega t)dt \tag{7.14}$$

Inserting (7.13) into (7.14) gives:

$$P = \frac{\mu_0 M_r H}{\tau_R}\frac{\sin^2(\theta_0)}{2}$$

Taking an equiprobability for the initial orientation,θ_0, we obtain:

$$P = \frac{\mu_0 M_r H}{4\tau_R} \tag{7.15}$$

We can note than contrary to the hysteresis dissipation which increases proportionally to the frequency, here we reach a constant value, because the amplitude of the oscillation is decreasing as the inverse of the frequency, cf. Eq. (7.13). At any frequency the viscous dissipation is given by Eq.(7.14) and Eq.(7.11). A typical curve for the dissipation versus frequency is shown in Fig. 7-11. We see that there is a maximum at a quite low frequency

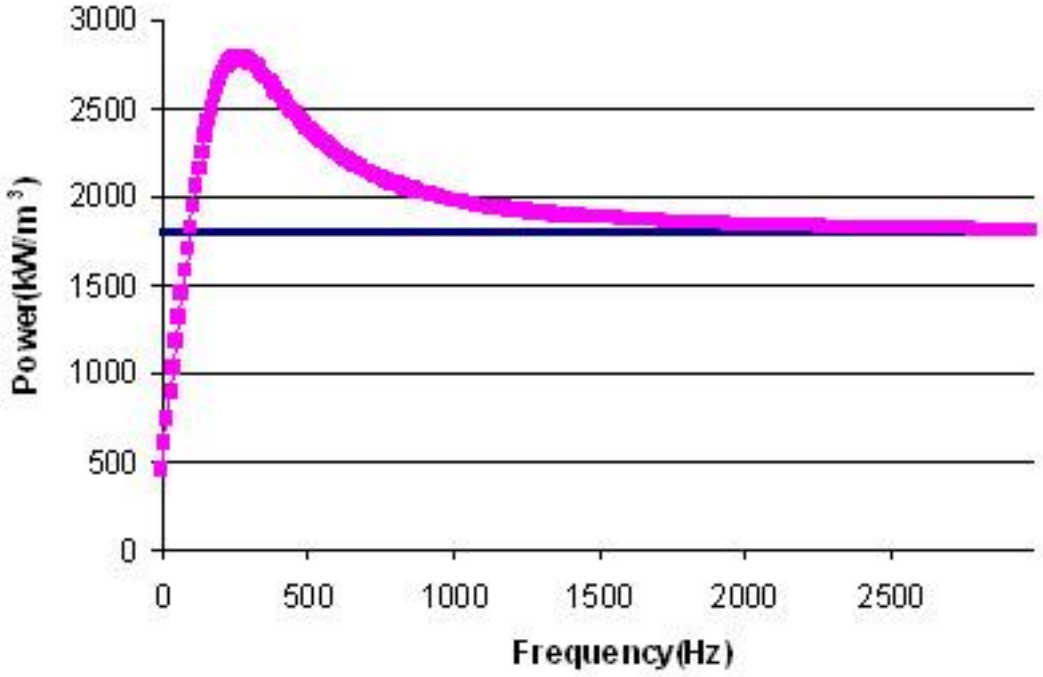

***Fig. 7-11. Power dissipated by rotation for θ_0=30° H=12kA/m Mr=250kA/m. η=10Pa.s The blue line is the limit predicted by Eq.*(7.15)**

(300Hz) which corresponds to $\omega\tau_R$=0.5. The limiting power given by Eq. (7.15) is inversely proportional to the viscosity and proportional to the square of the applied field and to the square of the remanent magnetization. In the conditions corresponding to Fig. 7-11 –with a viscosity of 10Pa.s-we obtain 0.4W/g which is much larger than the power loss due to hysteresis with cobalt particles at 5 kHz and for the same field: 0.01W/g. This difference decreases when we increase the field: for H=1000Oe we shall have 17.5W/g for mechanical dissipation against 2.6W/g for hysteresis. The calculation of mechanical dissipation with our fibers supposes that there are no interactions at all between the nanofibers, which is certainly not the case since they carry a permanent magnetization. This interaction will likely strongly reduce the motion of the particles, furthermore, if the particles stick to the membrane, their motion will still be further reduced. On the contrary the heating due to the hysteresis is much easier to control since it does not depend on the motion of the particles, and as we shall see in the next section, the heating power can be sufficient for an hyperthermia treatment

7.5.3. Simulation of the heating of a tumor

As reported in the right part of Tab. 7-1, if we apply a magnetic field of 159kA/m (2000*Oe*) at 10 kHz on cobalt nanowires powders, the energy dissipated will be 12.8kJ/m3. So if we inject

only 89mg of cobalt nanowires inside a $1cm^3$ tumor, which corresponds to a volume fraction of 1%, we produce a power P=1.28W (cf.Eq(7.10)).

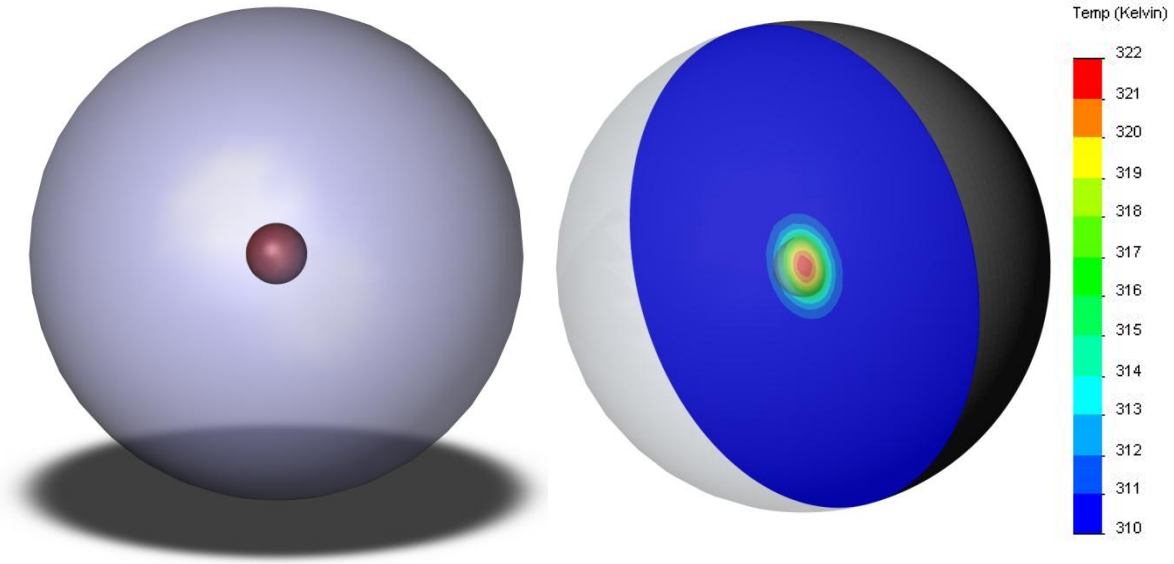

Fig. 7-12: Simulation of hyperthermia in cancer treatment, the left figure represents a tumor of $1cm^3$ in a spherical environment (diameter of 10cm)of water, the right figure is the result of simulation (Cross-sectional view)after 2mn

In a first approach, we consider that the thermal properties of the tumor and of the surrounding medium are the same, and we take a sphere of 10cm of radius to simulate the surrounding medium of the tumor with the thermal properties of water.The power is only injected in the small sphererepresenting the tumor as shown in Fig. 7-12. The temperature map after 2mn is shown in the left side of Fig. 7-12. It appears that after 2 mn we have already a temperature rise of 12°C at the center and that the domain where the temperature is above 40°C is restricted to a sphere of radius 9mm, compared to the radius of the tumor of 6.3mm. So the tissue which would be affected by the treatment is quite well restricted to the one where the particles have been injected.

7.6. Conclusion

Besides the magnetolysis effect, we have studied the possibility to heat locally a tumor thanks to the hysteresis losses of the magnetic particles. In this aim we have built a device which allows recording the temperature increase in the presence of an alternative field in the range 0 to 20 kHz and maximum amplitude of 12kA/m at 10 kHz. By using an appropriated software, we were able to simulate the temperature rise that we observe experimentally and to deduce

from this simulation the power produces by the application of the field. On the other hand we have measured the area of the hysteresis loop and compared the theoretical prediction based on this hysteresis loop to the one measured from the temperature rise. We have obtained a good agreement for the commercial iron oxide powder but for the cobalt nanofibers there is a difference by a factor of two which is very likely due to the large uncertainty on the value of the area of the hysteresis loop at low field. We have also shown theoretically that an other efficient dissipation process could, in principle, be obtained from the presence of a remanent magnetization induced by a previous application of a high magnetic field. The inconvenience, as was the case for small nanoparticles already used in hyperthermia, is that the dissipated power depends a lot on the viscoelastic environment of the particles. At last we have seen that, if we apply a strong enough field (H=2000Oe) - but still practically feasible at 10kHz- the raise of temperature obtained with cobalt nanofibers would be large enough to get an efficient hyperthermia treatment.

8. CONCLUSION AND PERSPECTIVES(EN. FR)

This dissertation has described the use of magnetic microprobes to study the rheological properties of a viscoelastic fluid and an improved method to determine the rheological properties of cancer cells by atomic force microscope. This dissertation also has discussed the feasibility to obtain highly monodisperse magnetic nanoparticles, and their bioapplications: the possibility of mechanically destruction of the cancer cells under a low frequency alternative magnetic field, and the hyperthermia under a higher frequency magnetic field.

We have first studied the rotation and the translation of a submillimetric fiber in a Newtonian fluid. The domain of rotation of the fiber has been determined both in the inertial regime and in the viscous regime and the boundary between rotation and oscillation is well recovered experimentally. It shows in particular that the critical frequency for rotation is inversely proportional to the viscosity and the square of the aspect ratio, but does not depend on the volume of the particle, as long as the inertia remains negligible. Then we compared different techniques based on the use of magnetic probes to study the rheological properties of a model viscoelastic fluid, which can represent the ones of cellular environment. This study was carried out with three different shapes of probe: spherical, cylindrical and a thin plate and two regimes of field gradient: alternative or step like. The values of the viscosity, shear modulus and yield stress obtained by modeling the motion of these probes in a viscoelastic solid at low strain, were in reasonable agreement with the results obtained from conventional rheometry. The use of micronic probes to obtain the rheological properties of cells could then be envisaged, but the optical measurement of the position of the probe at the scale of a fraction of micron is difficult to reach, especially when the motion is not guaranteed to be perpendicular to the optical axis, which will be the case if the particle lays on the surface of a cell which is usually not a flat one.

Then it seemed to us that the use of atomic force microscope was the more reliable tool to study the rheological properties of the cells. We have first developed an experimental protocol which allows a precise detection of the surface of the cell and to get a force versus

displacement of a spherical probe after removing the contribution of viscous forces on the cantilever. By combining, in the frame of a linear theory, the Hertz model of indentation and the description of the viscoelastic medium by the response function G (t) to a strain step, we can calculate the motion of the spherical probe and deduce, from a fit of the experimental motion, the viscoelastic parameters entering in the function G (t). Based on this method, the viscoelastic properties of Hep G2 cancer cells have been obtained. It has appeared that high velocities of indentation have revealed a short relaxation time, which is generally ignored due to the use of smaller indentation velocity. A generalized Maxwell solid with two relaxation times has been shown to rather well describe the viscoelastic behavior of the cell. This work has given a firm basis for the determination of viscoelastic functions with the help of an AFM. The AFM method is very useful to detect the rheological properties of cells since it can be applied locally and it is possible to obtain some map of the viscoelastic properties of the membrane and its supporting actin network. Furthermore by applying different level of forces, it is possible to follow the effect of this mechanical stimulation on the integrity of the cell.

Besides the study of the rheology of cancer cells, another important objective of this work was the study of the magnetolysis of the cells with the help of magnetic particles actuated by a magnetic field. In this aim we have used particles with a size in the micron range: spherical commercial particles and also spindle like iron particles synthesized in the laboratory. The interest of these particles is that they are very monodisperse and there spindle shape can help to mechanically injure the membranes. Their coverage with gold and polyethylene glycol to ensure biocompatibility has been realized and their functionalization for a specific binding to folate receptors which are overexpressed in certain cancer cells is underway. Also, in view to combine magnetolysis and hyperthermia, nanofibers made of cobalt have been synthesized and characterized. They are also quite well monodispersed with an average length of 80nm and a diameter of 10nm. They present a strong hysteresis cycle, which can be used for hyperthermia and also they can be easily magnetized to carry a permanent moment which allows rotating them by an applied alternative magnetic field-which is not the case for the iron particles which present a very small hysteresis. It still remains to make them biocompatible, which are presently under study through a transmetalation reaction between cobalt and gold as the one realized with iron spindle particles.

The central objective of this dissertation was to try to prove that one can damage cancer cells by magnetic nanoparticles in a low frequency magnetic field, mechanically not by

hyperthermia, since the heat dissipation is generally difficult to control. We have developed a well controlled protocol where the cells are submitted to the gradient of a magnetic field induced by the vibration of a neodymium permanent magnet below the plane of adherent cells. It was then possible to determine precisely the force exerted on each particle by the magnetic field and also, thanks to the rheological characterization, to simulate the penetration of the particles inside the cells. We have proved that the application of an alternative magnetic field at a frequency of a few hertz was able to provoke the death of the cells contrary to the application of a constant field. Still the calculation of the penetration of the particles inside the membrane remained quite small: the order of a few nm. The application of such a periodic indentation with the conical tip of an AFM had no effect on the cells and it was only above an indentation of 400nm that we obtained the death of the cell indicated by the blue trypan staining. Based on the observation of the clustering of the particles under magnetic field we proposed that it is the formation of aggregates of magnetic particles which considerably increases the magnetic force and the indentation. These results, and in particular those obtained with submicronic spindle like particles are promising, since despite a low volume of order $10^{-3}\mu m^3$ which can circulate in blood capillaries without causing embolism, it was possible to destroy the cell by a moderate field, which is easily obtained in MRI scanners. Further investigations with an AFM of the adhesion between a probe and the membrane of the cell versus the frequency of the oscillating motion could also help for a better understanding of the frequency dependency of the cell mortality.

Although it was not our main objective, we have studied the possibility to use cobalt nanofibers for hyperthermia applications, because these particles have a large hysteresis cycle and can also be magnetized to carry a permanent moment. Instead of using a calorimeter, which is difficult to install in the presence of the magnetic circuit, we have deduced the dissipated power from the measurement of the temperature rise and the use of a FEM calculation. The comparison with the dissipation which can be obtained from the measurement of hysteresis was in good agreement for a commercial powder presenting a strong hysteresis at low field. For our cobalt particles presenting a lower hysteresis at low field there is a difference by a factor of two between the two methods, which is believed to come from the low reliability of the measurement of the hysteresis area at low field. At higher field the predicted heating power obtained from the hysteresis measurement appears to be large enough for clinical applications. In the future, an improvement of our device should

allow applying a field of 600Oe at 10 kHz, which will allow more precise measurements of the dissipated power. It would also be interesting to study the effect of a permanent magnetization of the cobalt nanofibers dispersed in a suspending liquid since the calculation predicts a larger viscous dissipation than the one due to internal hysteresis.

Cette thèse a décrit l'utilisation de microsondes magnétiques pour étudier les propriétés rhéologiques d'un fluide viscoélastique et une nouvelle méthodologie pour la détermination des propriétés rhéologiques des cellules cancéreuses à partir d'un microscope à force atomique. Nous avons également montré la faisabilité d'obtenir des nanoparticules magnétiques très monodisperses et étudié leurs bioapplications: la destruction mécanique des cellules cancéreuses sous un champ magnétique alternatif à basse fréquence, et l'hyperthermie sous un champ magnétique de fréquence plus élevée.

Nous avons d'abord étudié la rotation et la translation d'une fibre submillimétrique dans un fluide newtonien. Le domaine de rotation de la fibre a été déterminé à la fois dans le régime inertiel et dans le régime visqueux et la limite entre la rotation et l'oscillation est déterminé expérimentalement. On montre en particulier que la fréquence critique de rotation est inversement proportionnelle à la viscosité et au carré du rapport d'aspect, mais ne dépend pas du volume de la particule, à condition que l'inertie reste négligeable. Puis nous avons comparé différentes techniques basées sur l'utilisation de sondes magnétiques pour étudier les propriétés rhéologiques d'un fluide viscoélastique modèle, qui peut représenter celles du milieu cellulaire. Cette étude a été réalisée avec trois formes de sondes différentes: sphériques, cylindriques et d'une plaque mince et par deux régimes de gradient de champ: alternatif ou continu. Les valeurs de la viscosité, du module de cisaillement et la contrainte seuil obtenus par la modélisation du mouvement de ces sondes dans un solide viscoélastique à faible déformation, sont en accord raisonnable avec les résultats obtenus avec un rhéomètre conventionnel. L'utilisation de sondes microniques pour obtenir les propriétés rhéologiques des cellules pourrait alors être envisagé, mais la mesure optique de la position de la sonde à

l'échelle d'une micron est difficile à atteindre, surtout lorsque le mouvement n'est pas forcément perpendiculaire à l'axe optique, ce qui sera le cas si la particule se fixe sur la surface d'une cellule qui n'est généralement pas plate.

Ensuite, il nous a semblé que l'utilisation d'un microscope à force atomique est l'outil le plus adapté pour étudier les propriétés rhéologiques des cellules. Nous avons mis au point un premier protocole expérimental qui permet d'avoir une détection précise de la surface de la cellule et d'obtenir la force en fonction de l'indentation d'une pointe sphérique après avoir enlevé la force visqueuse sur le cantilever. En combinant, dans le cadre d'une théorie linéaire, l'indentation par le modèle de Hertz et la description du milieu viscoélastique en fonction de la réponse G (t) à une déformation incrémentale, on peut calculer le mouvement de la pointe sphérique et en déduire, à partir d'un l'ajustement du mouvement expérimental, les paramètres viscoélastiques qui entrent dans la fonction G(t). Selon cette méthode, les propriétés viscoélastiques de cellules cancéreuses Hep G2 ont été obtenues. On a observé que les vitesses élevées d'indentation font apparaître un temps de relaxation rapide qui est généralement ignoré en raison de l'utilisation de faibles vitesses d'indentation. Un solide de Maxwell généralisé avec deux temps de relaxation a décri bien le comportement viscoélastique de la cellule. Ce travail a donné une base solide pour la détermination des fonctions viscoélastiques d'une cellule à l'aide d'un AFM. Cette méthode de l'AFM est très utile pour détecter les propriétés rhéologiques des cellules, car elle peut être appliquée à un endroit précis de la cellule et permet ainsi d'obtenir une carte du module de Young de la cellule. De plus, en appliquant différents niveaux de forces, il est possible de suivre l'effet de cette stimulation mécanique sur l'intégrité de la cellule.

Outre l'étude de la rhéologie de cellules cancéreuses, un autre objectif important de ce travail est l'étude de la magnétolyse des cellules à l'aide de particules magnétiques mises en mouvement par un champ magnétique. Dans ce but, nous avons utilisé des particules d'une taille de l'ordre du micron: particules sphériques commerciales et aussi en forme de fuseau comme des particules de fer synthétisées en laboratoire. L'intérêt de ces dernières particules, est leur grande monodispersité et leur extrémité pointue favorise la destruction mécanique des cellules. Leur fonctionnalisation par une couche d'or et de polyéthylène glycol pour assurer la biocompatibilité a été réalisée et le greffage d'acide folique pour une liaison spécifique à des récepteurs folate qui sont surexprimés dans certaines cellules cancéreuses est en cours. En outre, en vue de combiner magnétolyse et hyperthermie, les nanofibres de cobalt ont été

synthétisées et caractérisées. Elles sont également assez bien monodisperses avec une longueur moyenne de 80 nm et un diamètre de 10 nm. Elles présentent un cycle d'hystérésis important qui peut être utilisé pour l'hyperthermie et de plus elles peuvent être facilement magnétisées pour acquérir un moment permanent qui permet de les faire tourner par application d'un champ magnétique alternatif ce qui n'est pas le cas pour les particules de fer, qui présentent une très faible hystérésis. Il reste encore à les rendre biocompatibles par une réaction de transmétallation entre le cobalt et l'or comme celle réalisée avec les particules de fer.

L'objectif principal de cette thèse était d'essayer d'endommager mécaniquement les cellules cancéreuses par des nanoparticules magnétiques dans un champ magnétique basse fréquence, et non par l'hyperthermie, puisque la dissipation thermique est généralement difficile à contrôler. Nous avons développé un protocole bien contrôlé où les cellules sont soumises au gradient d'un champ magnétique induit par la vibration d'un aimant permanente en néodyme au dessous d'une boîte de pétri contenant des cellules tumorales. Il est alors possible de déterminer avec précision la force exercée sur chaque particule par le champ magnétique et également, grâce à la caractérisation rhéologique, de simuler la pénétration des particules à l'intérieur des cellules. Nous avons ainsi prouvé que l'application d'un champ magnétique alternatif à une fréquence de quelques hertz a pu provoquer la mort des cellules, contrairement à l'application d'un champ constant. Cependant, le calcul de la pénétration des particules à l'intérieur de la cellule est restée assez faible: de l'ordre de quelques nm. L'application d'une telle indentation périodique avec la pointe conique d'un AFM n'a eu aucun effet sur les cellules et c'est seulement avec une indentation supèrieure à 400 nm que nous avons obtenu la mort de la cellule, indiquée par la coloration au trypan bleu. Basé sur l'observation d'agrégats en présence du champ magnétique, nous avons proposé que ce soit la formation d'agrégats de particules magnétiques qui augmente considérablement la force magnétique et donc l'indentation. Ces résultats, et en particulier ceux obtenus avec les nanoparticules en forme d'aiguille sont prometteurs car, malgré un faible volume de l'ordre 10^{-3} μm3 leur permettant de circuler dans les capillaires sanguins sans provoquer d'embolie, il a été possible de détruire les cellules par un champ magnétique modéré, qui est facile à obtenir dans les scanners IRM. D'autres études avec l'AFM, de l'adhérence entre la pointe et la membrane de la cellule par rapport à la fréquence du mouvement oscillant pourraient aussi nous aider à une

meilleure compréhension de la dépendance de la fréquence en fonction de la mortalité cellulaire.

Bien que ce ne fût pas notre objectif principal, nous avons étudié la possibilité d'utiliser des nanofibres de cobalt pour l'hyperthermie, car ces particules ont un cycle d'hystérésis large et peuvent être également aimantées de façon à acquérir un moment permanent. Au lieu d'utiliser un calorimètre, ce qui est difficile à installer dans un circuit magnétique, nous avons déduit la puissance dissipée par la mesure de l'élévation de la température et l'utilisation conjointe d'un calcul par éléments finis. La comparaison avec la dissipation qui peut être obtenue à partir de la mesure de l'hystérésis est en bon accord pour une poudre commerciale présentant une forte hystérésis à faible champ. Pour nos particules de cobalt présentant une faible hystérésis à bas champ, il y a une différence d'un facteur deux entre les deux méthodes. Cette différence pourrait provenir de la faible fiabilité de la mesure de la zone d'hystérésis à bas champ. Avec un champ plus élevé, la prédiction de l'élévation de température obtenue à partir de la mesure de la courbe d'hystérésis semble être assez grande pour les applications cliniques. À l'avenir, une amélioration de notre dispositif devrait permettre l'application d'un champ de 600Oe (5kA/m) à 10 kHz, et donc d'avoir des mesures plus précises de la puissance dissipée. Il serait également intéressant d'étudier l'effet d'une aimantation permanente des nanofibres de cobalt dispersées dans un liquide peu visqueux puisque le calcul prédit une plus grande dissipation visqueuse que celle due à l'hystérésis interne.

9. BIBLIOGRAPHY

1. Anand P, Kunnumakara AB, Sundaram C, Harikumar KB, Tharakan ST, Lai OS, et al. Cancer is a Preventable Disease that Requires Major Lifestyle Changes. Pharm. Res. 2008 Jul 15;25(9):2097–116.

2. Boyle P, Levin B, International Agency for Research on Cancer. World cancer report 2008. Lyon: IARC Press; 2008.

3. INCa. La situation du cancer en France en 2011. Boulogne-Billancourt: l'INCa; 2011.

4. Beaulieu.N B, D., Bloom, R., and Stein,. Breakaway: The global burden of cancer - challenges and opportunities. The Economist. Economist Intelligence Unit Limited. London; 2009;71.

5. Halperin E. Perez and Brady's principles and practice of radiation oncology. 5th ed. Philadelphia: Wolters Kluwer Health/Lippincott Williams & Wilkins; 2008.

6. Ko A. Everyone's guide to cancer therapy : how cancer is diagnosed, treated, and managed day to day. Rev. 5th ed. Kansas City: Andrews McMeel Pub.; 2008.

7. Falk MH, Issels RD. Hyperthermia in oncology. Int J Hyperthermia. 2001 Feb;17(1):1–18.

8. Armijo LM, Brandt YI, Mathew D, Yadav S, Maestas S, Rivera AC, et al. Iron Oxide Nanocrystals for Magnetic Hyperthermia Applications. Nanomaterials. 2012 May 7;2(2):134–46.

9. Habash RWY, Bansal R, Krewski D, Alhafid HT. Thermal therapy, part 1: an introduction to thermal therapy. Crit. Rev. Biomed. Eng. 2006;34(6):459–89.

10. Carrey J, Mehdaoui B, Respaud M. Simple models for dynamic hysteresis loop calculations of magnetic single-domain nanoparticles: Application to magnetic hyperthermia optimization. J. Appl. Phys. 2011;109:083921.

11. Burton G. Chemical storylines. 2nd ed. Oxford: Heinemann; 2000.

12. Freitas R. Nanomedicine. Austin TX: Landes Bioscience; 1999.

13. Barnes J. Pre-Socratic philosophers. London :: Routledge,; 1990.

14. Lu A-H, Schmidt W, Matoussevitch N, Bönnemann H, Spliethoff B, Tesche B, et al. Nanoengineering of a Magnetically Separable Hydrogenation Catalyst. Angew. Chem. Int. Ed. 2004 Aug 20;43:4303–6.

15. Gupta AK, Gupta M. Synthesis and surface engineering of iron oxide nanoparticles for biomedical applications. Biomaterials. 2005 Jun;26:3995–4021.

16. Gleich B, Weizenecker J. Tomographic imaging using the nonlinear response of magnetic particles. Nature. 2005 Jun 30;435:1214–7.

17. Scarberry KE, Dickerson EB, McDonald JF, Zhang ZJ. Magnetic Nanoparticle−Peptide Conjugates for in Vitro and in Vivo Targeting and Extraction of Cancer Cells. J. Am. Chem. Soc. 2008 Aug;130(31):10258–62.

18. Pera NP, Kouki A, Haataja S, Branderhorst HM, Liskamp RMJ, Visser GM, et al. Detection of pathogenic Streptococcus suis bacteria using magnetic glycoparticles. Org. Biomol. Chem. 2010;8(10):2425.

19. Binnig G, Quate CF. Atomic Force Microscope. Phys. Rev. Lett. 1986 Mar;56(9):930–3.

20. Hinterdorfer P, Dufrêne YF. Detection and localization of single molecular recognition events using atomic force microscopy. Nat. Methods. 2006 May;3(5):347–55.

21. Ferrari L, Kaufmann J, Winnefeld F, Plank J. Interaction of cement model systems with superplasticizers investigated by atomic force microscopy, zeta potential, and adsorption measurements. J. Colloid Interface Sci. 2010 Jul 1;347(1):15–24.

22. Butt H-J, Cappella B, Kappl M. Force measurements with the atomic force microscope: Technique, interpretation and applications. Surf. Sci. Rep. 2005 Oct;59(1-6):1–152.

23. Hoffmann PM, Oral A, Grimble RA, Ozgur ozer H, Jeffery S, Pethica JB. Direct measurement of interatomic force gradients using an ultra-low-amplitude atomic force microscope. Proc. R. Soc. A-Math. Phys. Eng. Sci. 2001 May 8;457(2009):1161–74.

24. Whelan PM, Hodgson MJ. Essential principles of physics. London: J. Murray; 1978.

25. Serway RA. Physics for scientists & engineers. Philadelphia: Saunders College Pub.; 1986.

26. Batchelor GK. Slender-body theory for particles of arbitrary cross-section in Stokes flow. Journal of Fluid Mechanics. 1970;44:419–40.

27. Van de Ven TGM. Colloidal hydrodynamics. London; San Diego: Academic Press; 1989.

28. Wilhelm C, Gazeau F, Bacri J-C. Rotational magnetic endosome microrheology: Viscoelastic architecture inside living cells. Phys. Rev. E. 2003 Jun;67:061908.

29. Keshoju K, Xing H, Sun L. Magnetic field driven nanowire rotation in suspension. Appl. Phys. Lett. 2007;91:123114.

30. Cohen ER, Lide DR, Trigg GL. AIP Physics desk reference. New York: Springer; 2003.

31. Fernández P, Heymann L, Ott A, Aksel N, Pullarkat PA. Shear rheology of a cell monolayer. New J. Phys. 2007 Nov 30;9(11):419–419.

32. Levine AJ, Lubensky TC. Response function of a sphere in a viscoelastic two-fluid medium. Phys. Rev. E. 2001 Apr;63(4 Pt 1):041510.

33. Barnes HA, Walters K, Hutton JF. An introduction to rheology. Amsterdam: Elsevier; 1996.

34. Sato M, Theret DP, Wheeler LT, Ohshima N, Nerem RM. Application of the Micropipette Technique to the Measurement of Cultured Porcine Aortic Endothelial Cell Viscoelastic Properties. J. Biomech. Eng. 1990;112(3):263–8.

35. Thoumine O, Ott A. Time scale dependent viscoelastic and contractile regimes in fibroblasts probed by microplate manipulation. J. Cell. Sci. 1997 Sep;110 (Pt 17):2109–16.

36. Mills JP, Qie L, Dao M, Lim CT, Suresh S. Nonlinear elastic and viscoelastic deformation of the human red blood cell with optical tweezers. Mech. Chem. Biosyst. 2004 Sep;1(3):169–80.

37. Hénon S, Lenormand G, Richert A, Gallet F. A New Determination of the Shear Modulus of the Human Erythrocyte Membrane Using Optical Tweezers. Biophys. J. 1999 Feb;76(2):1145–51.

38. Wang N, Butler J, Ingber D. Mechanotransduction across the cell surface and through the cytoskeleton. Science. 1993 May 21;260(5111):1124–7.

39. Maksym GN, Fabry B, Butler JP, Navajas D, Tschumperlin DJ, Laporte JD, et al. Mechanical properties of cultured human airway smooth muscle cells from 0.05 to 0.4 Hz. J. Appl. Physiol. 2000 Oct;89(4):1619–32.

40. Radmacher M, Fritz M, Kacher CM, Cleveland JP, Hansma PK. Measuring the viscoelastic properties of human platelets with the atomic force microscope. Biophys. J. 1996 Jan;70(1):556–67.

41. Lim CT, Zhou EH, Quek ST. Mechanical models for living cells--a review. J. Biomech. 2006;39(2):195–216.

42. Kuznetsova T, Starodubtseva M, Yegorenkov N, Chizhik S, Zhdanov R. Atomic force microscopy probing of cell elasticity. Micron. 2007 Dec;38(8):824–33.

43. Levine, Lubensky. One- and two-particle microrheology. Phys. Rev. Lett. 2000 Aug 21;85(8):1774–7.

44. Johnson KL. Contact mechanics. Cambridge: Cambridge Univ. Press; 2004.

45. Srinivasa R., Eswara R. An FEM approach into nanoindentation on linear elastic and visco elastic characterization of soft living cells. IJNA. 2008;55–68.

46. Dimitriadis EK, Horkay F, Maresca J, Kachar B, Chadwick RS. Determination of Elastic Moduli of Thin Layers of Soft Material Using the Atomic Force Microscope. Biophys. J. 2002 May;82(5):2798–810.

47. Darling EM, Zauscher S, Block JA, Guilak F. A Thin-Layer Model for Viscoelastic, Stress-Relaxation Testing of Cells Using Atomic Force Microscopy: Do Cell Properties Reflect Metastatic Potential? Biophys. J. 2007 Mar 1;92(5):1784–91.

48. Darling EM, Zauscher S, Guilak F. Viscoelastic properties of zonal articular chondrocytes measured by atomic force microscopy. Osteoarthr. Cartil. 2006 Jun;14(6):571–9.

49. Vadillo-Rodriguez V, Dutcher JR. Dynamic viscoelastic behavior of individual Gram-negative bacterial cells. Soft Matter. 2009;5(24):5012.

50. Balland M, Desprat N, Icard D, Féréol S, Asnacios A, Browaeys J, et al. Power laws in microrheology experiments on living cells: Comparative analysis and modeling. Phys. Rev. E. 2006 Aug;74(2 Pt 1):021911.

51. Wang N, Ingber DE. Control of cytoskeletal mechanics by extracellular matrix, cell shape, and mechanical tension. Biophys. J. 1994 Jun;66(6):2181–9.

52. Kim D-H, Rozhkova EA, Ulasov IV, Bader SD, Rajh T, Lesniak MS, et al. Biofunctionalized magnetic-vortex microdiscs for targeted cancer-cell destruction. Nat. Mater. 2010 Feb;9(2):165–71.

53. Hu S-H, Gao X. Nanocomposites with Spatially Separated Functionalities for Combined Imaging and Magnetolytic Therapy. J. Am. Chem. Soc. 2010 Jun 2;132(21):7234–7.

54. Cook SM, Lang KM, Chynoweth KM, Wigton M, Simmonds RW, Schäffer TE. Practical implementation of dynamic methods for measuring atomic force microscope cantilever spring constants. Nanotechnology. 2006 May 14;17(9):2135–45.

55. Ahassan E, Heinz W, Antonik M, Dcosta N, Nageswaran S, Schoenenberger C, et al. Relative Microelastic Mapping of Living Cells by Atomic Force Microscopy. Biophys. J. 1998 Mar;74(3):1564–78.

56. Alcaraz J, Buscemi L, Puig-de-Morales M, Colchero J, Baró A, Navajas D. Correction of Microrheological Measurements of Soft Samples with Atomic Force Microscopy for the Hydrodynamic Drag on the Cantilever. Langmuir. 2002 Feb;18(3):716–21.

57. Chu Y-S, Dufour S, Thiery JP, Perez E, Pincet F. Johnson-Kendall-Roberts Theory Applied to Living Cells. Phys. Rev. Lett. 2005 Jan;94(2):028102.

58. Guevorkian K, Colbert M-J, Durth M, Dufour S, Brochard-Wyart F. Aspiration of Biological Viscoelastic Drops. Phys. Rev. Lett. 2010 May;104(21):218101.

59. Yoffe EH. Modified Hertz theory for spherical indentation. Philos. Mag. A. 1984 Dec;50(6):813–28.

60. Dintwa E, Tijskens E, Ramon H. On the accuracy of the Hertz model to describe the normal contact of soft elastic spheres. Granul. Matter. 2007 Nov 14;10(3):209–21.

61. Wilhelm J, Frey E. Elasticity of Stiff Polymer Networks. Phys. Rev. Lett. 2003 Sep;91(10):108103.

62. Schiffmann KI. Nanoindentation creep and stress relaxation tests of polycarbonate. Int. J. Mater. Res. 2006;1199–211.

63. Broedersz C, Depken M, Yao N, Pollak M, Weitz D, MacKintosh F. Cross-Link-Governed Dynamics of Biopolymer Networks. Phys. Rev. Lett. 2010 Nov;105(23):238101.

64. Vadillo-Rodriguez V, Beveridge TJ, Dutcher JR. Surface Viscoelasticity of Individual Gram-Negative Bacterial Cells Measured Using Atomic Force Microscopy. J. Bacteriol. 2008 Apr 11;190(12):4225–32.

65. Wu Y-N, Chen D-H, Shi X-Y, Lian C-C, Wang T-Y, Yeh C-S, et al. Cancer-cell-specific cytotoxicity of non-oxidized iron elements in iron core-gold shell NPs. Nanomedicine. 2011 Aug;7(4):420–7.

66. Chen M, Yamamuro S, Farrell D, Majetich SA. Gold-coated iron nanoparticles for biomedical applications. J. Appl. Phys. 2003;93(10):7551.

67. Kandori K, Ishikawa T. Preparation and microstructural studies on hydrothermally prepared hematite. J. Colloid Interface Sci. 2004 Apr;272(1):246–8.

68. Ocaña, Morales, Serna. Homogeneous Precipitation of Uniform alpha-Fe2O3 Particles from Iron Salts Solutions in the Presence of Urea. J. Colloid Interface Sci. 1999 Apr 15;212(2):317–23.

69. Gou X, Wang G, Park J, Liu H, Yang J. Monodisperse hematite porous nanospheres: synthesis, characterization, and applications for gas sensors. Nanotechnology. 2008 Mar 26;19(12):125606.

70. Iijima M, Yonemochi Y, Kimata M, Hasegawa M, Tsukada M, Kamiya H. Preparation of agglomeration-free hematite particles coated with silica and their reduction behavior in hydrogen. J. Colloid Interface Sci. 2005 Jul 15;287(2):526–33.

71. Baker C, Hasanain SK, Shah SI. The magnetic behavior of iron oxide passivated iron nanoparticles. J. Appl. Phys. 2004;96(11):6657.

72. Carpenter EE, Calvin S, Stroud RM, Harris VG. Passivated Iron as Core−Shell Nanoparticles. Chem. Mater. 2003 Aug;15(17):3245–6.

73. Fung KK, Qin B, Zhang XX. Passivation of α-Fe nanoparticle by epitaxial γ-Fe2O3 shell. Mater. Sci. Eng. A-Struct. 2000 Jun;286(1):135–8.

74. Morales MP, González-Carreño T, Serna CJ. The formation of a–Fe2O3 monodispersed particles in solution. J. Mater. Res. 2011 Jan 31;7(09):2538–45.

75. Ishikawa T, Matijevic E. Formation of monodispersed pure and coated spindle-type iron particles. Langmuir. 1988 Jan;4(1):26–31.

76. Lee W, Kim MG, Choi J, Park J-I, Ko SJ, Oh SJ, et al. Redox−Transmetalation Process as a Generalized Synthetic Strategy for Core−Shell Magnetic Nanoparticles. J. Am. Chem. Soc. 2005 Nov;127(46):16090–7.

77. Milosevic I, Jouni H, David C, Warmont F, Bonnin D, Motte L. Facile Microwave Process in Water for the Fabrication of Magnetic Nanorods. J. Phys. Chem. C. 2011 Oct 6;115(39):18999–9004.

78. Wang Y, Muramatsu A, Sugimoto T. FTIR analysis of well-defined α-Fe2O3 particles. Colloid Surf. A-Physicochem. Eng. Asp. 1998 Mar;134(3):281–97.

79. Yariv S, Mendelovici E. The Effect of Degree of Crystallinity on the Infrared Spectrum of Hematite. Appl. Spectrosc. 1979;33(4):410–1.

80. Danan H. New Determinations of the Saturation Magnetization of Nickel and Iron. J. Appl. Phys. 1968;39(2):669.

81. Mandal S, Krishnan KM. CocoreAushell nanoparticles: evolution of magnetic properties in the displacement reaction. J. Mater. Chem. 2007;17:372.

82. Chakroune N, Viau G, Ricolleau C, Fiévet-Vincent F, Fiévet F. Cobalt-based anisotropic particles prepared by the polyol process. J. Mater. Chem. 2003 Feb 5;13(2):312–8.

83. Viau G, Garcıa C, Maurer T, Chaboussant G, Ott F, Soumare Y, et al. Highly crystalline cobalt nanowires with high coercivity prepared by soft chemistry. physica status solidi (a). 2009 Apr;206:663–6.

84. Gao J, Gu H, Xu B. Multifunctional Magnetic Nanoparticles: Design, Synthesis, and Biomedical Applications. Acc. Chem. Res. 2009 Aug 18;42(8):1097–107.

85. Lok C. Medical imaging techniques are being adapted to study gene expression and other cellular activities in living animals. Corie Lok talks to the pioneers who are watching cells at work in their natural habitat. Nature. 2001;412:372–4.

86. Medeiros SF, Santos AM, Fessi H, Elaissari A. Stimuli-responsive magnetic particles for biomedical applications. Int. J. Pharm. 2011 Jan;403(1-2):139–61.

87. Beaune G, Levy M, Neveu S, Gazeau F, Wilhelm C, Ménager C. Different localizations of hydrophobic magnetic nanoparticles within vesicles trigger their efficiency as magnetic nano-heaters. Soft Matter. 2011;7(13):6248.

88. Sandre O, Moreaux L, Brochard-Wyart F. Dynamics of transient pores in stretched vesicles. Proc. Natl. Acad. Sci. USA. 1999 Sep 14;96(19):10591–6.

89. Lübbe AS, Alexiou C, Bergemann C. Clinical applications of magnetic drug targeting. J. Surg. Res. 2001 Feb;95(2):200–6.

90. Rejman J, Oberle V, Zuhorn IS, Hoekstra D. Size-dependent internalization of particles via the pathways of clathrin- and caveolae-mediated endocytosis. Biochem. J. 2004 Jan 1;377(1):159.

91. Bauer IW, Li S-P, Han Y-C, Yuan L, Yin M-Z. Internalization of hydroxyapatite nanoparticles in liver cancer cells. J. Mater. Sci. Mater. Med. 2007 Aug 15;19(3):1091–5.

92. Fung AO, Kapadia V, Pierstorff E, Ho D, Chen Y. Induction of Cell Death by Magnetic Actuation of Nickel Nanowires Internalized by Fibroblasts. J. Phys. Chem. C. 2008 Oct 2;112(39):15085–8.

93. Darton NJ, Hallmark B, James T, Agrawal P, Mackley MR, Slater NKH. Magnetic capture of superparamagnetic nanoparticles in a constant pressure microcapillary flow. J. Magn. Magn. Mater. 2009 May;321(10):1571–4.

94. Bouchlaka MN, Sckisel GD, Wilkins D, Maverakis E, Monjazeb AM, Fung M, et al. Mechanical Disruption of Tumors by Iron Particles and Magnetic Field Application Results in Increased Anti-Tumor Immune Responses. Mosley RL, editor. PLOS ONE. 2012 Oct 25;7(10):e48049.

95. Liu D, Wang L, Wang Z, Cuschieri A. Magnetoporation and Magnetolysis of Cancer Cells via Carbon Nanotubes Induced by Rotating Magnetic Fields. Nano Lett. 2012 Oct 10;12(10):5117–21.

96. Griffiths DJ. Introduction to electrodynamics. San Francisco: Pearson; 2008.

97. Osborn J. Demagnetizing Factors of the General Ellipsoid. Phys. Rev. 1945 Jun;67(11-12):351–7.

98. Freshney RI. Culture of animal cells : a manual of basic technique. New York, N.Y.: Wiley-Liss; 2000.

99. Sneddon IN. The relation between load and penetration in the axisymmetric boussinesq problem for a punch of arbitrary profile. Int. J. Eng. Sci. 1965 May;3(1):47–57.

100. Weisenhorn AL, Khorsandi M, Kasas S, Gotzos V, Butt H-J. Deformation and height anomaly of soft surfaces studied with an AFM. Nanotechnology. 1993 Apr 1;4(2):106–13.

101. Hategan A, Law R, Kahn S, Discher DE. Adhesively-Tensed Cell Membranes: Lysis Kinetics and Atomic Force Microscopy Probing. Biophys. J. 2003 Oct;85(4):2746–59.

102. Teissie J, Golzio M, Rols MP. Mechanisms of cell membrane electropermeabilization: a minireview of our present (lack of ?) knowledge. Biochim. Biophys. Acta. 2005 Aug 5;1724(3):270–80.

103. Kashevsky BE, Agabekov VE, Kashevsky SB, Kekalo KA, Manina EY, Prokhorov IV, et al. Study of cobalt ferrite nanosuspensions for low-frequency ferromagnetic hyperthermia. Particuology. 2008 Oct;6(5):322–33.

104. Sullivan CR. Optimal choice for number of strands in a litz-wire transformer winding. IEEE Trans. Power Electron. 1999 Mar;14(2):283–91.

105. Lacroix L-M, Carrey J, Respaud M. A frequency-adjustable electromagnet for hyperthermia measurements on magnetic nanoparticles. Rev. Sci. Instrum. 2008;79:093909.

106. Cicchitti A, Lombaradi C, Silversti M, Soldaini G, Zavattarlli R. Two-phase cooling experiments – ressure drop heat transfer burnout measurements. Energia Nucleare. 1960;7(6):407–25.

107. Maxwell JC. A treatise on electricity and magnetism. Vol. 1. Oxford: Clarendon; 1873.

108. Landauer R. The Electrical Resistance of Binary Metallic Mixtures. J. Appl. Phys. 1952;23(7):779.

109. Kirkpatrick S. Percolation and Conduction. Rev. Mod. Phys. 1973 Oct;45(4):574–88.

110. Richter C, Viljoen HJ, Van Rensburg NFJ. Effective thermal conductivity estimates of particulate mixtures. J. Appl. Phys. 2003;93(5):2663.

111. Gonzo EE. Estimating correlations for the effective thermal conductivity of granular materials. Chem. Eng. J. 2002 Dec 28;90(3):299–302.

112. Awad MM, Muzychka YS. Effective property models for homogeneous two-phase flows. Exp. Therm. Fluid Sci. 2008 Oct;33(1):106–13.

113. Mercier S, Molinari A, El Mouden M. Thermal conductivity of composite material with coated inclusions: Applications to tetragonal array of spheroids. J. Appl. Phys. 2000;87(7):3511.

114. Buongiorno J. Convective Transport in Nanofluids. J. Heat Transfer. 2006;128(3):240.

115. Shin D, Banerjee D. Enhancement of specific heat capacity of high-temperature silica-nanofluids synthesized in alkali chloride salt eutectics for solar thermal-energy storage applications. Int. J. Heat Mass Transf. 2011 Feb;54(5-6):1064–70.